



THE HONG KONG
POLYTECHNIC UNIVERSITY

香港理工大學

Pao Yue-kong Library

包玉剛圖書館

Copyright Undertaking

This thesis is protected by copyright, with all rights reserved.

By reading and using the thesis, the reader understands and agrees to the following terms:

1. The reader will abide by the rules and legal ordinances governing copyright regarding the use of the thesis.
2. The reader will use the thesis for the purpose of research or private study only and not for distribution or further reproduction or any other purpose.
3. The reader agrees to indemnify and hold the University harmless from and against any loss, damage, cost, liability or expenses arising from copyright infringement or unauthorized usage.

IMPORTANT

If you have reasons to believe that any materials in this thesis are deemed not suitable to be distributed in this form, or a copyright owner having difficulty with the material being included in our database, please contact lbsys@polyu.edu.hk providing details. The Library will look into your claim and consider taking remedial action upon receipt of the written requests.

THE HONG KONG POLYTECHNIC UNIVERSITY

DEPARTMENT OF APPLIED PHYSICS

**Ferromagnetism in carbon-doped
ZnO thin films and nanostructures**

WEI CHANGSONG

A THESIS SUBMITTED IN PARTIAL FULFILLMENT OF
THE REQUIREMENTS FOR
THE DEGREE OF DOCTOR OF PHILOSOPHY

December 2011

CERTIFICATE OF ORIGINALITY

I hereby declare that this thesis is my own work and that, to the best of my knowledge and belief, it reproduces no material previously published or written, nor material that has been accepted for the award of any other degree or diploma, except where due acknowledgement has been made in the text.

_____ (Signature)

WEI CHANGSONG (Name of candidate)

ABSTRACT

The ZnO-based diluted magnetic semiconductors (DMS) have attracted scientific interest due to their unique properties and multifunctionality in ferromagnetic and ferroelectric. Transition metals have been chosen as dopants for ZnO-based DMS. However, the origin of the ferromagnetism is controversial as it is suspected that the ferromagnetism is induced by transition metal dopant clusters or secondary phases. In order to avoid the ambiguous ferromagnetism in ZnO-based DMS, carbon, as a non-magnetic element, has been suggested to be an appropriate dopant for ZnO-based DMS. Hence, in this thesis, the possibility of using carbon as a dopant to produce ZnO-based DMS is explored. The ZnO thin films were prepared firstly by the filtered cathodic vacuum arc technique. Optimization of the growth parameters, such as substrates temperature and oxygen pressure, were achieved in relation to the structural, electrical and optical properties of the ZnO thin films. The fabrication of the carbon-doped ZnO (ZnO:C) thin films and nanostructures were performed by the ion beam irradiation (IBI) technique. The two vital parameters of IBI, ion beam energy and irradiation time, were investigated systematically to determine the effective carbon doping parameters for the formation of ferromagnetic ZnO:C thin films and nanostructures.

The structural, electrical and magnetic properties of the ZnO:C thin films and nanoneedles were characterized. The ZnO:C thin films and nanoneedles all

showed the hexagonal wurtzite structure with high crystallinity. The ferromagnetism in the ZnO:C system with Curie temperature (T_C) higher than 330 K was found. The saturated magnetization (M_s) was enhanced with the increase of the carbon concentration. The anomalous Hall effect and negative magnetoresistance with *p*-type conduction were detected in the ZnO:C system. These unusual transport behaviors in the ZnO:C system are regarded as the effect correlating to the magnetic inhomogeneous and magnetic phase transition. The ferromagnetism in the ZnO:C system is stable in ambient air for more than one year. In addition, the magnetic anisotropy was detected as a signature of intrinsic ferromagnetism in the ZnO:C system. As for the ZnO:C nanoneedles, there is another dominated effect due to the strong dipole–dipole magnetic interaction among the nanoneedles resulted in the magnetic anisotropy.

Several characterization methods were employed to investigate the origin of ferromagnetism in the ZnO:C system. Transmission electron microscopy (TEM) and high resolution transmission electron microscopy (HRTEM) analysis suggest that the carbon doping introduced some defects in the ZnO samples leading to the decrease of grain size of the ZnO:C with increasing the carbon concentration. X-ray diffraction (XRD) spectra show the reduction of lattice constant *c* with carbon doping which is expected as smaller C ions substituted into the O sites of ZnO lattices. The X-ray absorption near-edge structure (XANES) spectra indicate a strong hybridization of O 2*p* orbitals with C 2*p* states in ZnO:C system. This *p*-*p* interaction leads to an indirect ferromagnetic coupling of C atoms. It is speculated that the substitution of C ions into O sites is related to the origin of the ferromagnetism in the ZnO:C system.



LIST OF PUBLICATIONS

1. **C.S. Wei**, S.P. Lau, M. Tanemurab, M. Subramanianb and Y. Akaike, “Ferromagnetic anisotropy of carbon-doped ZnO nanoneedles fabricated by ion beam technique”, *Applied Surface Science*, 258 (2012) 5486.
2. T.S. Heng, S.P. Lau, **C.S. Wei**, L. Wang, B.C. Zhao, M. Tanemura and Y. Akaike, “Stable ferromagnetism in *p*-type carbon-doped ZnO nanoneedles”, *Applied Physics Letters*, 95 (2009) 133103.
3. **C.S. Wei**, S.P. Lau, M. Tanemura and Y. Akaike, “Ferromagnetism in C-doped ZnO films prepared by ion beam technique”, Presented at International Conference on Materials for Advanced Technologies (ICMAT2011), Symposium B: Synthesis and Architecture of Nanomaterials, Jun.26-Jul.1, 2011, Singapore.
4. S.P. Lau, T.S. Heng, **C.S. Wei** and M. Tanemura, “Ferromagnetic carbon-doped ZnO nanoneedles”, *IEEE Proceedings*, 5424999 (2010) 1118.
5. L.B. Tang, X.M. Li, R.B. Ji, K.S. Teng, G.A. Tai, J. Ye, **C.S. Wei** and S.P. Lau, “Bottom-up synthesis of large-scale graphene oxide nanosheets”, *J. Chem. Mat.* 22 (2012), 5676.

ACKNOWLEDGMENT

I would like to express my gratitude to all those who gave me the opportunity to pursue my PhD study in the Hong Kong Polytechnic University and to complete this thesis. I am heartily thankful to my supervisor, Prof. S.P. Lau, whose encouragement, guidance and support from the initial to the final level of my study which enabled me to develop an understanding of the research subject. Without his consistent and illuminating instruction, this thesis could not have reached its present form.

I am greatly indebted to the professors and teachers at the Department of Applied Physics: Prof. L.H.W. Chan, Prof. K.H. Wong, Prof. S.F. Yu, Dr. J.H. Hao, Dr. C.W. Leung, and Dr. X.M. Zhang, for their kind assistance, stimulating discussions and endless encouragement.

Additionally, my special thanks go to all people have supported my research project: Prof. M. Tanemura and his research group from Nagoya Institute of Technology for ion beam irradiation, Prof. D.G. McCulloch and Dr. J.L. Peng from RMIT University for transmission electron microscopy and high resolution transmission electron microscopy, Prof. S.S. Kim and Dr. K. Asokan from Inha University and Prof. A.V. Soldatov and Dr. V. Mazalova from Southern Federal University for X-ray absorption near-edge fine structure spectroscopy.

I would also like to thank all my colleagues from the Department of Applied Physics, Dr. L.B. Tang, Dr. G.A. Tai, Dr. J. Ye, Mr. C.M. Luk, and Mr. Y.Y. Hui, who supported me in my research work.

TABLE OF CONTENTS

CERTIFICATE OF ORIGINALITY.....	I
ABSTRACT	II
LIST OF PUBLICATIONS	IV
ACKNOWLEDGMENT	V
TABLE OF CONTENTS.....	VI
LIST OF FIGURE CAPTIONS.....	X
LIST OF TABLE CAPTIONS.....	XV
LIST OF ABBREVIATIONS	XVI
CHAPTER 1 Introduction.....	1
1.1 Spintronics	1
1.2 Diluted magnetic semiconductors	6
1.3 ZnO-based DMS	9
1.4 Carbon-doped ZnO DMS	11
1.5 Objectives of research	12
1.6 Thesis overview	13
CHAPTER 2 Literature review.....	15
2.1 ZnO	15
2.2 Transition metal doped ZnO (ZnO:TM) DMS	19
2.2.1 Cobalt-doped ZnO (ZnO:Co)	19
2.2.2 Iron-doped ZnO (ZnO:Fe).....	22
2.2.3 Manganese-doped ZnO (ZnO:Mn).....	23
2.3 Carbon-doped ZnO (ZnO:C) DMS	24

CHAPTER 3	Experimental and methodology	28
3.1	Sample fabrication methodology	28
3.1.1	Filtered cathodic vacuum arc technique	28
3.1.2	Ion beam irradiation technique.....	30
3.2	Sample characterization methodology	33
3.2.1	X-ray diffraction.....	33
3.2.2	Energy dispersive X-ray spectroscopy	34
3.2.3	X-ray absorption near-edge fine structure spectroscopy.....	35
3.2.4	Field emission scanning electron microcopy.....	36
3.2.5	Transmission electron microscopy	37
3.2.6	High resolution transmission electron microscopy.....	38
3.2.7	Electron energy loss spectroscopy.....	38
3.2.8	Atomic force microscopy	39
3.2.9	Magnetic force microscopy	41
3.2.10	Photoluminescence spectroscopy	41
3.2.11	Vibrating sample magnetometer.....	43
3.2.12	Superconducting quantum interference device.....	44
3.2.13	Transport properties measurement	48
CHAPTER 4	Preparation of ZnO films	50
4.1	Introduction.....	50
4.2	Effect of substrate temperature	51
4.2.1	XRD structural characteristics.....	51
4.2.2	Photoluminescence.....	53
4.3	Effect of O ₂ pressure	54
4.3.1	XRD structural characteristics.....	54
4.3.2	Photoluminescence.....	55
4.4	ZnO thin films prepared under optimized conditions.....	58
4.5	Summary	59
CHAPTER 5	Preparation of ZnO:C by IBI	60
5.1	Effect of distance from the graphite plate	60



5.2	Effect of ion beam energy	62
5.2.1	Atomic force microscopy	62
5.2.2	Magnetic properties	64
5.3	Effect of irradiation time	65
5.3.1	Atomic force microscopy	65
5.3.2	Magnetic properties	67
5.4	Summary	68
CHAPTER 6 Ferromagnetic ZnO:C thin films.....		69
6.1	Introduction	69
6.2	Structural characteristics	70
6.3	Ferromagnetic properties	71
6.3.1	M-H loops	71
6.3.2	ZFC-FC magnetization curves	73
6.3.3	Magnetic force microscopy	74
6.4	Transport properties	75
6.4.1	Hall effect.....	75
6.4.2	Temperature dependence of the resistivity	76
6.4.3	Anomalous Hall resistivity	78
6.4.4	Magnetoresistance	80
6.5	Stability of ferromagnetism.....	81
6.6	Summary	83
CHAPTER 7 Ferromagnetic ZnO:C nanoneedles		85
7.1	Introduction	85
7.2	Structural characteristics	86
7.3	Field emission scanning electron microscopy	87
7.4	Magnetic properties.....	88
7.4.1	M-H loops	88
7.4.2	ZFC-FC magnetization curves	90
7.4.3	Ferromagnetic anisotropy	91



7.5	Transport properties	94
7.6	Summary	95
CHAPTER 8 Origin of ferromagnetism.....		97
8.1	Introduction	97
8.2	High resolution transmission electron microscopy	97
8.3	Transmission electron microscopy	98
8.4	Electron energy loss spectroscopy	100
8.5	X-ray absorption near-edge fine structure spectroscopy	102
8.6	Origin of the ferromagnetism in ZnO:C.....	105
8.7	Summary	107
CHAPTER 9 Conclusions and recommendations		108
9.1	Conclusions	108
9.2	Recommendations for future works	109
REFERENCES		112

LIST OF FIGURE CAPTIONS

Figure 1-1 Electron has a charge and a spin.	2
Figure 1-2 Spin up and spin down.	2
Figure 1-3 Applications of spintronics in storage industry.	3
Figure 1-4 Concept of GMR.	4
Figure 1-5 Concept of TMR.	5
Figure 1-6 Schematic illustration of spin-FET, spin-LED and spin-RTD.	6
Figure 1-7 Three types of semiconductors: (a) a nonmagnetic semiconductor, which contains no magnetic ions; (b) a diluted magnetic semiconductor, an alloy between nonmagnetic semiconductor and magnetic element; and (c) a magnetic semiconductor, in which a periodic array of magnetic element is present.	8
Figure 1-8 Computed values of the Curie temperature for various <i>p</i> -type semiconductors containing 5% of Mn per cation.[23].	10
Figure 2-1 The rock salt (a), zincblende (b) and wurtzite (c) phases of ZnO. O atoms are shown as the bigger grey spheres, Zn atoms as the small black spheres. [59].	17
Figure 3-1 Schematic diagram of the FCVA system.	29
Figure 3-2 Schematic diagrams of the fabrication of (a) ZnO:C thin films and (b) ZnO:C nanoneedles by IBI technique.	31
Figure 3-3 Schematic diagram of the formation mechanism of the ZnO:C nanoneedles. (a) Ar ⁺ ions are irradiated onto the graphite target and carbon layer, (b) formation of the carbon needles, (c) carbon needles acted as a mask against the sputter erosion for the formation of ZnO:C nanoneedles.	32
Figure 3-4 Energy diagram of the fundamental photoabsorption processes and the subsequent filling of the core hole by emission of a photon or an Auger electron which contribute to XANES spectra.	36

Figure 3-5 Schematic diagram of AFM.....	40
Figure 3-6 Schematic diagram of MFM.	41
Figure 3-7 Sample holder and detection mechanism of VSM.....	43
Figure 3-8 Configuration of SQUID. [From Quantum Design company]	45
Figure 3-9 Diagram of the ZFC-FC magnetization curves.....	47
Figure 4-1 XRD patterns of the ZnO thin films grown at different temperatures with 0.5 mTorr oxygen pressure.	52
Figure 4-2 PL spectra of the ZnO thin films grown at 200, 300 and 400 °C with 0.5 mTorr oxygen pressure.....	54
Figure 4-3 XRD patterns of the ZnO thin films grown at 400 ° with oxygen pressures of 0.5, 1.0 and 1.2 mTorr.	55
Figure 4-4 PL spectra of (a) the ZnO thin films grown at 200 °C, (b) 300 °C and (c) 400 °C with different oxygen pressures.	56
Figure 4-5 (a) Surface and (b) cross-sectional SEM images of the ZnO film grown at optimized conditions.....	58
Figure 5-1 Schematic diagram of the experimental set up for doping various C concentration into ZnO films.	60
Figure 5-2 AFM micrographs of (a) as-grown ZnO, and ZnO:C thin films irradiated with different ion beam energies: (b) 500 eV, (c) 600 eV, (d) 700 eV, (e) 800 eV, (f) 900 eV, (g) 1000 eV.....	63
Figure 5-3 ZnO:C thin films were prepared under different ion beam energies. (a) The M-H loops of the ZnO:C thin films. (b) The dependence of saturated magnetizations of the ZnO:C thin films on the ion beam energies.	65
Figure 5-4 AFM micrographs of the ZnO:C thin films fabricated at 700 eV with different times (a) 3, (b) 5, (c) 7, (d) 9 minutes.	66
Figure 5-5 The roughness of the ZnO:C thin films fabricated at 700 eV with different irradiation times (open squares), comparing with the roughness of the films irradiated by the different ion beam energies (solid squares).	67
Figure 5-6 ZnO:C thin films were fabricated at 700eV with different irradiation times. (a) The M-H loops of the ZnO:C thin films	

	prepared at different irradiation times. (b) The dependence of magnetic moment of the ZnO:C thin films on the irradiation time.	68
Figure 6-1	(a) XRD patterns of the ZnO thin film and ZnO:C thin films with different carbon concentration and (b) the expanded view of XRD patterns.	70
Figure 6-2	The magnetization hysteresis loops of the ZnO:C thin films with different carbon concentrations at room temperature.	72
Figure 6-3	The hysteresis loops of the ZnO:C (film ①) film at 5 and 300 K. The inset shows the expanded view of the hysteresis loops.	73
Figure 6-4	The ZFC-FC magnetization curves for the ZnO:C thin film (film ①) measured at magnetic field of 50 Oe.	74
Figure 6-5	(a) The MFM micrograph of the ZnO:C thin film (film ②); (b) the expanded view of the MFM micrograph; (c) the correspond AFM micrograph of the ZnO:C thin film in the same area of (b).....	75
Figure 6-6	Temperature dependence of the resistivity on the ZnO:C thin film (film ①). The variable range hopping in the presence of carrier-carrier interaction is evident from the linearity of $\ln(\rho)$ vs. $T^{-1/2}$ as shown in the inset, where solid curves are a guide for the eye. The linear fit depicts a transport mechanism and activation energy change at 216 K for the sample.....	77
Figure 6-7	The magnetic field dependence of anomalous Hall resistivity ρ_{xy} on the ZnO:C thin film (film ①) measured at 300 K. The applied magnetic field is perpendicular to the sample plane with constant current of 0.01 mA as illustrated in the inset.	78
Figure 6-8	Temperature dependence resistivity of the ZnO:C thin film (film ①) under an applied field of 0, 1, 4 and 8 Tesla. Inset shows the temperature dependence resistivity from 180 to 240 K.....	79
Figure 6-9	The MR curves of the ZnO:C thin film (film ①) measured at 5, 200, and 300 K.....	81
Figure 6-10	M_s and hole concentration of the ZnO:C thin film (film ①) as a function of the storage time.	82

Figure 6-11 M_s dependence of the ZnO:C thin film (film ①) as a function of annealing temperature.	83
Figure 7-1 (a) XRD patterns of the ZnO nanoneedles and ZnO:C nanoneedles with different carbon concentrations and (b) the expanded view of XRD patterns.	86
Figure 7-2 FESEM images of the ZnO:C nanoneedles: (a) sample surface is perpendicular to the electron beam; (b) sample surface faces to the electron beam with a tilt angle of 45°	88
Figure 7-3 The magnetization hysteresis loops of the ZnO:C nanoneedles with different carbon concentration at room temperature.	89
Figure 7-4 Magnetic hysteresis loops of the ZnO:C nanoneedles (needles ①) at 5 and 300 K. The inset shows enlarged view of the magnetic hysteresis loops.	89
Figure 7-5 ZFC-FC magnetization curves for ZnO:C nanoneedles with different carbon concentrations measured at low magnetic field of 50 Oe.	90
Figure 7-6 The magnetization hysteresis loops of the ZnO:C nanoneedles (needles ①) at room temperature in the perpendicular and parallel directions of the applied fields.	91
Figure 7-7 Angular dependence of M_s and H_c for the ZnO:C nanoneedles (needles ①).	92
Figure 7-8 The magnetic field dependence of anomalous Hall resistivity (ρ_{xy}) of the ZnO:C nanoneedles (needles ①) measured at 300 K. The applied magnetic field is perpendicular to the sample's plane with constant current of 0.01 mA. The ρ_{xy} data after background subtraction is displayed in the inset.	95
Figure 8-1 (a)~(c) HRTEM images of the ZnO:C thin film. The stacking fault (purple arrow) and platelike defects (yellow arrow) are marked in the images (b) and (c), respectively. (d) HRTEM image of the as-grown ZnO. (e) The comparison image of the SADP of ZnO:C with the simulated patterns of ZnO.	98
Figure 8-2 TEM images of ZnO:C thin films (a) film ①, (b) film ② and (c) film ④.	99
Figure 8-3 The magnetization hysteresis loops of the undoped ZnO samples irradiated by ion beam.	100

Figure 8-4	The typical EELS spectra of the ZnO:C thin films.....	101
Figure 8-5	EDX mapping of the ZnO:C thin film. On the top left is a TEM image of the same area.	102
Figure 8-6	The normalized XANES spectra at O <i>K</i> -edge of the ZnO:C thin films (film ①, ② and ④).....	104
Figure 8-7	The normalized XANES spectra at C <i>K</i> -edge of ZnO:C thin films (film ①, ② and ④).	105
Figure 8-8	Calculated total (top panel) and local density of states for the carbon dopant and a neighboring Zn atom. The Fermi level is indicated by the dashed vertical line. [46]	106



LIST OF TABLE CAPTIONS

Table 1	Reported magnetic properties of TM-doped ZnO DMS.....	11
Table 2	Physical parameters of ZnO.	15
Table 3	Comparison of the physical properties of some compound semiconductors.	16
Table 4	FWHM, grain size, interplanar spacing and lattice parameter (c) of ZnO thin films grown at 200, 300 and 400 °C with 0.5 mTorr oxygen pressure.	53
Table 5	Transport properties of ZnO thin film.	59
Table 6	The roughness of the as-grown and irradiated ZnO thin films under different ion beam energies.....	64
Table 7	The roughness of the as-grown ZnO thin films and irradiated ZnO thin films at 700 eV with irradiation time ranging from 3 to 9 minutes.....	67
Table 8	The resistivity, carrier concentration and Hall mobility of the ZnO:C thin films measured at room temperature.	76

LIST OF ABBREVIATIONS

Abbreviations	Descriptions
AFM	atomic force microscopy
BMP	bound magnetic polaron
DMS	diluted magnetic semiconductor
EELS	electron energy loss spectroscopy
EDX	energy-dispersive X-ray spectroscopy
FC	field cooling
FCVA	filtered cathodic vacuum arc
FESEM	field emission scanning electron microscope
FET	field effect transistor
FM	ferromagnetism
FWHM	full width at half maximum
GMR	giant magnetoresistive
HRTEM	high resolution transmission electron microscopy
IBI	ion beam irradiation
LDOS	local density of states
LED	light-emitting diode
MFM	magnetic force microscopy
OPAMBE	oxygen plasma-assisted molecular beam epitaxy
OPDB	off-plane double bend
PL	photoluminescence
PLD	pulsed laser deposition
PPMS	physical properties measurement system
RF	radio frequency
RT	room temperature
RTD	resonant tunneling device
SADP	selected area diffraction pattern
SEM	scanning electron microscope

Abbreviations	Descriptions
SDOS	surface density of states
SQUID	superconducting quantum interference devices
TEM	transmission electron microscopy
TM	transition metals
TMR	tunnel magnetoresistance
VRH	variable range hopping
VSM	vibrating sample magnetometer
XANES	X-ray absorption near-edge fine structure spectroscopy
XRD	X-ray diffraction
ZFC	zero field cooling

CHAPTER 1

Introduction

1.1 Spintronics

Spintronics is the science and technology, also known as magnetoelectronics, in which charge and spin degrees of freedom of electrons can be used simultaneously in order to store, process, sense and communicate data and information in solid devices.

Electron has a charge and a spin as shown in Figure 1-1. In classical electronics, electronic devices rely only on the transport of electrons with charges moving by electric fields to transmit information and are stored in a capacitor to save it [1]. The control of electrical charge has influenced nearly all aspects of life during the last hundred years. However, recently physicists are trying to exploit the spin of the electron rather than its charge to create a remarkable new generation of spintronics devices. Traditional approaches using spin are based on the alignment of a spin (either “up” or “down”) relative to a reference (an applied magnetic field or magnetization orientation of the ferromagnetic film) (see Figure 1-2). Device operations then proceed with some quantity (electrical current) that depends on a predictable way with the degree of alignment. Adding the spin degree of freedom to conventional semiconductor charge based electronics or using the spin degree of freedom alone will add substantially more capability and

performance to electronic products. The advantages of these new devices would be compact, nonvolatility, increased data processing speed, consumed less power compared to conventional electronics, because the energy needed to change spin is easy compared to energy needed to push charge around, and increased integration densities compared with conventional silicon chips and circuit elements. [2]

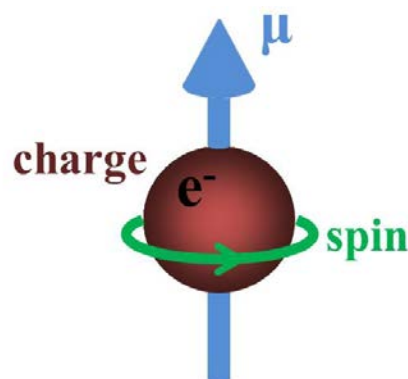


Figure 1-1 Electron has a charge and a spin.

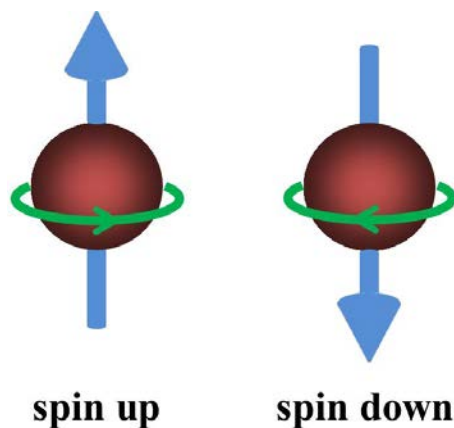


Figure 1-2 Spin up and spin down.

The prototype spintronics devices which are already in use in storage industry as a read head and a memory-storage cells are the giant magnetoresistive (GMR) [3-

5] and tunnel magnetoresistance (TMR) [6] parts which consist of alternating ferromagnetic and nonmagnetic metal layers (Figure 1-3).

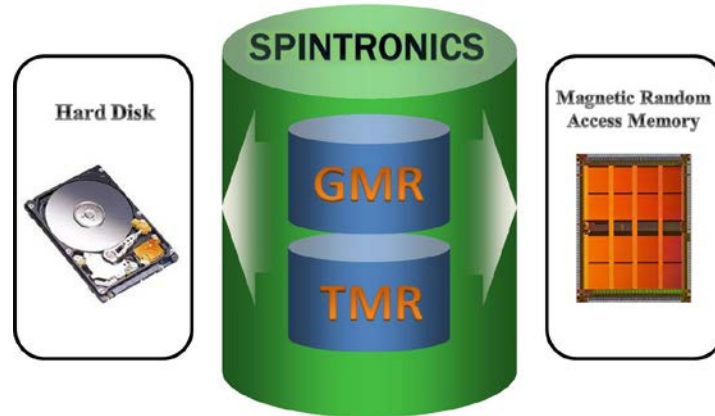


Figure 1-3 Applications of spintronics in storage industry.

Giant magnetoresistance (GMR) is a quantum mechanical magnetoresistance effect observed in thin film structures composed of alternating ferromagnetic and non-magnetic layers. When two ferromagnetic layers are separated by a non-magnetic thin layer, electrical resistance of the multilayer changes depending on the orientations of the magnetizations of ferromagnetic thin layers. When the directions of the magnetizations are the same, the possibility of electron scattering at the interface of non-magnetic/ferromagnetic layers becomes smaller, resulting in low electrical resistance. However, if the directions of the magnetizations of the two ferromagnetic layers are opposite, the electron with opposite spin orientation with respect to the magnetization of the electrode layer is scattered (spin dependent electron scattering). The electrical resistance of the multilayer becomes higher than the case for the same directions of the magnetization, as shown in Figure 1-4.

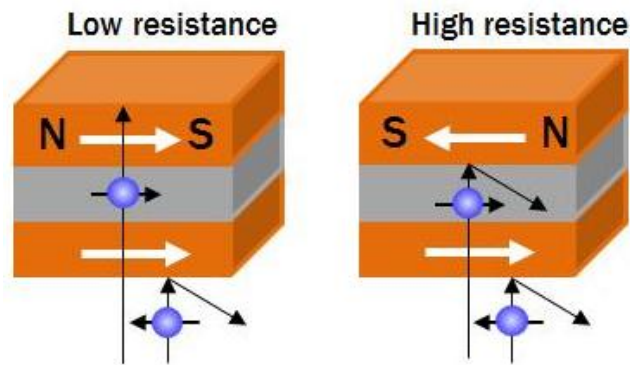


Figure 1-4 Concept of GMR.

As to TMR, when two ferromagnetic layers are separated by a thin insulator layer, electrical resistance of the multilayer in the perpendicular direction to the film changes depending on the orientations of the magnetizations of ferromagnetic thin layers because of spin dependent electron tunneling between the two ferromagnetic layers. When the directions of the magnetizations of the two ferromagnetic electrodes are the same, the possibility of electron tunneling between the two ferromagnetic electrodes through the insulator layer becomes larger, resulting in larger tunneling current. However, if the directions of the magnetizations of the two ferromagnetic electrodes are opposite, the electron with opposite spin orientation with respect to the magnetization of the ferromagnetic electrode cannot be tunneled. Then the tunneling electron current become smaller compared to the case for the same directions of the magnetizations. This phenomenon is called tunnel magnetoresistance (TMR), as shown in Figure 1-5.

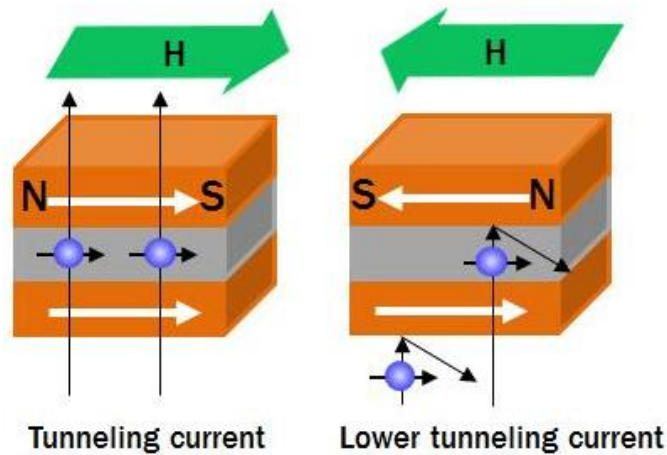


Figure 1-5 Concept of TMR.

The GMR and TMR materials have been commercialized in hard disk drivers as read heads. In magnetic recording, magnetic fields were used to read or write the information stored on the magnetization, which ‘measures’ the local orientation of spins in ferromagnets. The TMR materials are also strongly expected to be applied to magnetoresistive random access memories. Moreover, optical methods for spin injection, detection, and manipulation have been developed that exploit the ability to precisely engineer the coupling between electron spin and optical photons. Depends on a deeper understanding of fundamental spin interactions in solid state materials as well as the roles of dimensionality, defects, and semiconductor band structure in modifying these dynamics, it is anticipated that the merging of electronics and photonics will ultimately lead to new spin-based multifunctional devices (Figure 1-6) such as spin-FET (field effect transistor) [7], spin-LED (light-emitting diode), spin-RTD (resonant tunneling device) and optical switches operating at terahertz frequency etc. [2, 8-10].

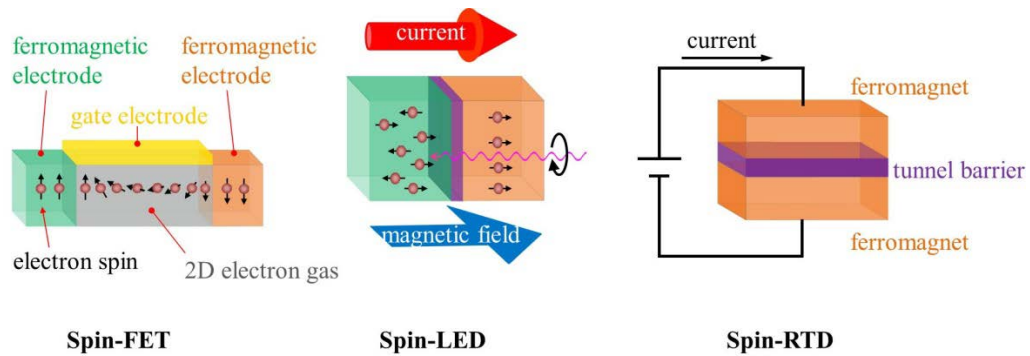


Figure 1-6 Schematic illustration of spin-FET, spin-LED and spin-RTD.

Spintronics focuses on two types of materials - ferromagnetic metallic alloys and ferromagnetic semiconductors. Ferromagnetic metallic alloys are currently used for magnetoelectronic devices. Ferromagnetic semiconductors, however, are attracting greater attention. Diluted magnetic semiconductors (DMSs), as one type of ferromagnetic semiconductors, are expected to play an important role in interdisciplinary materials science and future spintronics because charge and spin degrees of freedom are accommodated into single matter and their interplay is expected to explore novel physics and new devices.

1.2 Diluted magnetic semiconductors

Magnetic semiconductors are materials that exhibit both ferromagnetism and useful semiconductor properties. If implemented in devices, these materials could provide a new type of control of conduction. Although the traditional electronics are based on the control of charge carriers (*n*-type or *p*-type), but the practical magnetic semiconductors would also allow the control of quantum spin state (up or down). This would theoretically provide near-total spin polarization

(as opposed to iron and other metals, which provide only about 50% polarization), which is an important property for spintronics applications.

While many traditional magnetic materials, such as magnetite, are also semiconductors, materials scientists generally predict that magnetic semiconductors will only find widespread use if they are similar to well-developed semiconductor materials. To that end, DMSs have recently been a major focus of magnetic semiconductor research. These are based on traditional semiconductors, but are doped with transition metals instead, or in addition to, electronically active elements.

DMSs are semiconducting alloys whose lattice made up in part of substitutional magnetic atoms [11]. According to the contents of substitutional magnetic atoms, they can be classified as nonmagnetic semiconductor, diluted magnetic semiconductor and magnetic semiconductor (Figure 1-7). The semiconductors do not contain magnetic ions are nonmagnetic (Figure 1-7(a)), such as silicon (Si) and gallium arsenide (GaAs). In contrast, magnetic semiconductors have a periodic array of magnetic elements (Figure 1-7(c)) and have ferromagnetism and semiconducting properties, such as europium chalcogenides and semiconducting spinels. The amount of magnetic ions in DMS is between that in nonmagnetic semiconductor and magnetic semiconductor. The usefulness of semiconductors resides in the ability to dope them with impurities to change their properties, usually to *p*- or *n*-type. This approach can be followed to introduce magnetic elements into nonmagnetic semiconductors to make them into DMSs (Figure 1-7(b)) [12].

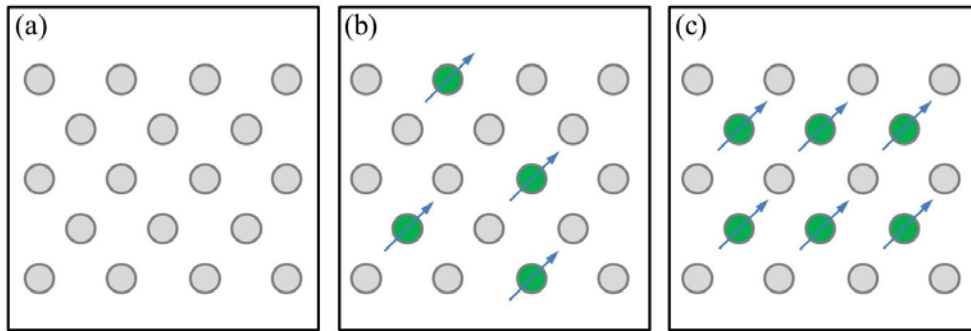


Figure 1-7 Three types of semiconductors: (a) a nonmagnetic semiconductor, which contains no magnetic ions; (b) a diluted magnetic semiconductor, an alloy between nonmagnetic semiconductor and magnetic element; and (c) a magnetic semiconductor, in which a periodic array of magnetic element is present.

As early as late 1960 to early 1970, oxide doped with Eu^{2+} [13] and spinel structured composite [14] were studied as magnetic semiconductors. However, structures of those composites are different from Si or GaAs, the crystals are very hard to produce in experiment, their low Curie temperature (T_C) (50 K or lower), strong insulation and poor semiconducting transport property [12] further hampered their value in application.

Later on, studies have been spread DMSs including transition metal (mainly Mn) doped II-VI[15], IV-VI[16], II-V [17] and III-V [18] compound semiconductors, typical examples are: II-VI: (Zn, Mn)Se [19], IV-VI: (Pb, Mn)Te [20] etc. Mn doped II-VI semiconductors are especially focused on, typical materials are (Zn, Mn)Se [21] etc. As to the III-V compound semiconductors, the prototypical carrier mediated ferromagnetic DMS is Mn-doped GaAs [22]. These closely related narrow gap III-V materials have been very extensively studied. Their properties are generally quite well understood and they have led to important insights into fundamental properties of ferromagnetic systems with strong spin-orbit coupling. They have also led to the demonstration of a wide range of novel

phenomena including some, like tunneling anisotropic magnetoresistance, which have subsequently been achieved in metal ferromagnetic systems. However despite considerable effort over many years the maximum T_C achieved in (Ga, Mn)As is still less than 200 K [22]. So unless some major new breakthrough is achieved these materials are unlikely to be of use for practical spin electronics technologies.

1.3 ZnO-based DMS

In recent years, the development of DMS is focused on the wide bandgap semiconductor as being most promising candidates for practical spintronics application. Due to the necessity that the DMS materials must exhibit ferromagnetism with a critical temperature above room temperature in order to have practical applications in spintronics devices, that temperature, i.e., (T_C is naturally deemed to be the bottleneck issue. In 2000, Dietl *et al.* [23] published a seminal paper in which mean field theory with Zener Model was used to predict which of the common diamagnetic semiconductors would exhibit a T_C above ambient temperature if doped with Mn. Of the many host semiconductors simulated, only ZnO and GaN were predicted to exhibit a T_C in excess of 300 K, as shown in Figure 1-8. From then on, the research on ZnO based magnetic semiconductors bloomed.

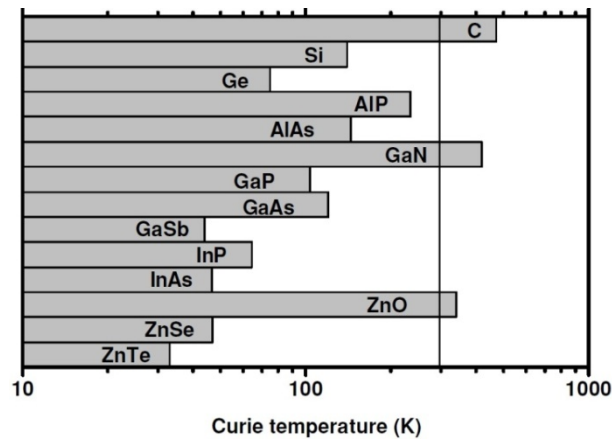


Figure 1-8 Computed values of the Curie temperature for various *p*-type semiconductors containing 5% of Mn per cation.[23]

Based on the theoretical works on ZnO,[24, 25] several groups have studied the growth of transition metal-doped ZnO (TM-doped ZnO or ZnO:TM) systems, such as Mn, Fe, Co, Cr, V and Ni in ZnO-based DMS [26-37]. It is supposed that the energy gain originating from the double-exchange mechanism [38] is increased through a little *s-d* hybridization between the conduction band and *e*-states. Table 1 summarizes the recent reports of magnetic properties of ZnO:TM DMS. Different techniques such as pulsed laser deposition (PLD), implantation, chemical method of sol-gel, magnetron sputtering and condensation, and solid state reaction have been employed to fabricate DMS. The experimental results in ZnO:TM DMS have been rather controversial. Some groups reported the ferromagnetism is intrinsic, while others believed ferromagnetism related to TM clusters. This variation can potentially be explained by the small total magnetization typically found in samples, the much diluted nature of the dopants, and the potential for artifacts, such as clustering of the magnetic dopants. The effect of such ferromagnetic clusters must be examined more carefully before the usefulness of such materials for spintronics application can be determined.

Consequently, the origin of ferromagnetism in ZnO:TM DMS is not well understood.

Table 1 Reported magnetic properties of TM-doped ZnO DMS.

Compound	TM cont. (at.%)	Fabrication method	Growth temp. (°C)	T _c (K)	Magnetism	Ref.
ZnO:Mn	<0.35	PLD	600	N/A		[26]
ZnO:Mn	0.36	PLD	600	N/A	spin-glass	[27]
ZnO _{1-x} TM _x O		PLD	500-600	N/A		[28]
ZnO:Mn	0.01-0.36	PLD	610		paramagnetic	[29]
ZnO:Mn	0-0.3	PLD	897	>30~45	0.15-0.17 μ _B /Mn	[30]
ZnO:(Mn, Sn)	0-0.3	implantation		250	1.26 μ _B /Co	[31]
ZnO:Co	0.02-0.5	PLD	300-700	N/A	spin-glass	[32]
ZnO:Co	0-0.25	sol-gel	<350	>350	0.56 μ _B /Co	[33]
ZnO:(Co, Mn, Cr or Ni)	0.05-0.25	PLD	350-600	280-300	2 μ _B /Co	[34]
ZnO:(Co, Fe)	<0.15	magnetron sputtering	600	>300	12-15 emu/cm ³	[35]
ZnO:(Fe, Cu)	0-0.1	solid state reaction		550	0.75 μ _B /Fe	[36]
ZnO:V	0.05-0.15	PLD	300	>350	0.5 μ _B /V	[37]

1.4 Carbon-doped ZnO DMS

In order to overcome the disadvantage of ZnO:TM DMS, non-magnetic elements were chosen as dopants to avoid forming the precipitates or clusters that are actually responsible for the ferromagnetic properties. Carbon is one of the candidates due to the finding of ferromagnetism in a number of carbon systems [39-43]. Carbon atoms on carbon nanotubes [44] and carbon substitutional doping in boron nitride nanotubes [45] were predicted to induce magnetism in the respective systems. Then, carbon-doped ZnO (ZnO:C) was predicted to be ferromagnetic and some initial experiments have shown signs of magnetic

behavior at room temperature.[46-50] Because carbon is not magnetic, ZnO:C is free of the ferromagnetic precipitates and hence forms a clean ferromagnetic semiconductor system.

Carbon is stable at room temperature but active at high temperature. During the conventional processes of PLD or solid state reaction, the fabrication temperature of ZnO:C is usually higher than 400 °C. In that environment, carbon could react with oxygen that makes it hard to be doped into ZnO. So the doping process of carbon is a challenge for the fabrication of ZnO:C system.

Therefore, it is of interest to explore the possibility of using carbon as a dopant to produce ZnO based DMS and to investigate the effect of carbon doping in ZnO on the peculiar magnetic properties. The calculation and simulation [49-51] confirming the ferromagnetism in ZnO:C which motivate us to fabricate the ZnO:C system using the filtered cathodic vacuum arc (FCVA) and ion beam irradiation (IBI) techniques and to investigate the characteristics of the ZnO:C. Understanding the mechanism of ferromagnetism in non-TM-doped ZnO is useful in exploring the new areas of DMS for the applications of the spintronics devices.

1.5 Objectives of research

In consideration of the potential of carbon as the dopant for the ZnO-based DMS, the main aims of the present thesis are to fabricate room temperature ferromagnetic ZnO:C system by optimizing the process parameters, to

investigate various characteristics of ZnO:C, and to reveal the mechanism of the ferromagnetism.

In this project, we attempt to:

- i. prepare ZnO thin films suit for the carbon doping to form ZnO:C system by optimizing the preparation process.
- ii. dope carbon into ZnO thin films to synthesize ZnO:C thin films and nanostructures by optimizing the fabrication process.
- iii. study the structural, ferromagnetic, and transport properties of the ZnO:C thin films and nanostructures.
- iv. investigate the origin and the mechanism of the ferromagnetism in the ZnO:C system.

1.6 Thesis overview

The background, motivation and the objectives of the research of this project are described in Chapter 1. The fundamental concepts, basic principles of the spintronics and the DMS are reviewed.

The literature review on DMS, ZnO:TM and ZnO:C is depicted in Chapter 2. The related research works of ZnO:TM and ZnO:C are described in this chapter.

Chapter 3 introduces the fabrication method for the ZnO:C system. The FCVA technique was employed to prepare the ZnO thin films and IBI technique was used to dope carbon into ZnO films. This chapter also describes various characterization methods adopted in this work.

In Chapter 4, the two important parameters of the FCVA technique, the oxygen pressure and substrate temperature, were systematically studied in order to explore the optimized parameters for the fabrication of ZnO thin films.

Chapter 5 discusses the effects of ion beam energy and the irradiation time on the fabrication of the ZnO:C thin films. The optimized parameters were found for the fabrication of ZnO:C thin films.

Chapter 6 and 7 provides the detailed characterization of the ZnO:C thin films and nanoneedles on SiO₂/Si substrates. The structural, magnetic and transport properties are investigated. The magnetic anisotropy of the nanoneedles is also investigated.

The microstructure and elemental analysis of the ZnO:C system were investigated using TEM, HRTEM, EELS and EDX in Chapter 8. The possible origin of the ferromagnetism is proposed combining with the experimental results of XRD and XANES.

A summary of the important results and achievements attained in the present investigation are emphasized and concluded in Chapter 9. As the successful fabrication of ZnO:C thin films and nanostructures, further research and development are suggested.

CHAPTER 2

Literature review

2.1 ZnO

ZnO was theoretically predicted to be ideal candidate for the room temperature DMS. The physical parameters of the ZnO are shown in Table 2.

Table 2 Physical parameters of ZnO.

Property	Value
Lattice parameters at 300K:	
a=b	3.249 Å
c	5.206 Å
Density	5.606 g/cm ³
Stable phase at 300K	Wurtzite
Thermal conductivity	0.6; 1-1.2 W/(m·K)
Melting point	1975 °C
Linear expanding	a ₀ :6.5×10 ⁻⁶ ; c ₀ : 3.0×10 ⁻⁶
Exciton binding energy	60 meV
Energy gap	3.35 eV (direct)
Intrinsic carrier concentration	<10 ⁶ /cm ³
Electron Hall mobility at	
n-type conductivity	200 cm ² /(V·s)
Hole effective mass	0.59
Hole Hall mobility at 300K	
p-type conductivity	5~50 cm ² /(V·s)

The technical progress made in synthesis (bulk and nanomaterials) and epitaxial growth of thin films indicate the possibility of realizing both *n*-type and *p*-type conduction in ZnO [52]. Making *p*-type ZnO is still a challenge and remains an intriguing issue [53, 54]. The domains of interest for compounds based on ZnO

and associated heterostructures are optoelectronics and spintronics. On comparing the key properties of ZnO with some of the competing compound semiconductors (Table 3), it is obvious that there is enormous potential for ZnO in optoelectronic applications.

Table 3 Comparison of the physical properties of some compound semiconductors.

Material	Crystal structure	Lattice parameter		Band gap energy (eV)	Energy of cohesion (eV)	Excitonic binding energy (meV)
		a(Å)	c(Å)			
		ZnO	Wurtzite			
ZnS	Wurtzite	3.82	6.26	3.8	1.59	30
ZnSe	Zincblende	5.66	--	2.7	14.29	20
GaAs	Zincblende	5.65	--	1.43	--	4.2
GaN	Wurtzite	3.19	5.19	3.39	2.24	21
6H-SiC	Wurtzite	3.18	15.12	2.86	3.17	--

ZnO is a wide-bandgap semiconductor of the II-VI semiconductor group. It has a unique combination of high band gap energy (about 3.4 eV) and excitonic stability (about 60 meV). The native doping of the semiconductor is *n*-type due to oxygen vacancies. ZnO semiconductor has several other favorable properties: good transparency, high electron mobility, strong room-temperature luminescence, etc. Those properties are already used for light emission applications [55-58] such as in emerging applications for transparent electrodes in liquid crystal displays and in energy-saving or heat-protecting windows, electronic applications of ZnO as thin-film transistors and light-emitting diodes.

The high excitonic energy also gives it strong resistance to high temperature electronic degradation during operation (e.g. laser diodes).

ZnO crystallizes in three main forms, rock salt, cubic zincblende and hexagonal wurtzite, shown in Figure 2-1.

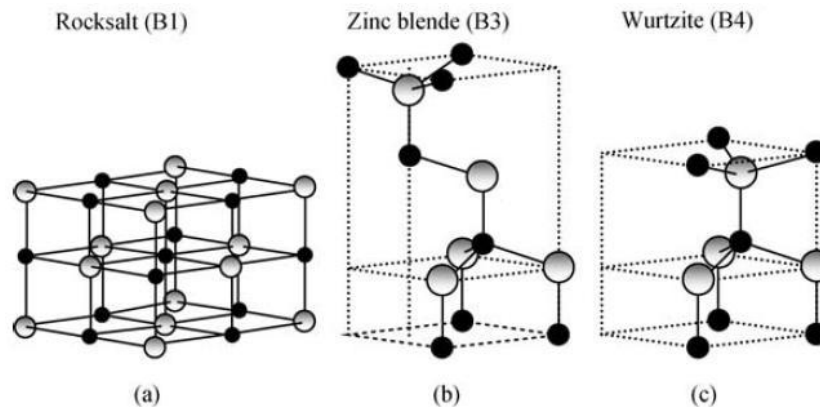


Figure 2-1 The rock salt (a), zincblende (b) and wurtzite (c) phases of ZnO. O atoms are shown as the bigger grey spheres, Zn atoms as the small black spheres. [59]

In the rocksalt structure, each Zn (or O) has six nearest neighbors. The space group symmetry of the rocksalt type of structure is $Fm\bar{3}m$ in the Hermann-Mauguin notation and O_h^5 in the Schoenflies notation and the structure is sixfold coordinated. However, the rocksalt structure cannot be stabilized by the epitaxial growth.

In the zincblende and wurtzite structures, the zinc and oxide centers are tetrahedral. In contrast to the rocksalt structure, each Zn (or O) has four nearest neighbors; the in-plane bonds are stronger than the out-of-plane bonds as indicated by higher electron density. The zincblende form has lower ionicity comparing to the wurtzite form. The symmetry of the zinc blende structure is given by space group $F\bar{4}3m$ in the Hermann-Mauguin notation and T_d^2 in the

Schoenflies notation and is composed of two interpenetrating face-centered cubic (fcc) sublattices shifted along the body diagonal by one-quarter of the length of the body diagonal. Zincblende ZnO has lower carrier scattering and higher doping efficiencies for the application.

The wurtzite structure is most stable at ambient conditions and thus most common due to its ionicity that resides exactly at the borderline between the covalent and the ionic materials. The wurtzite structure has a hexagonal unit cell with two lattice parameters a and c in the ratio of $\frac{c}{a} = \sqrt{\frac{8}{3}} = 1.633$ (in an ideal wurtzite structure) and belongs to the space group C_{6v}^4 in the Schoenflies notation and $P6_3mc$ in the Hermann–Mauguin notation. A schematic representation of the wurtzitic ZnO structure is shown in Figure 2-2. The structure is composed of two interpenetrating hexagonal closepacked (hcp) sublattices, each of which consists of one type of atom displaced with respect to each other along the threefold c -axis by the amount of $u = \frac{3}{8} = 0.375$ (in an ideal wurtzite structure) in fractional coordinates. The internal parameter u is defined as the length of the bond parallel to the c -axis divided by the c lattice parameter.

In addition, a potential application and the integrity of ZnO with conventional electronic application is also prime consideration in the choice of host materials. A ZnO-based DMS would be very promising because of its widespread application in electronic devices such as gas sensors, surface acoustic wave devices, optical wave guides, acousto-optic modulators, ultraviolet laser source and detectors.

2.2 Transition metal doped ZnO (ZnO:TM) DMS

Ferromagnetic phase is expected in TM ions doped ZnO [33, 37, 60-62]. In such system, exploitation of charge of the electron as well as the spin is possible. Different techniques such as pulsed laser deposition (PLD), sputtering, thermal evaporation and condensation, solid state reaction and chemical methods have been employed to fabricate such materials [63-68].

The remarkable progress has been made on realization of TM-doped ZnO such as cobalt-doped ZnO (ZnO:Co), iron-doped ZnO (ZnO:Fe), and manganese-doped ZnO (ZnO:Mn) with T_C at or above room temperature.

2.2.1 Cobalt-doped ZnO (ZnO:Co)

ZnO doped with Co is considered as the useful semiconductor which can be prepared by various methods. ZnO:Co films were prepared on sapphire substrate through PLD method by Rode *et al.* [69]. The in-plane structure of the ZnO:Co film was hexagonal and that its unit cell was rotated 30° with the respect to the sapphire substrate. It was found that the experimental result of $1.3 \pm 0.2 \mu_B$ per Co atom (μ_B/Co) was roughly half of the calculational result of $3 \mu_B/\text{Co}$ in a tetrahedral crystal field. This was ascribed to antiferromagnetic coupling between neighboring magnetic ions due to superexchange interaction. [18] The origin of the ferromagnetism in ZnO:Co was ruled out from the possibility of cobalt clusters. Because the ferromagnetic films of ZnO:Co were insulating at 10 K, it

was speculated that the free electrons, induced by oxygen vacancies, mediated the ferromagnetic exchange interactions. Fouchet *et al.*[70] also pointed that a high number of defects in the film were necessary to obtain ferromagnetism. These defects were most probably associated to the oxygen vacancies which can tune the strength of the magnetization in agreement with the model of Coey.[71]

Local Co structure in ZnO:Co films was also discussed. [72] Co is in the +2 valence state in ZnO:Co films. It was confirmed that Co^{2+} solute in the ZnO lattice sites substitutes for Zn^{2+} . Structural defects mechanism played an important role in the phenomenon of ferromagnetic ordering in the doped films. The structural defect dependent room temperature ferromagnetism may remain generally consistent with a bound magnetic polaron (BMP).[73] In the case of structural defects giving rise to charged point defects, the interaction of the hydrogenic electrons with Co^{2+} at appropriate distances could be realized in the impurity band on the basis of a Heisenberg exchange Hamiltonian, [74] which tends to form BMPs, coupling the $3d$ moments of the Co^{2+} ions within their volume λ^3 . The radius of hydrogenic orbital can be defined by $\lambda = \varepsilon_r(m/m_e)$, where ε_r is the dielectric constant, m is the electron mass, and m_e is the effective mass of the donor electrons. [71] Moreover, the hydrogenic orbital tends to sufficiently spread out to overlap other BMPs to achieve a ferromagnetic ordering between the polarons. The magnetization as a function of substrates revealed that the combination of ZnO:Co film grown on ferroelectric substrates and a suitable Co-O bond length likely serves as a key in ferromagnetic ordering.[75]

Dietl [76] also studied detailed ZnO:Co films depositing on sapphire by sputtering. The easy plane of ZnO:Co films was found perpendicular to the c axis of the wurtzite structure. Samples showed strong anisotropy: magnetization was significantly larger for the in-plane magnetic field. This indicated that the shape magnetic anisotropy was overcompensated by the crystalline magnetic anisotropy. The presence of a robust ferromagnetism was quite different from the theory of the electron-mediated spin-spin interaction in DMS.[77] The ferromagnetic signatures in the absence of ferromagnetic precipitate of Co clusters resulted from uncompensated spins at the surface of the antiferromagnetic nanocrystals. The nanocrystal aggregation could be steered by growth conditions and codoping,[78] as the position of the Fermi level affects the charge state and the diffusion coefficient of transition metals in semiconductors.

Liu *et al.* [79] investigated the high T_C ferromagnetic ZnO:Co were grown by radio frequency (RF) oxygen plasma-assisted molecular beam epitaxy (OPAMBE). In their work, as-grown single crystalline ZnO:Co thin films are ferromagnetic with T_C above room temperature. The coercivity of the hysteresis loops is about 150 Oe. The magnitude of the magnetization depends on the Co content. With increasing Co content, the saturation magnetization increases. The origin of the high T_C ferromagnetism of ZnO:Co thin films were suggested from the percolation of BMP. [80] Only those of Co^{2+} locating on the intersection of two BMPs contributed to long range magnetic interactions.

2.2.2 Iron-doped ZnO (ZnO:Fe)

Iron-doped ZnO (ZnO:Fe) is another typical ZnO-based DMS. The origin of the ferromagnetism in ZnO:Fe was attributed to the secondary phase of ZnFe_2O_4 in the ZnO:Fe.[81] This secondary phase possesses an inverted spinel structure and is ferrimagnetic at room temperature. The ferromagnetism in ZnO:Fe from the secondary phase, while the majority of Fe ions substituted into the ZnO lattices appears to remain magnetically inert.

ZnO:Fe single crystals also showed ferromagnetism at room temperature.[82] The origin of the ferromagnetic properties of ZnO:Fe was interpreted as the formation of metallic Fe nanoparticles due to higher migration of Fe at the elevated temperature during the implantation. Moreover, the required diffusion length for nanoparticle formation is much shorter at the higher fluence. In the case of diluted Fe^{3+} ($5 \mu_B$ per ion), 28% and in the case of diluted Fe^{2+} ($6 \mu_B$ per ion), 23% of the implanted ions would contribute to the ferromagnetic interaction. Each implanted Fe ion possessed the magnetic moment of $0.30 \mu_B$.

The *a*-plane ZnO:Fe epitaxial films by high dose ions implantation showed the ferromagnetic behavior in ZnO:Fe up to 300 K.[61] The Fe ion oxidation states in ZnO are considered critical to the magnetic properties. Substitutional Fe^{2+} and Fe^{3+} ions in the ZnO lattices were studied using paramagnetic resonance.[83, 84] The 5D state of the free Fe^{2+} ($3d^6$) ion is split under perturbation of the tetrahedral crystal field, spin-orbit interaction, and trigonal field in ZnO lattices. Similarly, these perturbations split the levels of the 6S ground state of the Fe^{3+} ($3d^5$) ion. The Fe ion pairs coupled through indirect ways is the origin of the

ferromagnetism.

Debernardi *et al.*[85] reported on the calculation, by density functional theory, of the total energy and of the magnetic properties of wurtzite ZnO doped with diluted Fe impurities in the presence of vacancies. They found that the complex $\text{Fe}_{\text{Zn}}\text{-V}_{\text{Zn}}$ is energetically favored compared with the isolated Fe_{Zn} and V_{Zn} . An opposite situation was obtained for Fe_{Zn} and V_{O} . The complex $\text{Fe}_{\text{Zn}}\text{-V}_{\text{O}}$ is realized with V_{O} along the c axis. Fe has a magnetic moment of $3.49 \mu_B$ that induces on the oxygen atoms in the xy plane a magnetic polarization of the p orbitals of about $0.14 \mu_B$ for each oxygen atom. The total magnetization per supercell of $4.00 \mu_B$ is integer, since the surface density of states (SDOS) is fully polarized at ϵ_F . At the Fermi energy the majority SDOS vanishes, while the minority SDOS presents one-electron state. A minority spin density is localized at the vacancy site and is antiferromagnetically coupled with the majority spin density localized at the Fe atom. For Zn-poor growth condition, the $\text{Fe}_{\text{Zn}}\text{-V}_{\text{Zn}}$ complexes strongly influence the magnetism of the compound at room temperature and present a fully polarized spin density at the Fermi energy.

2.2.3 Manganese-doped ZnO (ZnO:Mn)

Mn-doped ZnO (ZnO:Mn) has attracted attention similarly because of the theoretical predictions that p -type ZnO:Mn was ferromagnetic with a high Curie temperature above 300 K.[12, 71, 86] In many literatures, ferromagnetism was observed in ZnO:Mn films fabricated by Mn ions implantation,[87] pulsed laser deposition,[88] reactive cosputtering from Zn and Mn targets,[89] and radio

frequency magnetron sputtering.[90] Theoretical investigations using *ab initio* calculations [25, 91] suggested that ferromagnetic ordering of Mn ions is favored when it is mediated by hole doping. The presence of numbers of oxygen vacancies in the films could activate the high temperature ferromagnetism. Oxygen vacancies constituted bound magnetic polarons (BMPs) because the greater density of oxygen vacancies could yield a greater overall volume occupied by BMPs and increased their probability of overlapping, which results in the long-range Mn-Mn ferromagnetic coupling. Thus the observed ferromagnetism in the ZnO:Mn films could be explained in terms of a direct ferromagnetic coupling between two neighboring Mn ions near the oxygen vacancies.

2.3 Carbon-doped ZnO (ZnO:C)

The literatures mentioned above indicated that Co-, Fe- and Mn-doped ZnO with T_C above room temperature have been fabricated by many different types of methods. The transition metal ions have partially filled *d* and *f* shells, respectively, which give rise to unpaired electrons. The ferromagnetism in some ZnO:TM systems was induced by incorporation into substitutional sites of large concentration of transition metal ions into the semiconductor.

However, the different ZnO:TM systems produced inconsistent results even some groups have found no ferromagnetism in ZnO:Co and ZnO:Mn based semiconductors. The origin of ferromagnetism was ascribed to the different mechanisms in different ZnO:TM systems such as spin-split-orbit model [92],

double-exchange mechanism [38], superexchange coupling mechanism,[23] which means the mechanism of ferromagnetism remains unclear. Moreover, a major challenge is to prevent formation of secondary phases that may dominate the magnetic properties of the doped semiconductor because it is found that various magnetic impurity phases exist in many samples [93-96] and the dopants often have a clustering tendency which implies that ferromagnetism may originate from nonuniform distributions of dopants. All of these promoted search for ZnO-based DMS with alternative dopants. If non-TM dopants can be incorporated into ZnO and induce magnetism, DMS thus produced would not suffer from problems related to precipitates of dopants since they do not contribute to ferromagnetism.

Ferromagnetism was reported in a number of carbon systems [39-43]. Some of these studies have speculated that intrinsic carbon defects could be responsible for the observed magnetic properties. Carbon atoms on carbon nanotubes [44] and carbon substitutional doping in boron nitride nanotubes [45] were predicted to induce magnetism in the respective systems.

Pan *et al.*[46] explored the possibility of using carbon as a dopant to produce ZnO based DMS by using first-principles calculations. He predicted a magnetic moment of $2.02 \mu_B$ per carbon atom (μ_B/C) when carbon substitutes oxygen in ZnO and regarded the Zn-C system as the origin of magnetism in ZnO:C. The experiments confirmed the presence of carbon atoms in the carbide form, indicating carbon substitution for oxygen and formation of Zn-C bonds in the ZnO:C thin films. Based on the experimental results and calculated band

structures, Pan proposed hole mediation as the mechanism of ferromagnetic coupling in ZnO:C.

Ye [48] studied ZnO:C powders prepared by the standard solid-state reaction method. According to the results of Raman spectroscopy investigation, the samples sintered in nitrogen showed lower D-band (disordered) and G-band (graphitic) concentrations, plausibly a result of nitrogen incorporation into the ZnO:C sample. All the samples are ferromagnetic at room temperature. The authors considered the electron-mediated mechanism is more suitable than the hole-mediated one for the explanation of ferromagnetism of ZnO:C materials.

Then, Peng *et al.* [49] pointed hole-induced magnetization in oxides is an intrinsic host property when enough homogeneous holes are injected into the system. Acceptor doping or quantum confinement can increase local hole concentration at the anion site so that the local density of states (LDOS) at the Fermi level and the exchange interaction are large; thus, magnetization can be achieved with a reasonable amount of global hole concentration. The authors demonstrated also that localization of the holes by dopants and quantum confinement effect can reduce the critical hole concentration for stabilizing magnetization. Thus it is of interest to study the ferromagnetism in ZnO:C nanostructures.

Kwak *et al.* [50] examined the role of quantum confinement on the ZnO:C nanocrystals using a real space first-principles method. The spin polarization energy of a nanocrystal was found to be sensitive to size owing to the partial occupancy of a less-localized minority spin state. Their analysis suggests that the

semiconductor with nonmagnetically induced magnetic moments should provide a significant advantage over the traditional DMS when applied to nanometer-scaled applications.

Nagare [51] reported the spin-polarized density functional calculations of ferromagnetic properties for a series of ZnO clusters and ZnO solid containing one or two substitutional carbon impurities. He analyzed the eigenvalue spectra, spin densities, molecular orbitals, and induced magnetic moments for Zn-C, Zn₂C, Zn₂OC, carbon-substituted Zn_nO_n (n = 3~10, 12) clusters and the bulk ZnO. The results showed that the doping induces magnetic moment of about 2 μ_B in all the cases. All systems with two carbon impurities showed ferromagnetic interaction, except when carbon atoms shared the same zinc atom as the nearest neighbor. This ferromagnetic interaction was predominantly mediated via π -bonds in the ring structures and through π - and σ -bonds in the three-dimensional structure. The calculations also showed that the interaction is significantly enhanced in the solid, bringing out the role of dimensionality of the Zn-O network connecting two carbon atoms.

Therefore, choosing carbon as the dopant for ZnO-based DMS is feasible. ZnO:C DMS could not suffer from the problems related to precipitates of dopants. In addition, the dimensionality is known to play a significant role in determining various properties. The behavior of carriers in nanostructures may also allow for the enhancement of the ferromagnetic semiconductor behavior because nanostructures are expected to have longer coherence times than in films. Thus both ZnO:C thin films and nanoneedles were investigated.

CHAPTER 3

Experimental and methodology

3.1 Sample fabrication methodology

3.1.1 Filtered cathodic vacuum arc technique

The filtered cathodic vacuum arc (FCVA) technique has been studied extensively since it was reported to be an effective method of producing high quality, dense coating films. In such a technique, a particle filter is used to separate and remove macroparticles from the cathodic arc plasma.[97-99] Various filter designs have been described in the literature; the most popular one is the classic 90° bend filter, but straight filters, 20°, 45° and S-duct filters have also been tested. Although these filters may achieve acceptable results for some applications, the problem of macroparticles inclusion in the deposited film is not completely addressed. This is because the solid macroparticles are easily multiply reflected from the filter wall, leading to incomplete filtering. This problem thus impedes the commercial usefulness of this technology for the production of high quality optical and electronic coatings. In an effort to further reduce the macroparticles, an off-plane double bend (OPDB) filter [100] has been developed.

The OPDB filter comprises three straight pieces and two tori. These two tori are actually 90° bends cut to the required angle. The plasma transmission and macroparticles efficiency of this "serpentine" filter now commercially available.

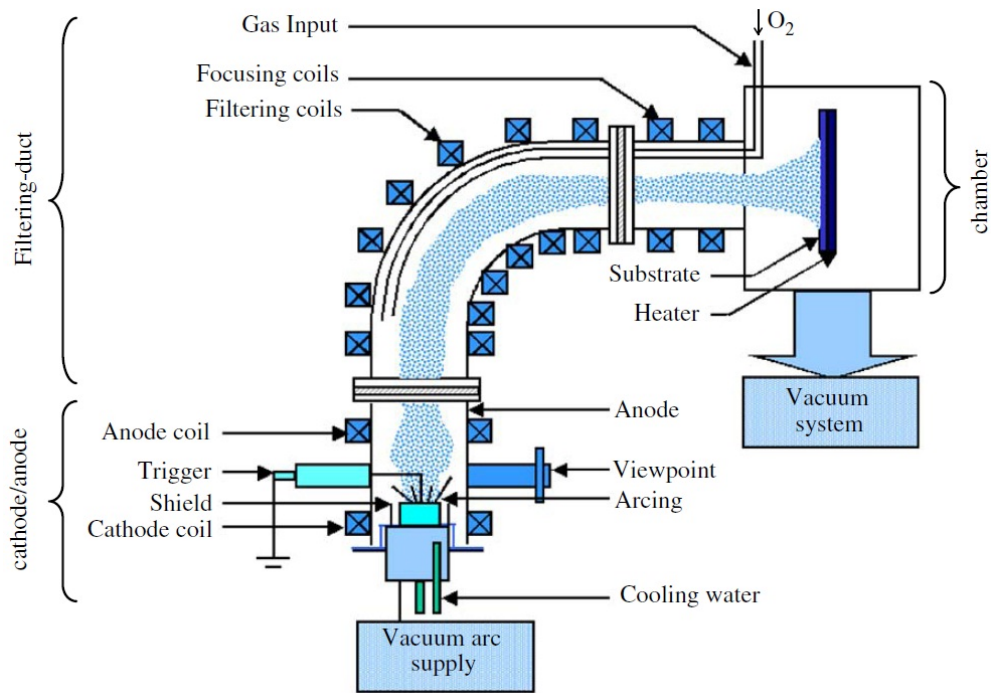


Figure 3-1 Schematic diagram of the FCVA system.

Figure 3-1 illustrates the schematic of the FCVA system for the deposition of ZnO thin films. The system consists of a cathodic vacuum arc source (anode–cathode coils), an OPDB plasma-filtering duct and a deposition chamber. When the trigger is struck on the metal target of Zn, energetic plasma ions from the metal target are formed. The plasma ions are then guided by the magnetic field inside the plasma-filtering duct. The filtering duct has two-torus bends with respect to axis of the cathodic vacuum arc source. The exterior wall of the filtering duct is surrounded by a set of magnetic coils for the generation of magnetic field to guide the plasma ions. The interior wall of the filtering duct is equipped with baffles that are designed to catch or to reflect macroparticles. Oxygen is introduced inside the filtering duct through an outlet along the OPDB filter such that metal-oxide plasma can be formed. The filtering duct is the most

important part of the FCVA system because it can effectively remove macroparticles from the metal-oxide plasma. The metal-oxide plasma will then be deposited on the substrate inside the deposition chamber. Because of the high kinetic energy of the metal-oxide plasma, the FCVA system can allow: (1) low-temperature deposition of ZnO thin films [101], (2) the deposition on lattice mismatched substrate [102], and (3) the use of large substrate (i.e., substrate diameter can be as large as 40 cm) [103] so that it is possible to achieve low-cost and mass-production of high quality ZnO thin films [104, 105].

3.1.2 Ion beam irradiation technique

Recently, various methods have been reported for the fabrication of one dimensional (1D) ferromagnetic ZnO:TM nanostructures such as direct hydrothermal synthesis [106], vapor transport [107, 108], chemical vapor deposition [109, 110], thermal evaporation [111], combustion [112], and laser-ablation methods [113] etc.. These techniques usually use catalysts and additives to control the nanostructure growth, leading to suspicious observed ferromagnetism. Exploring simple, cheap, catalyst-free, low-temperature methods of synthesizing vertically aligned 1D ZnO nanostructures remains a challenge. Energetic ions can create nanostructures on a surface or in the surface-near region of any kind of solid at room temperature [114]. The fabrication mechanism induced by sputtering of solid surfaces and the formation kinetics is mainly determined by etching instead of growth [115]. In modern sputtering model, surface atoms are ejected into a vacuum from an ion-impacting point via

a collision cascade in the projectile-implanted subsurface. The ion beam irradiation (IBI) technique has been proved to entail the formation of nanosized tips, conical protrusions and microcones structures of carbon and Si [116-118].

In this study, IBI technique was used to fabricate ZnO:C thin films and nanoneedles. The ZnO:C thin films and nanoneedles were fabricated in an ultra-high vacuum (UHV) system comprising micro-beam ion gun (JEOL MIED) and an arc-plasma gun (ULVAC APG-1000). The schematics of experimental setups are shown in Figure 3-2. The ion gun operated under an UHV ambient with Ar^+ ions was irradiated at an incidence angle of 45° to the graphite plate and the ZnO surface inside a vacuum system, carbon was doped into the host material. For the fabrication of doped thin films, the carbon ions were doped directly into the ZnO films through the irradiation of ion beams as shown in Figure 3-2(a). For the fabrication of doped nanoneedles, prior to the carbon doping, a thin carbon layer was deposited on the surface of the ZnO sample which would enhance the formation of nanoneedles during ion beam irradiation [119-121] as shown in Figure 3-2(b).

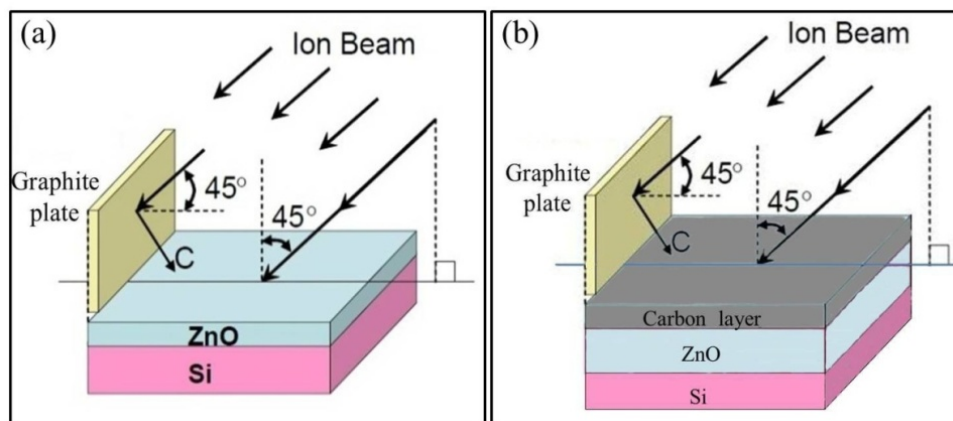


Figure 3-2 Schematic diagrams of the fabrication of (a) ZnO:C thin films and (b) ZnO:C nanoneedles by IBI technique.

Figure 3-3 depicts the formation mechanism of the ZnO:C nanoneedles by ion beam irradiation. Ar^+ ions are simultaneously irradiated onto the carbon-coated ZnO film and graphite plate as shown in Figure 3-3(a). The carbon needles are first formed from the carbon layer on the surface of the sample (Figure 3-3(b)). Further, continuous ion beam irradiation depletes the carbon layer and the carbon needles are decreasing gradually in length. The carbon needles act as a mask against the irradiation erosion which lead to the formation of slender cone-shape ZnO structures as shown in Figure 3-3(c). At the same time, carbon atoms from the graphite plate are doped into the ZnO with the side facing the graphite plate. The needle-like ZnO:C is developed progressively. When the carbon layer and carbon needles are eroded completely, ZnO:C nanoneedles are formed as shown in Figure 3-3(d).

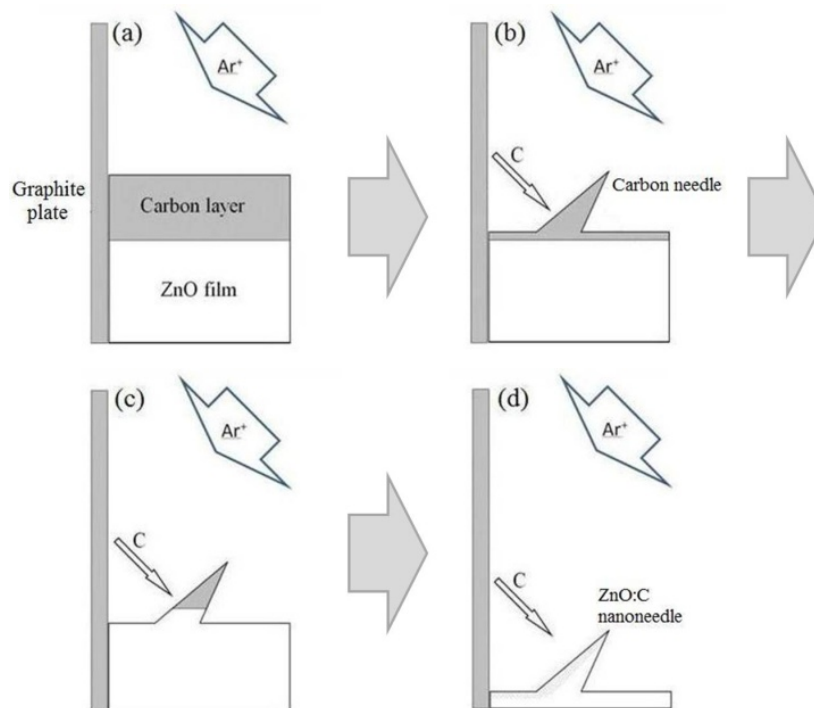


Figure 3-3 Schematic diagram of the formation mechanism of the ZnO:C nanoneedles. (a) Ar^+ ions are irradiated onto the graphite target and carbon layer, (b) formation of the carbon needles, (c) carbon needles acted as a mask against the sputter erosion for the formation of ZnO:C nanoneedles.

The chamber was pumped down to about 10^{-7} Torr, and the pressure remained at 10^{-6} Torr during the irradiation process. Prior to characterization, the residue of carbon layer was removed by ethanol. Ion beam irradiation of thin film surfaces provides a controlled and cost effective process for the formation of doped semiconductors and regular aligned nanostructures array at room temperature. This ion beam irradiation technique offers several advantages over other fabrication methods: (1) room temperature fabrication, (2) catalyst-free, (3) selectively growth of nanostructures, and (4) on any substrates.

3.2 Sample characterization methodology

3.2.1 X-ray diffraction

X-ray diffraction (XRD) is a powerful non-destructive technique for characterizing crystalline materials, which provides information on structures, phases, preferred crystal orientations (texture) and other structural parameters such as average grain size, crystallinity, strains and crystal defects. X-rays have high energies and short wavelength. When an incident beam of X-ray hit on a solid material, a portion of the beam would be scattered in all directions by the electrons. Also, the crystalline solid consists of a regular array of atoms; it may form a natural three-dimension diffraction grating for X-rays. The interaction of the incident rays with the sample produces constructive interference (and a diffracted ray) when conditions satisfy Bragg's Law:

$$n\lambda = 2d \sin \theta$$

where d is the distance between atomic layers in a crystal, and λ is the wavelength of the incident X-ray beam; n is an integer; θ is the diffraction angle in degrees. So, the atomic arrangements in the crystal could be deduced by X-ray diffraction.

And the crystallite size (t , nm), can be calculated from Scherrer's equation:

$$t = \frac{C\lambda}{B \cos \theta}$$

where λ is the X-ray wavelength (nm), B is the full width at half maximum (FWHM) of the peak (radians) corrected for instrumental broadening, θ is the Bragg angle, C is a factor (typically 1.0) that depends on the crystallite shape.

All the XRD measurements were carried out by Cu K_{α} ($\lambda = 0.154$ nm) radiation on X-ray diffractometer (Siemens D8 discover, 40 kV, 40 mA). Diffractograms were recorded from 30° to 60° with a step of 0.01° .

3.2.2 Energy dispersive X-ray spectroscopy

Energy-dispersive X-ray spectroscopy (EDX) is an analytical technique used for the elemental analysis or chemical characterization of a sample. It is one of the variants of X-ray fluorescence spectroscopy which relies on the investigation of a sample through interactions between electromagnetic radiation and matter. As the electron beam of the scanning electron microscope (SEM) is scanned across the sample surface, it generates X-ray fluorescence from the atoms in its path. The energy of each X-ray photon is characteristic of the element which produced

it. Basing on these data of energy, this technique can identify the elemental composition of the samples imaged in a scanning electron microscope for all elements with an atomic number greater than boron. Most elements are detected at concentrations on the order of 0.1 at.%.

3.2.3 X-ray absorption near-edge fine structure spectroscopy

X-ray absorption near-edge fine structure spectroscopy (XANES) is a type of absorption spectroscopy which is a powerful structural tool that provides information on the electronic structure and orientation of molecules or molecular fragments.

During a measurement, the sample is irradiated with monochromatic X-rays. The energy of the X-rays is varied around an ionization edge. The dominant process in the X-ray energy range is photoabsorption. The absorption process results in a photoelectron and a core hole. The hole is subsequently filled by an electron either radiatively by the emission of a fluorescent photon, or non-radiatively by the emission of an Auger electron (see Figure 3-4). Both channels are a direct measure of the existence of a core hole created by the X-ray absorption and are therefore a measure of the absorption cross section. XANES can probes the transitions from (usually) the *K*-edge (deepest core shell) of an atomic species into molecular orbitals of bonds to intra-molecular and extra-molecular (surface atoms) neighbors.

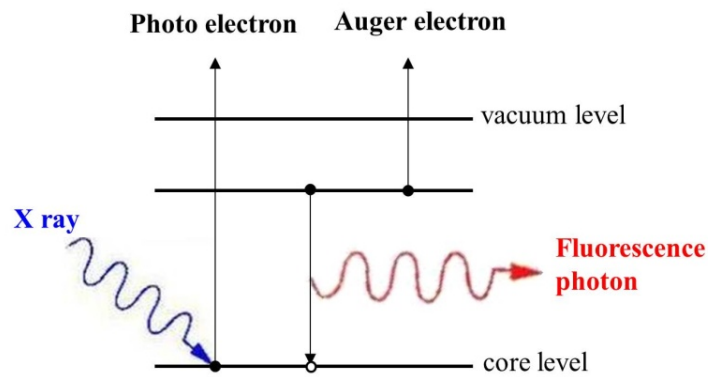


Figure 3-4 Energy diagram of the fundamental photoabsorption processes and the subsequent filling of the core hole by emission of a photon or an Auger electron which contribute to XANES spectra.

3.2.4 Field emission scanning electron microscopy

Field emission scanning electron microscopy (FESEM) is a very useful tool for high resolution surface imaging in the fields of nanomaterials science. In a field emission scanning electron microscope, comparing to the conventional SEM, no heating but a so-called "cold" source is employed. Field emission is the emission of electrons from the surface of a conductor caused by a strong electric field. An extremely thin and sharp tungsten needle (tip diameter 10-100 nm) works as a cathode. The field emission source reasonably combines with scanning electron microscopes whose development has been supported by advances in secondary electron detector technology. FESEM can produce clearer, less electrostatically distorted images with spatial resolution down to 2 nm. That's 5 times better than conventional SEM. It can reduce the penetration of low kinetic energy electrons probes closer to the immediate material surface. So FESEM is used usually for the semiconductor's surface and cross section analyzing for the widths, thicknesses, construction details and structure uniformity determination. Our

samples were studied by using FESEM (JEOL JSM-6335F). The acceleration voltage between cathode and anode was 20 kV, and the vacuum in the column of the microscope was about 5×10^{-4} Pa.

3.2.5 Transmission electron microscopy

Transmission electron microscopy (TEM) is a microscopy technique whereby a beam of electrons is transmitted through an ultra-thin specimen, interacting with the specimen as it passes through. It is a powerful tool for analysis of structure and devices with nano-meter scale dimensions. The instrument consists of an electro-magnetic lens furnished with an electron source. A monochromatic electron beam is accelerated and converged by electromagnetic lenses and apertures by varying the currents. The TEM collects the electrons that are transmitted through the specimen and an image is formed; the image is magnified and focused onto an imaging device, such as a fluorescent screen, on a layer of photographic film, or to be detected by a sensor. For crystalline materials, the specimen diffracts the incident electron beam, producing local diffraction intensity variations that can be translated into contrast to form an image. This technique is used for analyzing the morphology, crystallographic structure, and even composition of a specimen. Compared to SEM, TEM has better spatial resolution and can facilitate the analysis of features at atomic scale (in the range of a few nanometers) using electron beam energies in the range of 60 to 350 keV, is capable of additional analytical measurements, and requires significantly more sample preparation.

3.2.6 High resolution transmission electron microscopy

High resolution transmission electron microscopy (HRTEM) is the ultimate tool in imaging defects. It is an imaging mode of TEM that has been widely and effectively used for analyzing crystal structures and lattice imperfections in various kinds of advanced materials on an atomic scale. HRTEM can provide structural information at better than 0.2 nm spatial resolution. In most crystalline inorganic materials, including ceramics, semiconductors, and metals, the positions of individual atomic columns can be resolved. When recorded under optimum conditions, electron micrographs can be directly interpreted in terms of the projected crystal potential. In other cases, image simulations are necessary to match proposed structures to image features.

3.2.7 Electron energy loss spectroscopy

Electron energy loss spectroscopy (EELS) can be applied with several techniques, but always involves the bombardment of a sample with a monoenergetic beam of electrons. The technique is frequently used in association with transmission electron microscopy. It is perhaps one of the best methods for the elements ranging from carbon through the 3*d* transition metals.

In EELS, a material is exposed to a beam of electrons with a known, narrow range of kinetic energies. Energy loss occurs because of inelastic scattering by both inner-shell and outer-shell electrons present in the specimen. The amount of

energy loss can be measured via an electron spectrometer and interpreted in terms of what caused the energy loss. These losses can reveal the composition of the sample in TEM. Because the analyzing region can be selected from a part of the enlarged electron microscopic image, one can analyze very small region. Moreover, by selecting electrons with specific loss energy by a slit so as to image them, element distribution in specimen can be visualized

3.2.8 Atomic force microscopy

The atomic force microscopy (AFM) is a high-resolution type of scanning probe microscopy, with demonstrated resolution of fractions of a nanometer. It is widely used in both industrial and fundamental research to obtain atomic-scale images of materials surfaces. It provides a three-dimensional profile of the surface which is very useful for characterizing surface roughness, observing surface defects, and determining the size and conformation of molecules and aggregates on the surface.

The probe is placed on the end of a flexible cantilever, as shown in Figure 3-5. The AFM probe tip gently touches the surface and records the small force between the probe and the surface. The motion of the tip across the surface is controlled using feedback loop and piezoelectric (PZT) scanner. A semiconductor diode laser is bounced off the back of the cantilever onto a position sensitive photodiode detector. This detector measures the bending of cantilever during the tip is scanned over the sample. The measured cantilever deflections are used to generate a map of the surface topography.

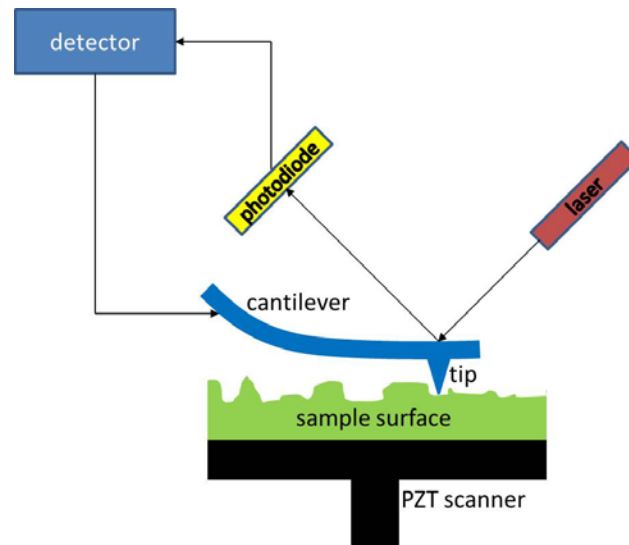


Figure 3-5 Schematic diagram of AFM.

The primary modes of operation for an AFM are the contact mode and tapping mode. In the contact mode operation, the force between the tip and the surface is kept constant during scanning by maintaining a constant deflection. The static tip deflection is used as a feedback signal. Because the measurement of a static signal is prone to noise and drift, low stiffness cantilevers are used to boost the deflection signal. However, close to the surface of the sample, attractive forces can be quite strong, causing the tip to "snap-in" to the surface. In order to prevent the tip from sticking to the surface, tapping mode was developed to bypass this problem. In tapping mode, the cantilever is driven to oscillate up and down at near its resonance frequency by a small piezoelectric element mounted in the AFM tip holder. An electronic servo uses the piezoelectric actuator to control the height of the cantilever above the sample. The servo adjusts the height to maintain a set cantilever oscillation amplitude as the cantilever is scanned over the sample. A tapping AFM image is therefore produced by imaging the force of the intermittent contacts of the tip with the sample surface.[122] This method of

"tapping" lessens the damage done to the surface and the tip compared to the amount done in contact mode. The topography of our samples was investigated by AFM (Veeco SPM-8) with the tapping mode.

3.2.9 Magnetic force microscopy

Magnetic force microscopy (MFM) images the spatial variation of magnetic forces on a sample surface. For MFM, the tip is coated with a ferromagnetic thin film. The system operates in non-contact mode, detecting changes in the resonant frequency of the cantilever induced by the magnetic field's dependence on tip-to-sample separation (shown in Figure 3-6). MFM can be used to image naturally occurring and deliberately written domain structures in magnetic materials.

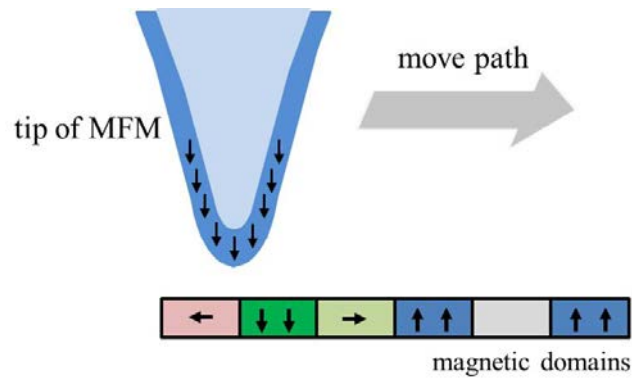


Figure 3-6 Schematic diagram of MFM.

3.2.10 Photoluminescence spectroscopy

Photoluminescence (PL) spectroscopy is a contactless, nondestructive method to probe the electronic structure of materials. The spectral distribution of PL from a

semiconductor can be analyzed to nondestructively determine the electronic bandgap.

In photoluminescence spectrometer, the light with particular wavelength is excited to illuminate the sample, where it is absorbed imparts excess energy into the material. This process is called photo-excitation. Photo-excitation causes electrons within the material to move into permissible excited states. When these electrons return to their equilibrium states, the excess energy is released and may include the emission of light. In the case of photo-excitation, this luminescence is called photoluminescence. The energy of the emitted light relates to the difference in energy levels between the two electron states involved in the transition between the excited state and the equilibrium state. The quantity of the emitted light is related to the relative contribution of the radiative process.

The most common radiative transition in semiconductors is between states in the conduction and valence bands, with the energy difference being known as the band gap. Radiative transitions in semiconductors also involve localized defect levels. The photoluminescence energy associated with these levels can be used to identify specific defects, and the amount of photoluminescence can be used to determine their concentration.

The PL spectra of the ZnO and ZnO:C at room temperature were studied by photoluminescence spectroscopy (Edinburgh FLSP920) under optical excitation by Xe lamp with a wavelength of 324 nm.

3.2.11 Vibrating sample magnetometer

Vibrating sample magnetometer (VSM) is a scientific instrument that measures magnetic properties. The schematic and configuration of VSM is shown in Figure 3-7. A sample is placed inside a uniform magnetic field to magnetize the sample. The sample is then physically vibrated sinusoidally, typically through the use of a piezoelectric material. The magnetic flux through a nearby detection coil varies sinusoidally. The induced voltage in the detection coil is proportional to the sample's magnetic moment, but does not depend on the strength of the applied magnetic field. In a typical setup, the induced voltage is measured by using the piezoelectric signal as its reference signal. By measuring the field of an external electromagnet, it is possible to obtain the hysteresis curve of a material.

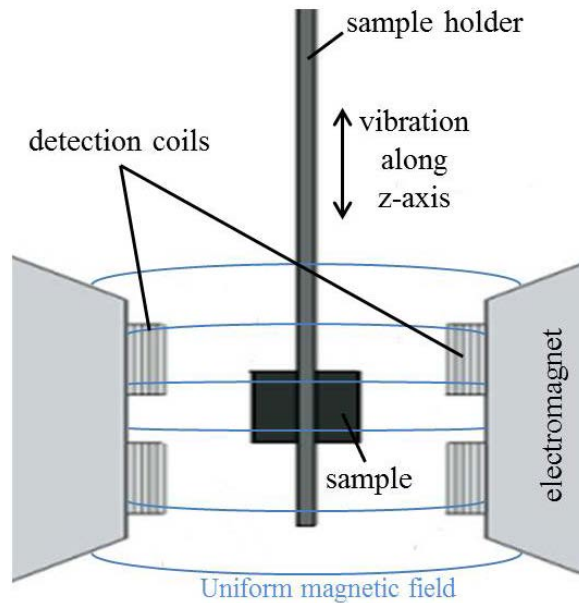


Figure 3-7 Sample holder and detection mechanism of VSM.

VSM was used heavily in this work in order to characterize the magnetic properties of the ZnO:C. The magnetic sample is mounted on the end of a

cantilevered rod that incorporates a piezoelectric element. The sample is magnetized by a uniform magnetic field, so $\frac{dH}{dt} = 0$ (H is the magnetic field and t is time) and a dipole moment (M_0) is induced in the sample. When sample is vibrating in magnetic field at a fixed frequency (ω), the magnetic moment (M) is generated and $M = M_0 \sin \omega t$. Then, a sinusoidal electrical signal can be induced in detection coils. According to Faraday's Law:

$$\varepsilon = -N \frac{d\Phi}{dt} = -N \frac{d(BA)}{dt} = -NA \frac{dB}{dt} = -NA\mu_0 \frac{d(H+M)}{dt} = -NA\mu_0 M_0 \omega \cos \omega t$$

in where ε is induction potential; N is the number of coils; Φ is the magnetic flux ($=B \cdot A$); t is time; A is the area of coil. The signal is proportional to the magnetic moment, vibration amplitude and vibration frequency. The ideal sensitivity of instrument is 10^{-7} emu.

The vibrating sample magnetometer (Lakeshore VSM7407) was employed to measure the magnetic moment of the samples at room temperature. The range of uniform magnetic field is -2.0 to 2.0 Tesla.

3.2.12 Superconducting quantum interference device

Superconducting quantum interference devices (SQUID) are the world's most sensitive detectors of magnetic signals. SQUIDs have been used to measure extremely weak magnetic fields for a variety of testing purposes that demand extreme sensitivity, including engineering, medical, and geological equipment, besides their use in the laboratory. Because it measure changes in a magnetic

field with such sensitivity, it does not have to come in contact with the samples.

Typical SQUID configuration is showed in Figure 3-8.

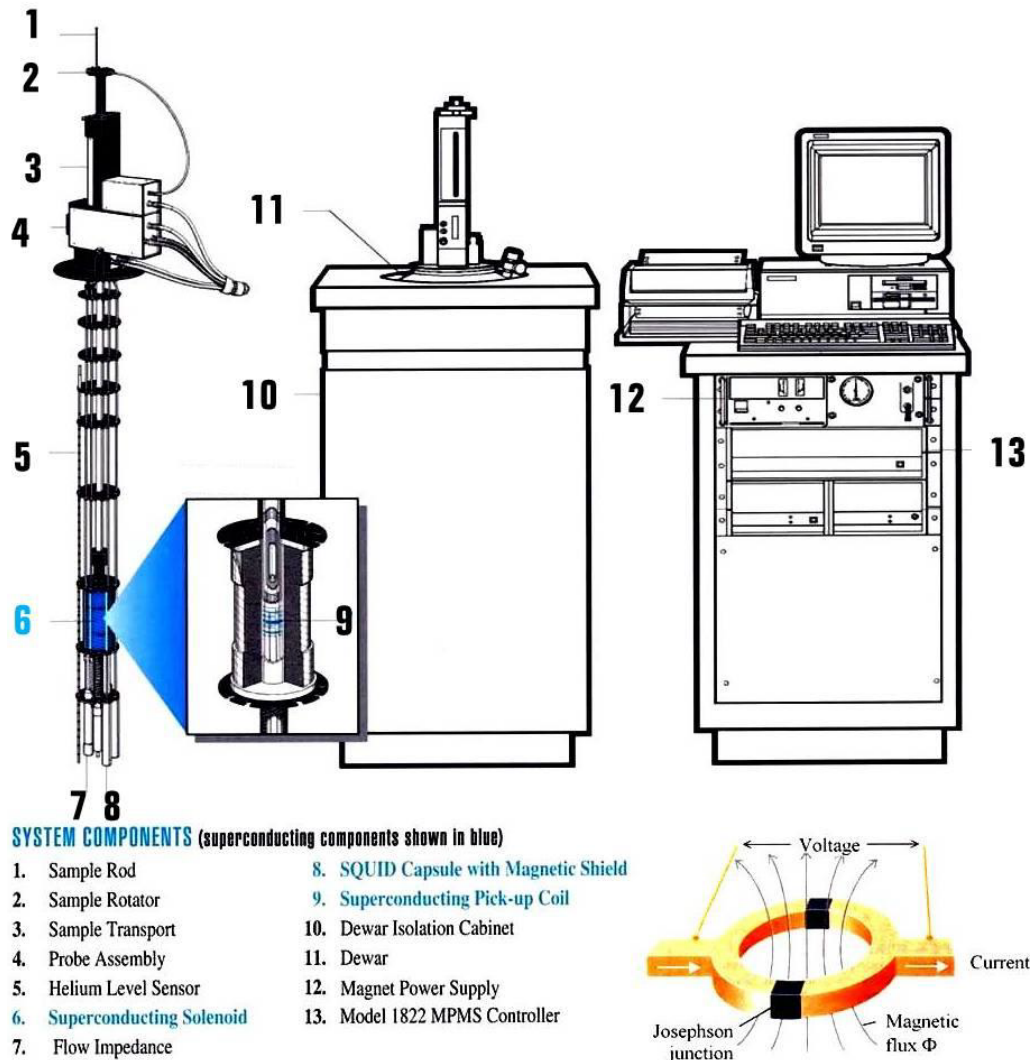


Figure 3-8 Configuration of SQUID. [From Quantum Design company]

A SQUID consists of a superconducting loop interrupted by either one or two Josephson junctions for the radio frequency (RF) or direct current (DC) SQUID, respectively. A Josephson junction is made up of two superconductors, separated by an insulating layer so thin that electrons can pass through [123]. When two

superconductors with different phases of the superconducting order parameters are connected through a weak link, tunneling current can flow between them. The tunneling current reaches minimum values at points where the applied magnetic flux is an integral multiple of the flux quantum. For DC SQUID, it consists of two Josephson junctions connected in parallel on a superconducting loop and is operated in the voltage state with a current bias. When the flux in the loop is increased, the voltage oscillates with a period Φ_0 ($\Phi_0 \equiv \frac{h}{2e}$, h is Planck's constant and e is the electron charge.). The quantum mechanical properties of the superconductor make this arrangement exquisitely sensitive to tiny changes in the local magnetic field. By detecting a small change in the voltage one is able to detect a change in flux typically as low as $10^{-6} \Phi_0$. The magnetic moments of samples can be characterized precisely and accurately in SQUID.

Besides the magnetic hysteresis loops, the zero field cooling (ZFC) - field cooling (FC) magnetization curves can be obtained directly also by SQUID. ZFC - FC magnetization curves are generally used to examine the magnetic types and properties of materials. They are measured in two different ways. ZFC is to cool the samples at zero magnetic field from room temperature to low temperature (lower than the characteristic temperature of samples) and then to apply a field at this low temperature and continuously to measure the effects of the field as raising the temperature to a level well above the characteristic level. FC is to apply the field at a relatively high temperature compared to a characteristic temperature and continuously to measure the effects of the field as lowering the temperature to a level well below the characteristic level. FC can be thought of as

the reverse process to ZFC. If the ZFC-FC magnetization curves are lining up on top of each other, the sample has no magnetic interaction such as paramagnetism and diamagnetism. If the ZFC-FC magnetization curves are almost the same, the sample is isotropic with the magnetic interaction in the long range. If the ZFC-FC magnetization curves have the significant differences such as the shape of branch or λ , the sample should be spin glass or superparamagnetism or changed in anisotropy, as shown in Figure 3-9.

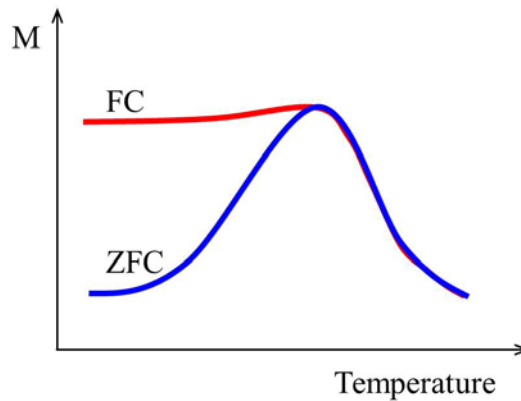


Figure 3-9 Diagram of the ZFC-FC magnetization curves.

In our works, SQUID (Quantum Design MPMS-5P) was employed to determine the magnetic moments of our samples not only at room temperature but also at low temperature down to 5K and at high temperature to 330 K. The results include the magnetic hysteresis loops (magnetic moment vs. field) and ZFC-FC magnetization curves. The magnetization absolute sensitivity of it is as low as 1×10^{-8} emu.

3.2.13 Transport properties measurement

For semiconductor materials, it yields the carrier concentration, its type, and carrier mobility [124]. The importance of the Hall effect is underscored by the need to determine carrier density, electrical resistivity, and the mobility of carriers accurately in semiconductors. More specifically, experimental data on Hall measurements over a wide temperature range provide quantitative information on impurities, imperfections, uniformity, scattering mechanisms, etc. The Hall coefficient (R_H) and resistivity (ρ) are experimentally determined and then related to the electrical parameters through (for n -type conduction) $R_H = r_H/ne$ and $\mu_H = R_H/\rho$, where n is the free-electron concentration, e is the unit electronic charge, μ_H is the Hall mobility, and r_H is the Hall scattering factor which is dependent on the particular scattering mechanism.

The transport properties of the samples were investigated by Lakeshore HMS 7507 system using the van der Pauw method in the temperature range from 80 K up to room temperature. Lakeshore HMS 7507 system is a turnkey, high performance system for the measurement of resistivity, carrier concentration, and mobility in semiconductors. The system has a uniform field of 0.55 Tesla over a radius of 3 cm and easily accommodates typical samples of area 4 cm². The capabilities of this system include the Hall coefficient, Hall resistance, resistivity, I-V curves, carrier density and mobility. It can measure samples with resistances ranging from 0.04 m Ω to 10 $\times 10^6$ Ω with less than 5% measurement uncertainty, carrier concentrations from 8 $\times 10^2$ to 8 $\times 10^{23}$ cm⁻³, hall mobility from 1 to 1 $\times 10^6$ cm²/VS. Prior to measurement, indium contact pads were made at the corner of

the samples. Then ohmic characteristic of the samples were tested before the Hall effect measurement. The measurements for the magnetoresistances of the samples were performed on a physical properties measurement system (PPMS) (Quantum Design PPMS-9) using the standard four-probe method in the temperature range from 5 K up to 330 K.

CHAPTER 4

Preparation of ZnO films

4.1 Introduction

The ZnO films were deposited on SiO₂/Si(100) substrates, which were mounted perpendicular to the direction of the plasma beam about 10 cm from the outlet of the filter bend. The substrates were cleaned ultrasonically using acetone, methanol and ionized water consequently, and then blown dry with nitrogen gas. Oxygen (purity 99.99%) was used as the reactive gas; its flow rate was controlled by a mass flow meter during deposition. The chamber was evacuated to a base pressure of 5×10^{-6} Torr before deposition. The chamber pressure decreases upon ignition of the arc, because oxygen gas is pumped by zinc plasma. So the pressure value used here was measured during the deposition process with arcing.

The quality of the ZnO as-grown films is very sensitive to some physical parameters such as the substrate temperature and the oxygen pressure in the chamber. The formation energy of the oxides related to the growth temperature which can also increase the thermodynamic stability of the oxides going from Zn plasma to ZnO. The sufficiency of oxygen in the reactive chamber controlled by the oxygen pressure determines the extent of reaction of the Zn plasma with oxygen gas turning into the ZnO films on the substrates. These two important parameters are direct influence the quality of ZnO films. In order to obtain the

ZnO films appropriate for the carbon doping, these two parameters were investigated.

The growth of ZnO films were carried out under different substrate temperatures from 200 to 400 °C (400 °C is the upper limit of our FCVA system) at various oxygen pressures ranging from 0.5 to 2 mTorr (0.5 mTorr is the lower limit of our FCVA system). The deposition time was adjusted to obtain films with thicknesses of about 600 nm.

4.2 Effect of substrate temperature

First the influence of substrate temperature on the quality of the ZnO films was studied. ZnO films were fabricated under various substrate temperatures from 200 to 400 °C. During the deposition, the oxygen pressure was maintained at 0.5 mTorr.

4.2.1 XRD structural characteristics

The crystal structure of the ZnO films was investigated by the XRD measurement. Figure 4-1 shows the XRD patterns of the ZnO thin films grown from 200 to 400 °C with the oxygen pressure of 0.5 mTorr. For the sample grown at 200 °C, no peak can be found in the XRD spectrum from 30 to 60° of 2θ . For each sample grown from 250 to 400 °C, it is observed that the ZnO films exhibit a (002) peak at 34.42° and no secondary phase is found. The dominant (002) peak indicates that the ZnO films have a hexagonal wurtzite structure with

their *c*-axis normal to the substrate-basal plane. The intensity of (002) peak at substrate temperature of 400 °C was the highest in all samples. It indicates the higher substrate temperature is more beneficial to the formation of high-crystal quality ZnO thin films.

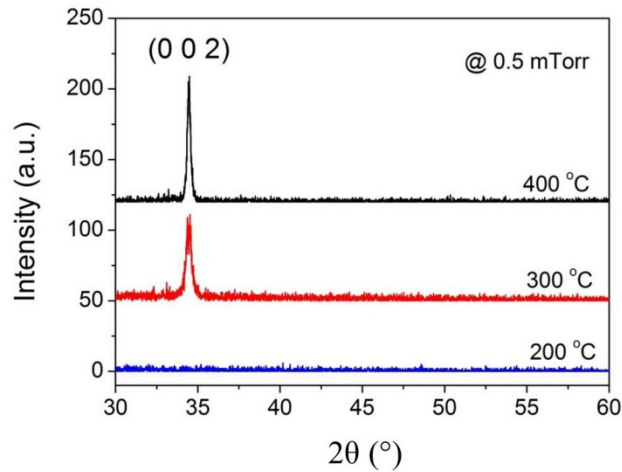


Figure 4-1 XRD patterns of the ZnO thin films grown at different temperatures with 0.5 mTorr oxygen pressure.

Table 4 summaries the structural properties of the ZnO films grown at 200, 300 and 400 °C with oxygen gas pressure of 0.5 mTorr extracted from XRD data. For samples grown at temperature above 300 °C, the interplanar crystal spacing of d_{002} and lattice parameter of *c* of the ZnO films is 0.2601 nm and 0.5202 nm, respectively. The grain size does increase from 22 nm at substrate temperature of 300 °C to 26 nm at 400 °C. It indicates that the thermal energy is helpful to the crystal quality of the ZnO films. Higher energy at higher substrate temperature impels the crystallization of films be better.

Table 4 FWHM, grain size, interplanar spacing and lattice parameter (c) of ZnO thin films grown at 200, 300 and 400 °C with 0.5 mTorr oxygen pressure.

Temp. (°C)	(002) position (°)	FWHM (°)	Grain size (nm)	d_{002} (nm)	c (nm)
200	--	--	--	--	--
300	34.42	0.382	22	0.2601	0.5202
400	34.42	0.319	26	0.2601	0.5202

4.2.2 Photoluminescence

The typical PL spectrum of ZnO film consists of two emission peaks, an excitonic related near band edge emission (NBE) in the ultraviolet region and a broad deep level emission band at around 610 nm [125]. At room temperature, the NBE is dominated by free excitonic recombination. The origin of the deep level emission band is still not well understood and has been ascribed to oxygen vacancies, oxygen interstitials and impurities.[126-128] The intensity ratio of the NBE emission to the deep level reveals the quality of the ZnO films.

Figure 4-2 shows the photoluminescence spectra of ZnO thin films grown at 200, 300 and 400 °C with 0.5 mTorr oxygen pressures. The ultraviolet (UV) emission corresponding to NBE emission is observed at around 378 nm (3.28 eV). As the substrate temperature increases, the UV peak position of the excitonic emission shifts from 374 to 378 nm which implies that the band gap narrowing effect occurred as the substrate temperature increases. The intensity of NBE emission is corresponding to the quality of the ZnO thin films. With the rising of the substrate temperature, the crystallinity of the ZnO film gets better due to the increasing of the thermal energy. This result is homologous to the XRD result.

The optimized substrate temperature for the ZnO films is determined to be as 400 °C.

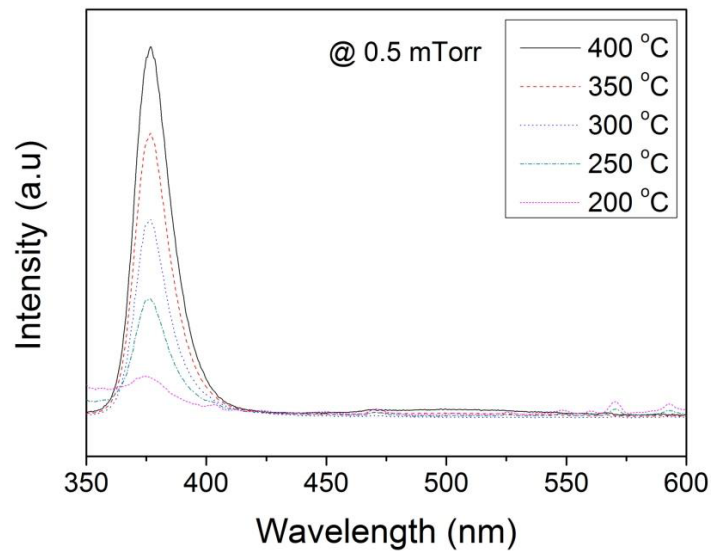


Figure 4-2 PL spectra of the ZnO thin films grown at 200, 300 and 400 °C with 0.5 mTorr oxygen pressure.

4.3 Effect of O₂ pressure

Since high temperature is better for the growth of high-crystal quality ZnO films, the substrate temperature was fixed at 400 °C. At this temperature, we studied the second important factor (i.e. gas pressure) for the fabrication of ZnO thin films.

4.3.1 XRD structural characteristics

Figure 4-3 shows the XRD patterns of the ZnO thin films grown at 400°C under different oxygen pressures from 0.5 to 2.0 mTorr. The (002) diffraction peaks at $2\theta = 34.42^\circ$ appears in the spectra, which indicates all the ZnO films formed the

hexagonal wurtzite crystal structure with their c axis perpendicular to the substrate surface. It shows that the ZnO films are of single phase with no detectable secondary phase within the sensitivity of the equipment.

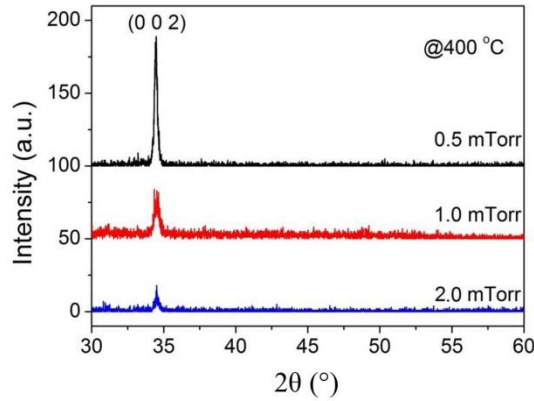


Figure 4-3 XRD patterns of the ZnO thin films grown at 400 ° with oxygen pressures of 0.5, 1.0 and 2.0 mTorr.

It is noteworthy that the intensity of the (002) decreases with the increase of the oxygen gas pressure from 0.5 mTorr to 2.0 mTorr. This behavior can be understood by two competing processes; the oxygen in the chamber is the necessary gas for the formation of ZnO thin films. The oxygen gas can improve the stoichiometry of the films and the crystal quality. On the other hand, the kinetic energy of the reactive particles in the cathodic plasma decreases due to high oxygen pressure, which limits surface diffusion of the growing atoms and thus degrades the film quality.

4.3.2 Photoluminescence

Photoluminescence spectra of the ZnO thin films were acquired at room temperature. Luminescent peaks are observed in the films grown under oxygen

pressures of 0.5, 1.0 and 2.0 mTorr at substrate temperature of 200, 300 and 400 °C as shown in Figure 4-4.

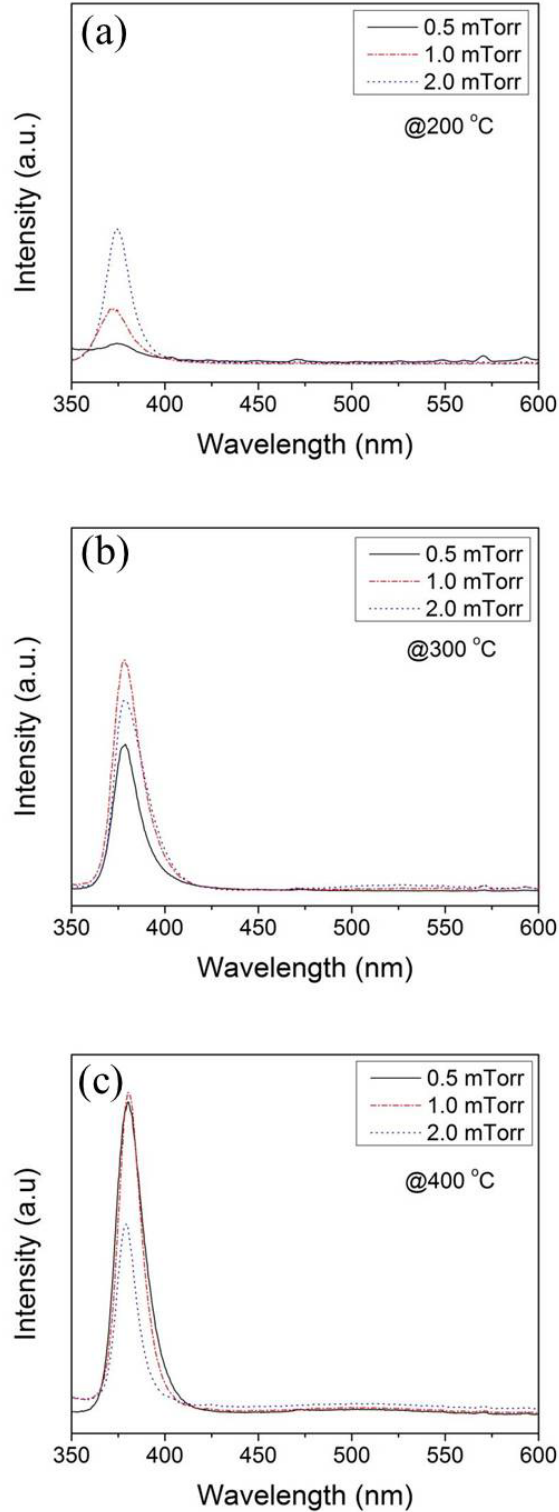


Figure 4-4 PL spectra of (a) the ZnO thin films grown at 200 °C, (b) 300 °C and (c) 400 °C with different oxygen pressures.

At 200 °C, the intensity of NBE peak at 378 nm is weak due to the poor crystal quality of the ZnO. With increasing the substrate temperature to 300 °C, the intensity of the NBE peak was enhanced and reached maximum when oxygen gas pressure was 1.0 mTorr, and then decreased at higher oxygen gas pressure. This behavior can be understood by two competing processes; the increase of oxygen pressure in the chamber improves the stoichiometry of the films and the crystal quality. On the other hand, the kinetic energy of the reactive particles in the cathodic plasma decreases due to high oxygen pressure, which limits surface diffusion of the growing atoms and thus degrades the film quality. At 400 °C, the intensity of the NBE peak is the strongest at 0.5 mTorr. The PL peak intensity decreases with further increase in oxygen gas pressure.

It indicates that the crystal quality of the ZnO films is very sensitive to the substrate temperature. At higher temperature, there is more thermal energy for the reactivation of Zn plasma with oxygen gas to form the ZnO thin film on the substrate surface so that the reaction is easier and more thorough. However, the overfilled O₂ is not helpful for improving the quality of the ZnO. When O₂ pressure is higher than 0.5 mTorr, the oxygen gas would reduce the kinetic energy of Zn ions in the plasma and it would hinder the efficient formation of Zn ions and oxygen atoms, leading to the reduction of crystal quality of the ZnO thin films.

The ZnO thin film grown at 400 °C with 0.5 mTorr of oxygen pressure exhibits a sharp and strong PL signal of NBE emission at the wavelength of 378 nm with a full width at half maximum of 13.86 nm, which is dominated by the free exciton

recombination. The appearance of the NBE with the relative high intensity shows the ZnO films are of high-crystal quality.

4.4 ZnO thin films prepared under optimized conditions

According to the above investigation, the optimized fabrication conditions for ZnO thin films were determined. The substrate temperature and oxygen gas pressure are 400 °C and 0.5 mTorr, respectively.

Figure 4-5 presents the typical surface and cross-sectional SEM images of the ZnO film. It is shown that a textured ZnO film grown on SiO₂/Si(100) without visible crack formation. No droplet is observed, confirming the high filtering efficiency of the filter used here. The thickness of the ZnO thin film is about 600 nm. The film displays a smooth, uniform grain size and void-free surface. From the cross-sectional image, it is seen that the film is composed of columnar-like structures, which is consistent with the highly (002) texture growth evidenced by the XRD analysis. The RMS (root mean square) roughness of the ZnO film was determined by AFM to be 10.3 nm.

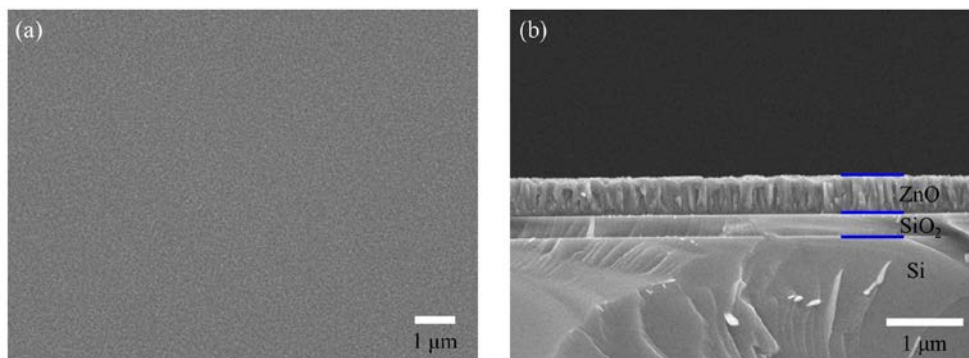


Figure 4-5 (a) Surface and (b) cross-sectional SEM images of the ZnO film grown at optimized conditions.

The electrical transport properties of the ZnO films were measured in a van der Pauw configuration utilizing a Lakeshore HMS 7507 system at room temperature. The ZnO films exhibit typical *n*-type semiconductor characteristics with resistivity of about 3.00 Ω·cm, as shown in Table 5. The carrier concentration and Hall mobility are $5.00 \times 10^{18} / \text{cm}^3$ and $1 \text{ cm}^2/\text{V}\cdot\text{s}$ respectively.

Table 5 Transport properties of ZnO thin film.

ZnO thin films	Value
Resistivity (Ω·cm)	3.00
Carrier concentration ($\times 10^{18}/\text{cm}^3$)	5.00
Hall mobility ($\text{cm}^2/\text{V}\cdot\text{s}$)	1
Type of conduction	<i>n</i>

4.5 Summary

In summary, the two important parameters for preparing ZnO films, substrate temperature and oxygen gas pressure, were investigated. Under the optimum conditions, 400 °C of substrate temperature and 0.5 mTorr of oxygen gas pressure, ZnO thin films with high-crystal quality can be obtained. The highly *c*-axis oriented films with wurtzite structure display a smooth, uniform grain size and void-free surface. The Hall measurement indicates that the room temperature resistivity was found to be 3 Ω·cm with Hall mobility of $1 \text{ cm}^2/\text{V}\cdot\text{s}$ and carrier concentration of $5 \times 10^{18}/\text{cm}^3$ for the optimized ZnO thin film.

CHAPTER 5

Preparation of ZnO:C by IBI

5.1 Effect of distance from the graphite plate

In order to dope C into the ZnO films with various concentrations, four ZnO samples were aligned with various specific distances in front of the graphite plate as shown in Figure 5-1. The distances between the samples (④, ③, ② and ①) and the graphite plate are 1, 1.5, 2 and 4 cm, respectively.

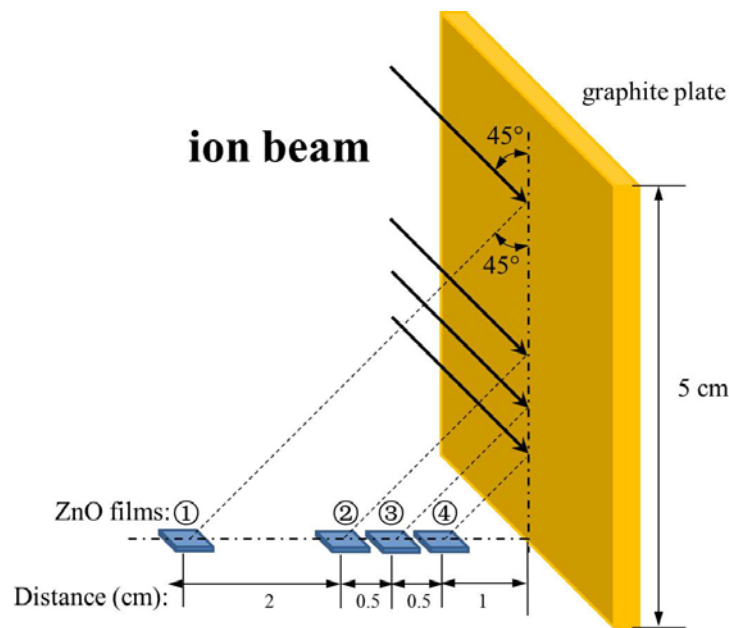


Figure 5-1 Schematic diagram of the experimental set up for doping various C concentration into ZnO films.

A beam of Ar^+ ions is irradiated at an incidence angle of 45° to the graphite plate and the ZnO samples surface. The emergence angle of the bombarded carbon

ions from the graphite plate is also 45° to the graphite plate and the ZnO surface. The ratio of the travelling distance of the carbon ions from the graphite plate to the sample ①, ②, ③ and ④ are 4:2:1.5:1. The sample nearest (i.e. sample ④) to the graphite plate is expected to receive the maximum amount of C ions. With an increase of separation distance from the graphite plate, the amount of C ions reaches the samples should decrease due to the energy loss of the C ions. The C concentration in the samples should be increased with the decrease of the distance from the graphite plate. So sample ① should receive minimum amount of C ions and the C concentration is expected to be inversely proportional to the distance between sample and the graphite plate.

In addition to the distance between the graphite plate and the ZnO sample, there are two other parameters which will affect the C concentration in the ZnO films which are ion beam energy and irradiation time. By increasing the ion beam energy, more C ions will be sputtered off from the graphite plate. The energy of the C ions will also increase which will affect the doping efficiency into ZnO. Prolonging the irradiation time will also increase the amount of C ions arriving onto the ZnO surface. On the other hand, the ion beam also etches the surface of the sample. By increasing either the ion beam energy or prolonging the irradiation time, the etching extent of the sample will increase.

Sample ④ is expected as the sample with the highest carbon concentration. Thus sample ④ was chosen for the study of the effect of ion beam energy and irradiation time to determine the optimum conditions for carbon doping.

5.2 Effect of ion beam energy

In order to investigate the effect of ion beam energy on the structural and magnetic properties of the ZnO:C thin films, ZnO thin films were irradiated by ion beam energies from 500 to 1000 eV with the same irradiation time of 3 minutes.

5.2.1 Atomic force microscopy

The surface morphology of the as-grown ZnO thin film and the ZnO:C thin films were characterized using the atomic force microscopy (AFM). Figure 5-2 shows the micrographs of the surface morphology of the ZnO films irradiated by ion beam with different ion beam energies.

After the irradiation, the films consist of dense and fairly uniform grain size. However, when the ion beam energy is more than 700 eV, some droplet-like particles could be observed on the surface of the films as shown in Figure 5-2(e) ~ (g). These droplet-like particles were identified by energy dispersive X-ray spectroscopy (EDX) as carbon dots. With increasing ion beam energy, the carbon dots accrued. It is due to the excessive bombarding of carbon ions from the graphite plate by the energetic ions. When the ion beam energy is greater than 800 eV, more carbon species reached the surface of the ZnO. The excess carbon ions accumulate at the surface of the thin films and form the carbon dots on the surface instead of doping into the ZnO thin films. Consequently, the ion beam energy of 700 eV may be appropriate for the fabrication of ZnO:C system.

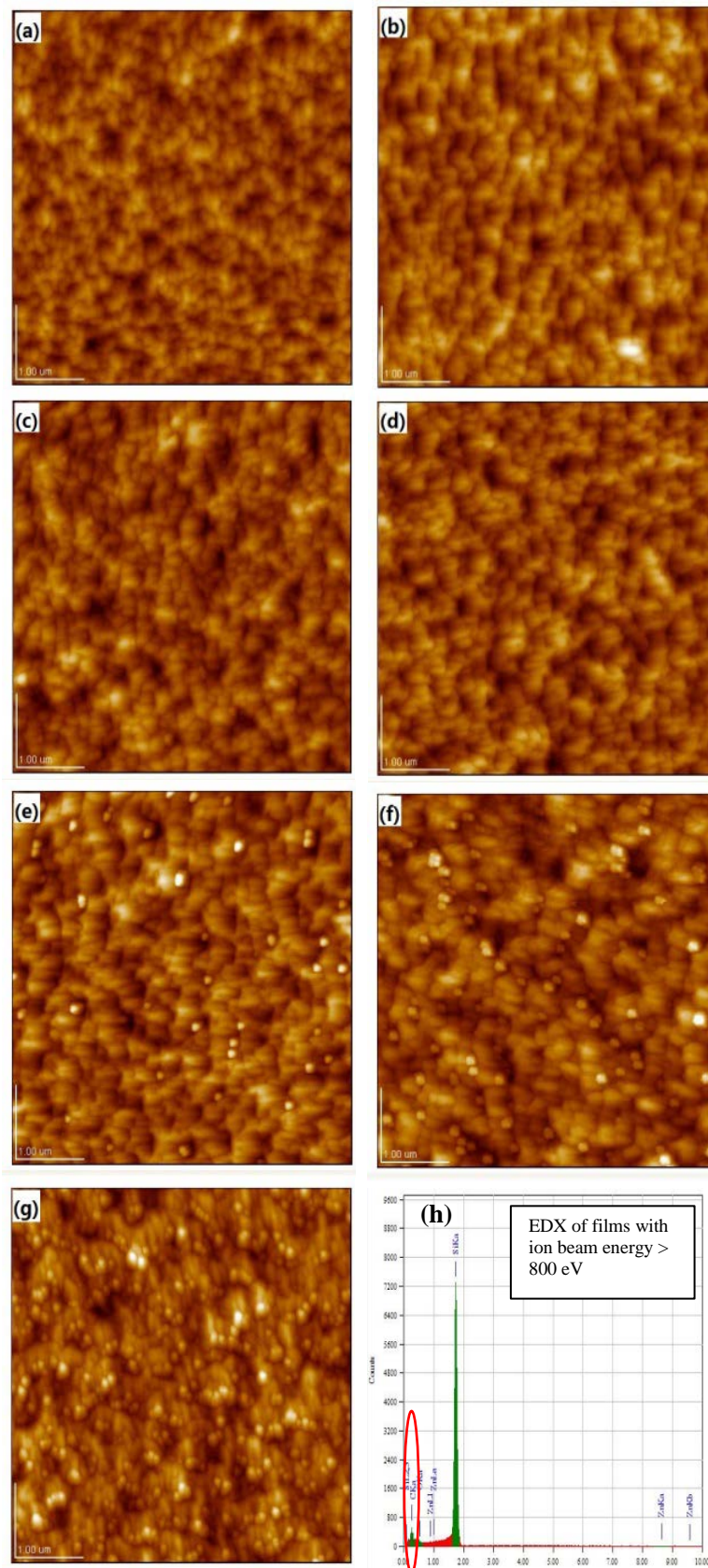


Figure 5-2 AFM micrographs of (a) as-grown ZnO, and ZnO:C thin films irradiated with different ion beam energies: (b) 500 eV, (c) 600 eV, (d) 700 eV, (e) 800 eV, (f) 900 eV, (g) 1000 eV. (h) Droplet-like particles were identified by EDX as carbon.

The roughness of these films after irradiation is presented in Table 6. The roughness of the as-grown ZnO thin film is 10 nm. The roughness of the ZnO:C thin films is increased from 10.5 to 19.4 nm with ion beam energies ranging from 500 eV to 1000 eV respectively.

Table 6 The roughness of the as-grown and irradiated ZnO thin films under different ion beam energies.

	As-grown	500 eV	600 eV	700 eV	800 eV	900 eV	1000 eV
Roughness (nm)	10	10.5	11.5	12.4	16.9	18.8	19.4

5.2.2 Magnetic properties

The ferromagnetic properties of these ZnO:C thin films were studied by SQUID. The magnetization (or magnetic moments) can be found in the hysteresis loops. The hysteresis loops as a function of ion beam energy is shown in Figure 5-3. When the ion beam energy is less than 700 eV, the hysteresis loops of the ZnO:C thin films were not clear due to the inconspicuous magnetic moments in the samples. Increasing the energy to 700 eV, a clear hysteresis loop could be seen. The saturated magnetization (M_s) is about 3.97 emu/cm^3 for the sample prepared at 700 eV. At 800 eV, M_s was about 2 times of that at 700 eV. However, with increasing the ion beam energy to 1000 eV, the magnetic moments of the samples do not increase further. It indicates that the threshold ion beam energy for the carbon doping in this system is about 700 eV.

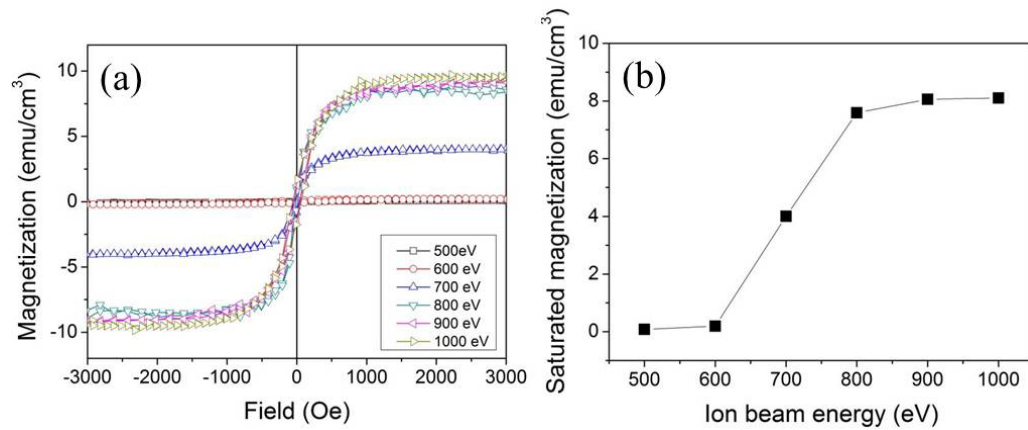


Figure 5-3 ZnO:C thin films were prepared under different ion beam energies. (a) The M-H loops of the ZnO:C thin films. (b) The dependence of saturated magnetizations of the ZnO:C thin films on the ion beam energies.

Although using ion beam energy of above 700 eV could produce ZnO:C with higher M_s , however, higher energy would induce excess carbon dots on the surface of the samples. In order to obtain the ZnO:C thin films with larger M_s without impurity on the surface, we selected the ion beam energy of 700 eV and then investigated the effect of irradiation time.

5.3 Effect of irradiation time

The effect of the irradiation time on magnetic properties of the ZnO:C thin films was investigated. The ion beam energy was fixed at 700 eV and the irradiation times were varied from 3 to 9 minutes.

5.3.1 Atomic force microscopy

Figure 5-4 shows the AFM micrographs of the ZnO:C thin films fabricated at 700 eV with different irradiation times. There is no droplet-like particle formed

on the surface of all the samples. It indicated that the doping rate of carbon ions is not changing remarkably with the irradiation time.

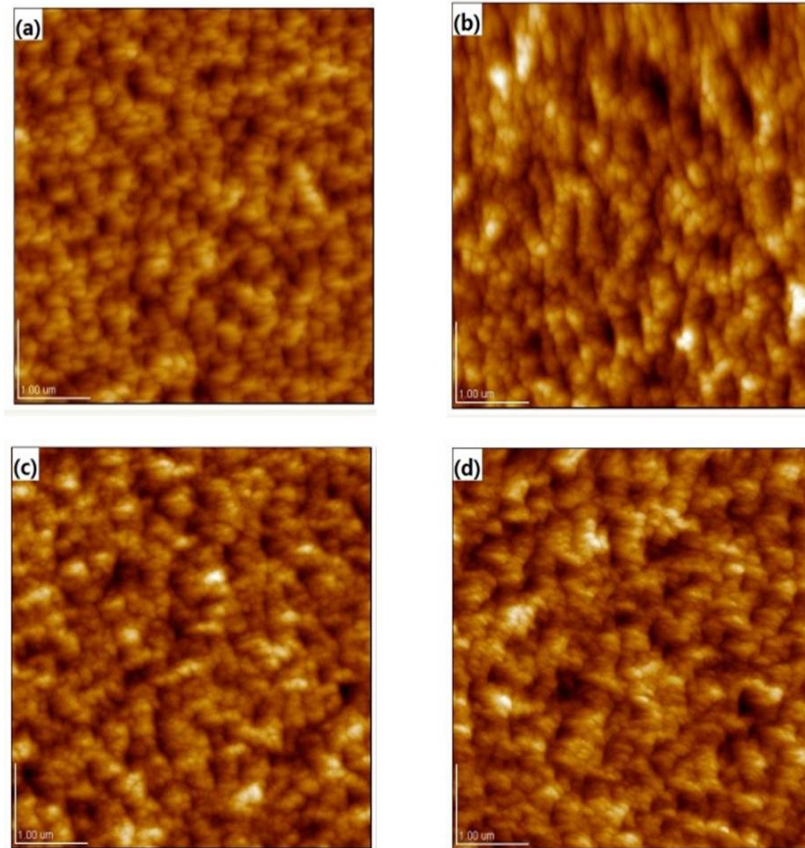


Figure 5-4 AFM micrographs of the ZnO:C thin films fabricated at 700 eV with different times (a) 3, (b) 5, (c) 7, (d) 9 minutes.

The roughness of these films is presented in Table 7. The roughness is increased slightly with prolonging the irradiation time from 3 minutes to 9 minutes. Comparing the roughness of the ZnO:C thin films prepared at different ion beam energies with different irradiation times, as shown in Figure 5-5, it can be found that the surface roughness of the ZnO:C thin films prepared at 700 eV with 3 minutes is less than those prepared at higher ion beam energies.

Table 7 The roughness of the as-grown ZnO thin films and irradiated ZnO thin films at 700 eV with irradiation time ranging from 3 to 9 minutes.

	As-grown	3mins	5mins	7mins	9mins
Roughness (nm)	10	12.4	13.0	14.1	16.3

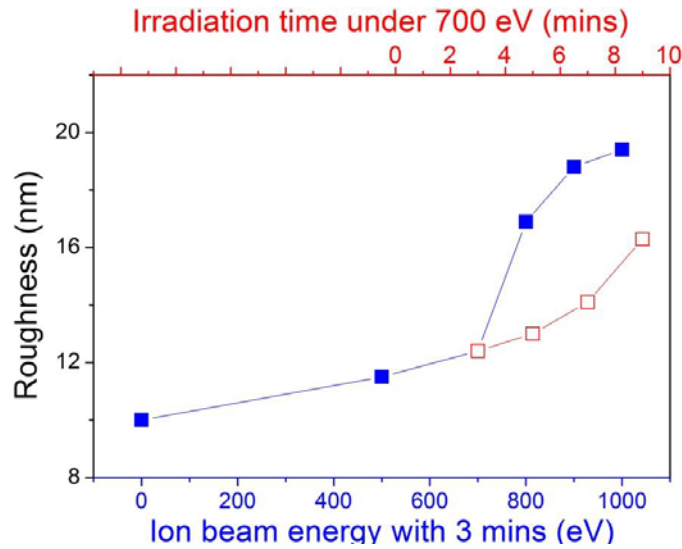


Figure 5-5 The roughness of the ZnO:C thin films fabricated at 700 eV with different irradiation times (open squares), comparing with the roughness of the films irradiated by the different ion beam energies (solid squares).

5.3.2 Magnetic properties

Figure 5-6(a) shows the M-H curves of the ZnO:C thin films prepared at 700 eV with irradiation times ranging from 3 to 9 minutes. The M_s is increased by a factor of 2 when the irradiation time increases from 3 to 4 minutes. It is worth noting that M_s increases slightly from 5 to 9 minutes. It indicates that the optimized growth conditions for the ferromagnetic ZnO:C is 7 minutes irradiation at 700 eV.

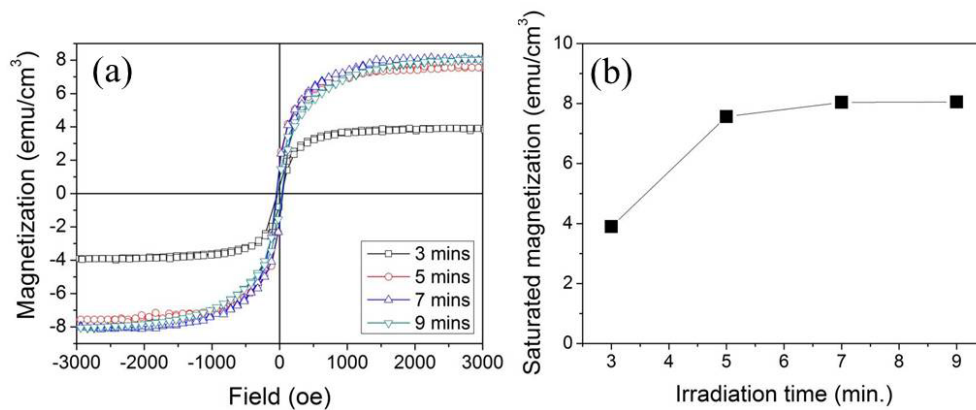


Figure 5-6 ZnO:C thin films were fabricated at 700eV with different irradiation times. (a) The M-H loops of the ZnO:C thin films prepared at different irradiation times. (b) The dependence of magnetic moment of the ZnO:C thin films on the irradiation time.

5.4 Summary

In summary, the ion beam irradiation technique is an effective method for the fabrication of ZnO:C system. The effects of ion beam energy and irradiation time on the samples were investigated. The optimized growth conditions for the ZnO:C thin films were determined to be 700 eV of ion beam energy with 7 minutes of irradiation time.

CHAPTER 6

Ferromagnetic ZnO:C thin films

6.1 Introduction

The ZnO:C thin films were fabricated by the FCVA and IBI techniques under the optimized conditions, 700 eV of ion beam energy and 7 minutes of irradiation time. The samples labeled as ①, ②, ③ and ④ represent various C concentrations. As discussed in Section 5.1, the C content in the samples ①, ②, ③ and ④ are increasing as samples ① and ④ being the lowest and highest C content respectively.

We attempted to quantify the carbon content in the samples by various techniques such as X-ray photoelectron spectroscopy, high-resolution transmission electron microscopy, electron energy loss spectroscopy, and X-ray absorption near-edge fine structure spectroscopy. However, we were not able to obtain reliable results which can determine the carbon content in the samples. Therefore, samples labeled as ①, ②, ③ and ④ are used throughout this thesis to represent various C contents in the samples.

VSM and SQUID were employed to study the magnetic properties of the ZnO:C thin films. Temperature dependent transport properties of the ZnO:C thin films were obtained. Microstructure and surface morphology of these films were investigated.

6.2 Structural characteristics

Figure 6-1 shows the X-ray diffraction (XRD) patterns of the ZnO and ZnO:C thin films. All the ZnO:C thin films exhibit a prominent *c*-axis (002) texture at 34.53° with high crystallinity, corresponding to a ZnO wurtzite structure. No trace of the impurities or graphite-related peaks can be detected within the scanning range of 30° to 60° .

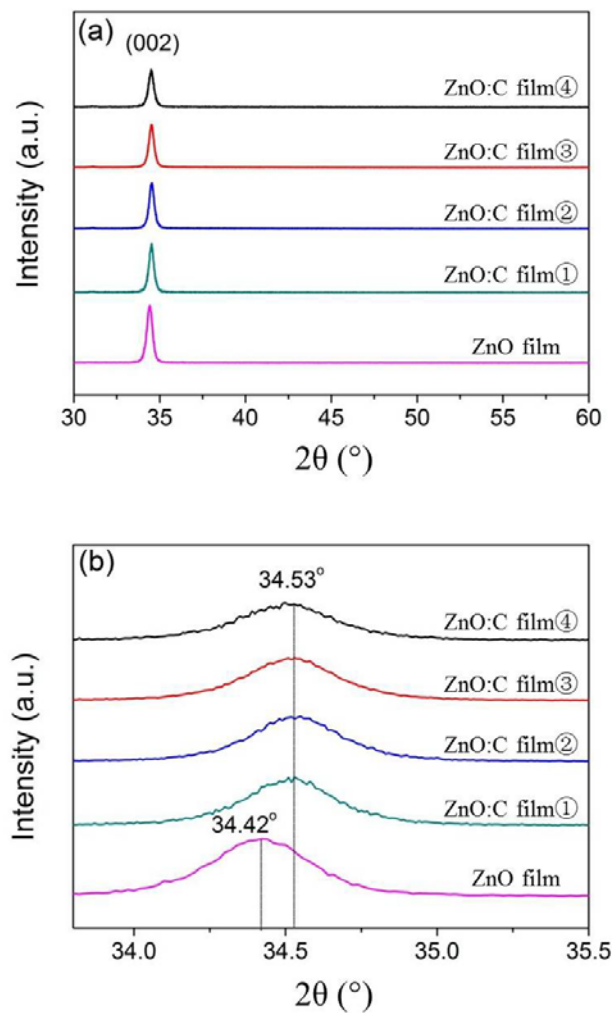


Figure 6-1 (a) XRD patterns of the ZnO thin film and ZnO:C thin films with different carbon concentration and (b) the expanded view of XRD patterns.

A shift of (002) peak to higher angle by 0.11° as compared to the as-grown ZnO

thin film is observed in the patterns of ZnO:C thin films. By the calculations through (1) Bragg law and (2) formula of lattice constants,

$$n\lambda = 2d \sin \theta \quad (1)$$

$$a = d \sqrt{\frac{4}{3}(h^2 + hk + k^2) + l^2 \left(\frac{a}{c}\right)^2} \quad (2)$$

where n is an integer, λ is the wavelength of incident wave, d is the spacing between the planes in the atomic lattice, a and c are the lattice constants, h , k and l are Miller indices of the plane. The lattice constant c of (002) plane can be calculated. It reveals that the lattice constant c of the ZnO:C thin films is reduced by 0.309% as compared to the ZnO thin film. The radius of Zn^{2+} , O^{2-} and covalent carbon are 0.74\AA , 1.40\AA and 0.77\AA respectively. The radius of covalent carbon is smaller than the radius of O^{2-} . The reduction of lattice constant c with carbon doping is expected as smaller C ions substituted into the O sites of ZnO lattices.

6.3 Ferromagnetic properties

6.3.1 M-H loops

Figure 6-2 shows the magnetic hysteresis loops of the ZnO:C thin films at room temperature with different carbon concentrations. All the samples exhibit ferromagnetic ordering with clear hysteresis loops. M_s of the ZnO:C thin films is increasing with the increase of the carbon concentration in the ZnO:C.

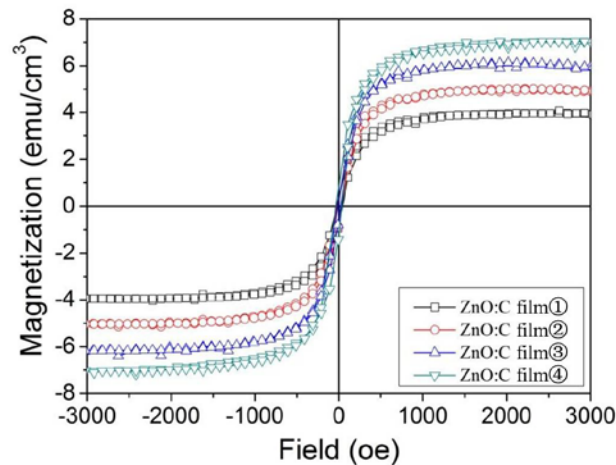


Figure 6-2 The magnetization hysteresis loops of the ZnO:C thin films with different carbon concentrations at room temperature.

Figure 6-3 shows the magnetic hysteresis loops of the ZnO:C thin film (film ①) at 5 and 300 K. M_s of the samples increases by 50% from 4.08 emu/cm^3 at 300 K to 6.12 emu/cm^3 at 5 K. It is worthwhile to highlight that no ferromagnetism can be observed from the as-grown ZnO and the ion beam irradiated sample in the absence of the graphite plate under identical growth conditions. A large enhancement in coercivity is detected at low temperature. The coercivity (H_C) is found in the order of 50 Oe at 300 K; then it is surged to 150 Oe at 5 K, as illustrated in the inset of Figure 6-3. This broadening effect is a classical behavior of magnetic materials at low temperature. According to Stoner-Wohlfarth's model [129], the magnetocrystalline anisotropy of materials at a given temperature can be considered simply as to be proportional to the product of M_s and H_C . As to our ZnO:C thin film, both M_s and H_C increasing with the decreasing of the temperature suggest that the ferromagnetic anisotropy of ZnO:C thin film is enhanced remarkably at low temperature.

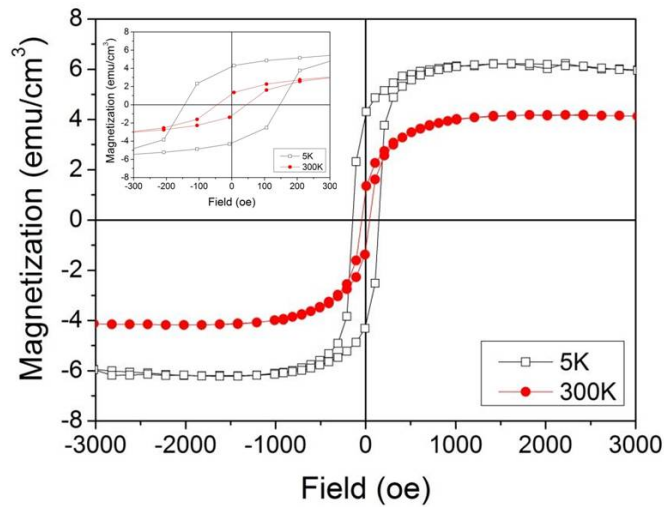


Figure 6-3 The hysteresis loops of the ZnO:C (film ①) film at 5 and 300 K. The inset shows the expanded view of the hysteresis loops.

6.3.2 ZFC-FC magnetization curves

The ZFC-FC magnetization curves of the ZnO:C thin film (film ①) measured under applied field of 50 Oe are shown in Figure 6-4. The sample exhibits a Curie temperature above 330 K. The magnetization increases with an increase in temperature from 5 K up to a transition temperature (T_T) of 216, and then the magnetization decreases with temperature greater than T_T . This convex shape of ZFC-FC curve reflects antiferromagnetic and ferromagnetic transition near T_T . Focusing on ZnO:C thin films (film ①), for $T < 216$ K, a pronounced antiferromagnetic interaction is observed. However, the ferromagnetic phase is still strongly dominant over the whole range of temperatures. The cusp in the ZFC and FC magnetization is typically interpreted as an indication of spin-glass behavior [46], attributing to the frustration originating from the coexistence of ferromagnetic and antiferromagnetic interactions.

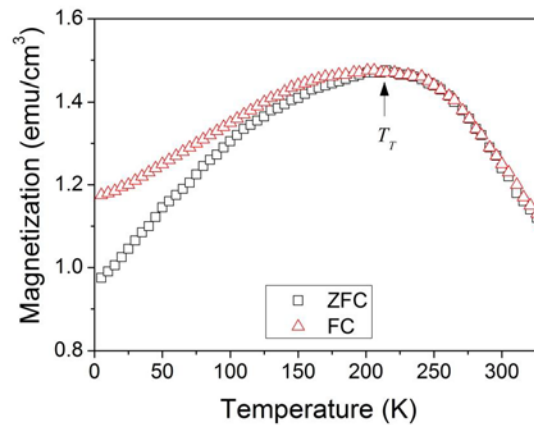


Figure 6-4 The ZFC-FC magnetization curves for the ZnO:C thin film (film ①) measured at magnetic field of 50 Oe.

6.3.3 Magnetic force microscopy

Figure 6-5 shows the magnetic force microscopy (MFM) micrograph of the ZnO:C thin film (film ②). It is found that the MFM amplitude image shows the points distribution in the area of $25 \mu\text{m}^2$ (Figure 6-5(a)) on the surface of the ZnO:C thin film. In order to judge the relationship between the MFM micrograph and the surface topography of the ZnO:C thin film, the scan area was shrunk to $1 \mu\text{m}^2$. The speckle-like structures are shown in MFM amplitude image (Figure 6-5(b)) which is not evident from the corresponding topography image (Figure 6-5(c)). The average diameter of these speckles is about 200 nm. The distribution of the speckle-like magnetic domains in the ZnO:C thin film is related to the process of the ion beam irradiation technique. During the irradiation, the C ions should be bombarded out of the graphite plate to form cluster of the carbon ions. The C ions should arrive at the surface of the ZnO thin film randomly. The areas where the C ions were doped into should show the magnetic domains as the speckle structure. Other places are nonmagnetic.

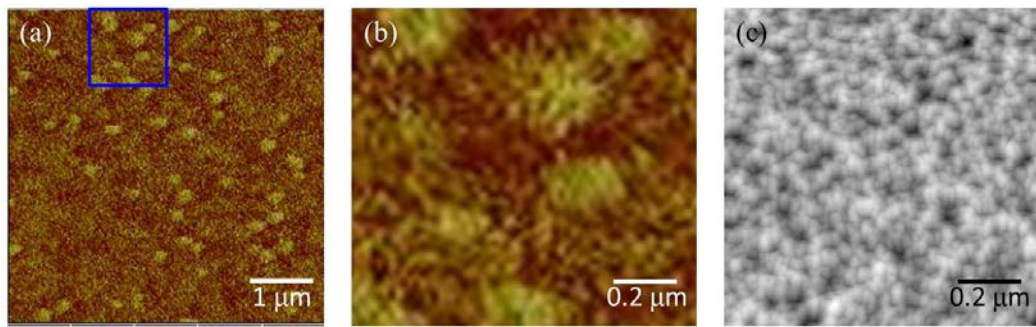


Figure 6-5 (a) The MFM micrograph of the ZnO:C thin film (film ②); (b) the expanded view of the MFM micrograph; (c) the correspond AFM micrograph of the ZnO:C thin film in the same area of (b).

6.4 Transport properties

6.4.1 Hall effect

C is predicted to be a *p*-type dopant for ZnO. In order to determine carrier type and concentration of the ZnO:C thin films, the Hall measurement was conducted. Table 8 shows the resistivity, carrier concentration and Hall mobility of the ZnO:C thin films measured at room temperature. The ZnO:C thin films exhibit *p*-type conduction with the hole concentration at about $2 \times 10^{18}/\text{cm}^3$. The experimental result is in good agreement with the theoretical studies. [46, 49] Theoretical calculations suggested that direct hole doping at the anion site such as C substitution on the O site is more effective for localizing the hole and sustaining the magnetic moment.

It is noted that the resistivity increased with the increase of the C concentration in the ZnO:C thin films. It is generally known that shallow donors or acceptors increase the concentration of electrons or holes in the semiconductors, while

deep level impurities only reduce the concentration of carriers due to their bonding nature in the host crystal.

Table 8 The resistivity, carrier concentration and Hall mobility of the ZnO:C thin films measured at room temperature.

ZnO:C film	①	②	③	④
Resistivity ($\Omega\cdot\text{cm}$)	3.69	3.84	3.98	4.09
Carrier concentration ($\times 10^{18}/\text{cm}^3$)	1.92	1.94	2.00	2.08
Hall mobility ($\text{cm}^2/\text{V}\cdot\text{s}$)	4	20	25	28
Type of conduction	<i>p</i>	<i>p</i>	<i>p</i>	<i>p</i>

6.4.2 Temperature dependence of the resistivity

The temperature dependence resistivity $\rho(T)$ of the ZnO:C thin film (film ①) is plotted in Figure 6-6. The resistivity of the ZnO:C thin film decreases with increasing temperature. Three distinct $\rho(T)$ regions with their crossover temperatures at 216 K (T_1) and 300 K (T_2) are clearly depicting three different transport mechanisms. For $T > T_2$, the ZnO:C thin film exhibits the metallic-like behavior with its resistivity and activation energy keep almost constant at 3.7 $\Omega\cdot\text{cm}$ and 1.23 meV, respectively. The metallic behavior persists until T_2 and then followed by a sharp rise in the resistivity up to a temperature of about T_1 , which is reminiscent of a metallic-like to semiconductor-like transition. The ZnO:C possesses resistivity of 62 $\Omega\cdot\text{cm}$ at 216 K. For $T < T_1$, the resistivity increases monotonically. At 30 K, the resistivity of the ZnO:C increases to 70 $\Omega\cdot\text{cm}$ and having activation energy of 417 meV, elucidating an insulator-like

behavior. Interestingly, we note that the transition temperature of T_1 corresponds well to the ZFC-FC peak of ZnO:C (film ①) as illustrated in Figure 6-6 and Figure 6-4. It suggests that there should be a close correlation between the transport and magnetic properties of the ZnO:C.

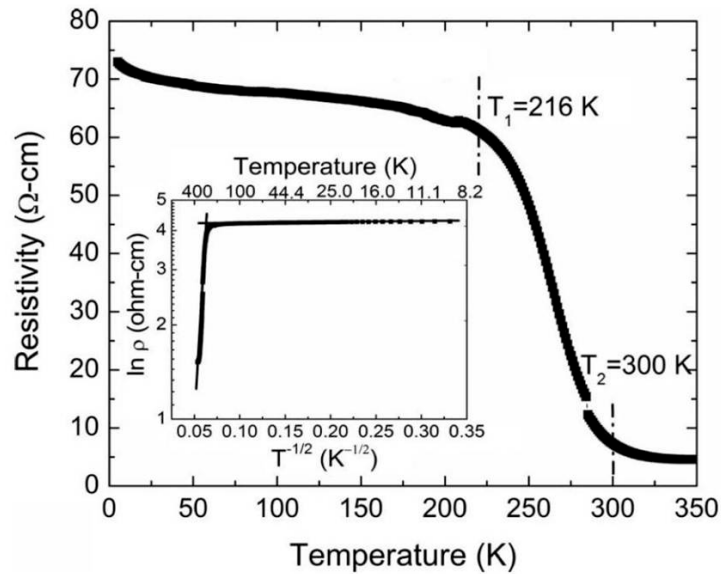


Figure 6-6 Temperature dependence of the resistivity on the ZnO:C thin film (film ①). The variable range hopping in the presence of carrier-carrier interaction is evident from the linearity of $\ln(\rho)$ vs. $T^{-1/2}$ as shown in the inset, where solid curves are a guide for the eye. The linear fit depicts a transport mechanism and activation energy change at 216 K for the sample.

In order to further explore the transport mechanism in the ZnO:C, the data were replotted into $\ln(\rho)$ versus $T^{-1/2}$ as shown in the inset of Figure 6-6. It is evident that $\ln(\rho)$ is linear as a function of $T^{-1/2}$ with a crossover point at T_1 . The linearity of $\ln(\rho)$ as a function of $T^{-1/2}$ for the entire temperature range is qualitatively consistent with the thermally activated process, $\rho = \rho_0 \exp[(T_0/T)^{1/2}]$, which is a characteristic of magnetic polaron variable range hopping (VRH) in the presence of carrier-carrier interaction.[130] The VRH mechanism provides a reasonable explanation of transport behavior in ZnO:C thin films.

6.4.3 Anomalous Hall resistivity

Figure 6-7 shows the magnetic field (H) dependence Hall resistivity (ρ_{xy}) for the ZnO:C thin film (film ①). The field was applied perpendicular to the sample's surface at 300 K as depicted in the inset of Figure 6-7.

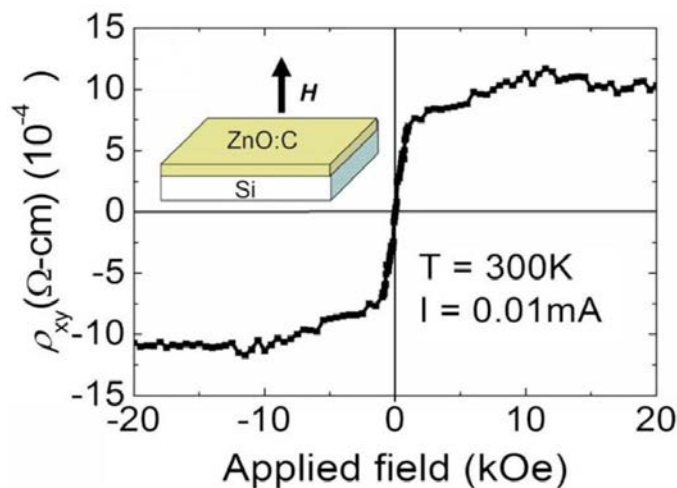


Figure 6-7 The magnetic field dependence of anomalous Hall resistivity ρ_{xy} on the ZnO:C thin film (film ①) measured at 300 K. The applied magnetic field is perpendicular to the sample plane with constant current of 0.01 mA as illustrated in the inset.

As it is common for the ferromagnetic materials, the value of ρ_{xy} is given by the sum of the ordinary Hall effect and anomalous Hall effect (AHE) term determined by the magnetization $M(H)$. [131] At low magnetic fields (< 2.5 kOe), ρ_{xy} has largely linear field dependence and the anomalous contribution dominates. Above 2.5 kOe, ρ_{xy} increases gradually and becomes much less field dependent, which is dominated by ordinary Hall resistance. The positive slope at high field regime implies the charge carriers in the ZnO:C thin film is p -type with its hole concentration at $2 \times 10^{18}/\text{cm}^3$. Theoretical calculations suggested that direct hole doping at the anion site such as C substitution on the O site is more effective for

localizing the hole and sustaining the magnetic moment.[46, 132] The result is in good agreement with the theoretical prediction. It is worthwhile to highlight that the characteristic of ρ_{xy} as a function of magnetic field is similar to the $M(H)$ plot as shown in Figure 6-2, suggesting intrinsic nature of ferromagnetism in the ZnO:C.

Next, we take into account the magnetotransport properties of the ZnO:C thin film before discussing the intrinsic nature of this ferromagnetic material. Figure 6-8 shows the temperature dependence of resistivity on the ZnO:C thin film, performed at applied magnetic fields of 0, 1, 4 and 8 Tesla. The resistivity decreases with an increase in magnetic field, reflecting negative magnetoresistance ratio. To our surprise, the remarkable change in resistivity occurred in the temperature range between 180 and 240 K, as seen from the inset of Figure 6-8. It is an unusual phenomenon as compared to ZnO:TM materials.[133]

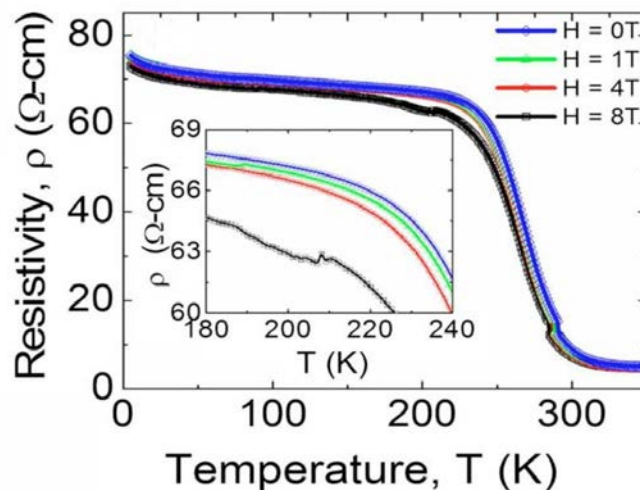


Figure 6-8 Temperature dependence resistivity of the ZnO:C thin film (film ①) under an applied field of 0, 1, 4 and 8 Tesla. Inset shows the temperature dependence resistivity from 180 to 240 K.

6.4.4 Magnetoresistance

Figure 6-9 shows the magnetoresistance (MR) ratio curves of the ZnO:C thin film (film ①) at 5, 200, and 300 K, the corresponding MR ratio is -1%, -4%, and -0.2%, respectively. The MR is peaked at 200 K and then the value decreases to about 0.2% at 300 K. This unusual result is in accordance with the magnetic dependence $\rho(T)$ data in Figure 6-8. Combining the magnetic and magnetotransport analysis, the possible underlying mechanism of this unusual MR effect should correlate to the magnetic inhomogeneous and magnetic phase transition at 200 K, as evidenced by $M(T)$ curves in Figure 6-4. Near transition temperature of 200 K, the ground state changes from ferromagnetic to antiferromagnetic state, leading to domain wall scattering. Domain walls are known to be a source of resistance and the phase transition energy goes along with domain walls.[134] Thus, the strongest MR near 200 K could be due to its smaller antiferromagnetic-ferromagnetic transition energy and reduced domain walls resistance. The rapid rise in resistivity from 300 to 200 K could be attributed to the gradual growth of antiferromagnetic interaction, as suggested by the ZFC-FC curve given in Figure 6-4. Interestingly, the similar MR behavior is found in hole-doped perovskite manganites system such as $\text{La}_{1-x}\text{Sr}_x\text{MnO}_3$, where the highest negative MR ratio occurred at the ferromagnetic transition temperature.[135]

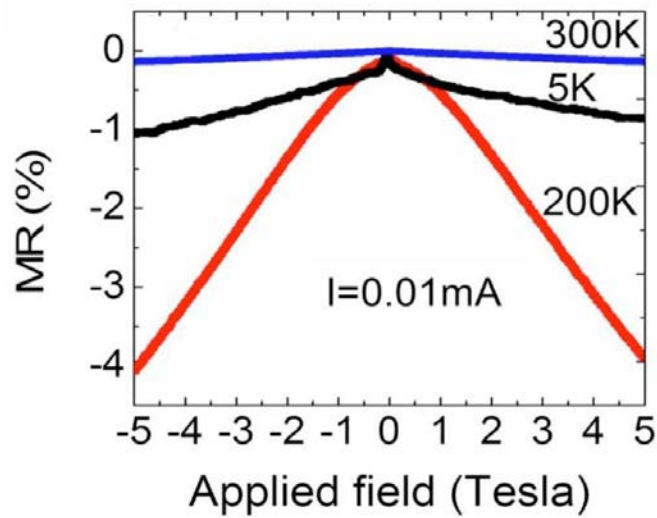


Figure 6-9 The MR curves of the ZnO:C thin film (film ①) measured at 5, 200, and 300 K.

6.5 Stability of ferromagnetism

It is known that ferromagnetism in ZnO:TM films or nanoparticles are not stable and will degrade with time. The degradation could take place within hour to several months after the samples were synthesized.[136-139] Thus, it would be of interest to study the stability of the ZnO:C samples. The ZnO:C thin film (film ①) was kept in a transparent sample box in ambient air for a long period of time. The time dependence M_s was measured in an interval of three months as plotted in Figure 6-10. M_s of the ZnO:C thin film remains constant at 3.9 emu/cm^3 over a period of one year. Our observation is stark contrast to many ZnO:TM materials where the ferromagnetism will degrade with time.[137-139] It should also be noted that the hole concentration of the ZnO:C thin films remains almost constant for the entire storage period as shown in Figure 6-10, suggesting the stable p -type behavior in the ZnO:C system. The transient p -type behavior observed in most of the p -type ZnO can be attributed to either the addition of free

electrons due to hydrogen or the creation of compensating defects.[137] The conduction in ZnO:C thin films does not seem to be sensitive to ambient air or oxidation process.

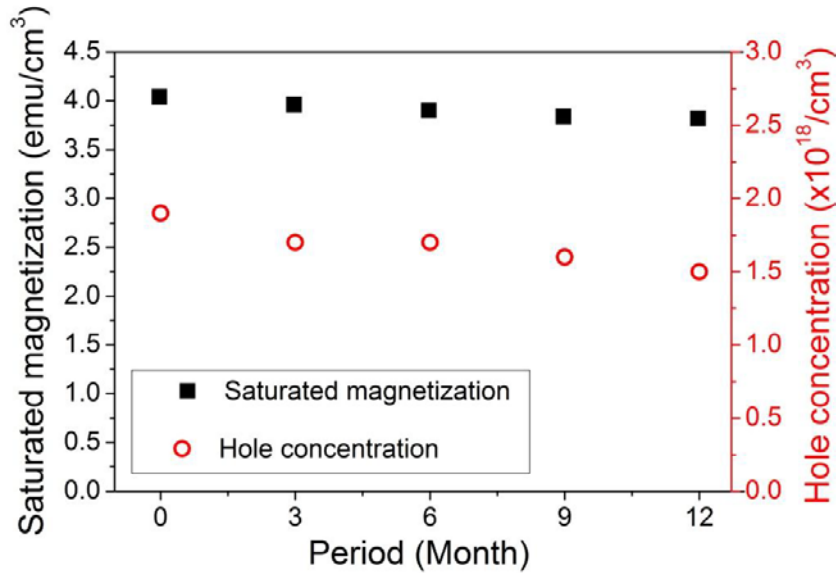


Figure 6-10 M_s and hole concentration of the ZnO:C thin film (film ①) as a function of the storage time.

To have better understanding of its ferromagnetic stability, the ZnO:C thin film (film ①) was annealed in air for 15 minutes at various temperatures ranging from room temperature to 700 °C. M_s of the ZnO:C thin film remains constant for annealing temperature up to 200 °C as shown in the Figure 6-11. Nevertheless, M_s reduces by 17.5% to 3.3 emu/cm³ after the sample was annealed at 300 °C. The sample annealed at 300 °C shows high resistivity and no reliable Hall effect could be obtained. The loss of electronically active acceptor states could be explained by the generation of compensating defects such as oxygen vacancies.[137] The ferromagnetism in the ZnO:C thin film is associated

with the hole and the hole could enhance the ferromagnetism, which is in good agreement with the theoretical studies.[46, 49]

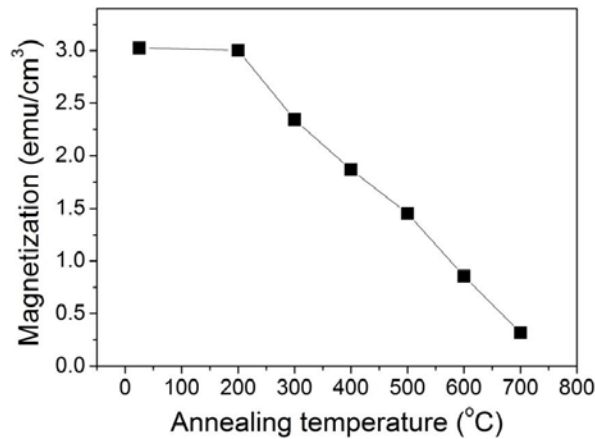


Figure 6-11 M_s dependence of the ZnO:C thin film (film ①) as a function of annealing temperature.

6.6 Summary

The ZnO:C thin films with different carbon concentrations showed hexagonal wurtzite structure. All the ZnO:C thin films exhibit ferromagnetic ordering at room temperature and the Curie temperature is above 330 K. *P*-type conduction is observed in the ZnO:C thin films with their hole concentrations about $2 \times 10^{18}/\text{cm}^3$. The ZnO:C thin film exhibits the semiconductor behavior when the temperature is between 30 K and 216 K. For the temperature is above 300 K, the ZnO:C thin film shows the metallic-like behavior. When temperature is lower than 30 K, the resistivity of the ZnO:C thin film increases significantly, elucidating an insulator-like behavior. The AHE and MR signals at room temperature reveal that direct hole doping at the anion site in the ZnO:C thin films is more effective for localizing the hole and sustaining the magnetic

moment. The ZnO:C thin films are stable at room temperature and do not degrade markedly during the storage time of more than one year.

CHAPTER 7

Ferromagnetic ZnO:C nanoneedles

7.1 Introduction

Owing to the peculiar characteristics and the particular application, one-dimensional (1D) ZnO-based DMS nanostructures has attracted great attention in materials science and nanotechnology fields. It is due to the high processing temperature in the conventional methods such as pulsed laser deposition and solid state reaction that the fabrication of 1D ZnO:C nanoneedles remains largely unexplored. One way to overcome this problem is the use of ion beam doping at low temperatures. Ion beam irradiation to the metals, semiconductors, and also carbon surfaces can induces the formation of various types of surface structures, such as ripples, conical protrusions, rods, and whiskers, with dimensions from nano- to micrometers.[117, 140, 141] This technique has been proved as an effective method for doping and the fabrication of nanoneedles at room temperature.[120, 142, 143] Cu-doped ZnO nanoneedles were fabricated by this technique showing room temperature ferromagnetism [119]. In this chapter, we report the magnetic anisotropy in the ferromagnetic ZnO:C nanoneedles fabricated by the ion beam irradiation technique at room temperature. Similar to the ZnO:C thin films, the nanoneedles are labeled as needles ①, ②, ③ and ④

with increasing C content according to their number where needles ① and ④ being the lowest and highest C content respectively.

7.2 Structural characteristics

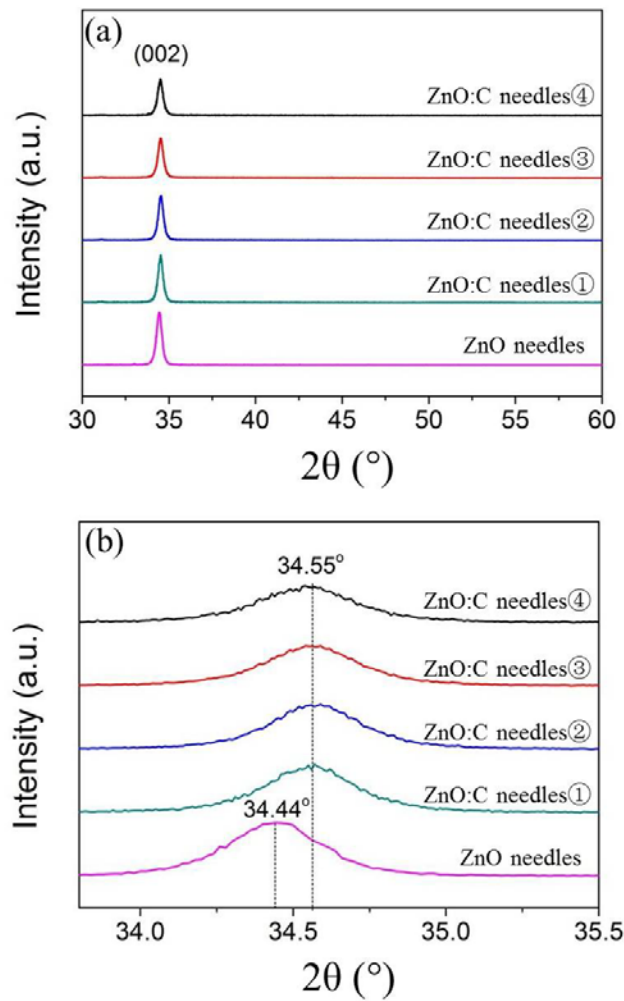


Figure 7-1 (a) XRD patterns of the ZnO nanoneedles and ZnO:C nanoneedles with different carbon concentrations and (b) the expanded view of XRD patterns.

Figure 7-1 shows the XRD patterns of the ZnO and ZnO:C nanoneedles. The (002) peaks associated with the hexagonal wurtzite structure are observed at

34.44° and 34.55° in the ZnO and ZnO:C nanoneedles, respectively. No graphite-related peak is detected within the sensitivity of XRD. The (002) peak of the ZnO:C nanoneedles is shifted to a higher angle comparing with the undoped ZnO nanoneedles. By the calculations through Equation (1) Bragg law and Equation (2) formula of lattice constants mentioned in Chapter 6, the lattice constant c of (002) plane can be calculated. It reveals that the c of the ZnO:C nanoneedles is reduced by 0.337% as compared to the ZnO nanoneedles. The radius of Zn^{2+} , O^{2-} and covalent carbon are 0.74Å, 1.40Å and 0.77Å respectively. The radius of covalent carbon is smaller than the radius of O^{2-} . The reduction of lattice constant c with carbon doping is expected as smaller C ions substituted into the O sites of ZnO lattices.

7.3 Field emission scanning electron microscopy

The surface morphology of the nanoneedles is shown in Figure 7-2 obtained by field emission scanning electron microscope (FESEM). It is disclosed that the surface of the sample is covered with needle-like structures. The ZnO:C nanoneedles are uniformly distributed. Figure 7-2(b) was taken by aligning the sample faces to the electron beam with a tilt angle so that the inclined angle between the nanoneedles and substrate could be estimated. The needle-like structures with the sharp tips are aligned at an angle of around 45° relative to the surface of the ZnO film. The length of the nanoneedles is about 700 nm and the average diameter of the shaft is 200-250 nm with considerably sharp morphology. The apex angle of the nanoneedles is around 15°.

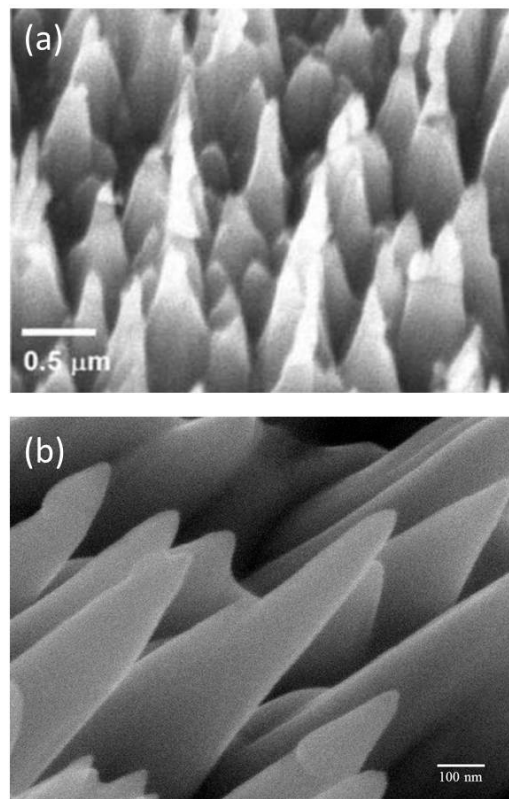


Figure 7-2 FESEM images of the ZnO:C nanoneedles: (a) sample surface is perpendicular to the electron beam; (b) sample surface faces to the electron beam with a tilt angle of 45°.

7.4 Magnetic properties

7.4.1 M-H loops

Ferromagnetic properties of the ZnO:C nanoneedles were investigated. The measured magnetization has subtracted the diamagnetic background arising from the substrate. The undoped ZnO nanoneedles are non-magnetic. The ZnO:C nanoneedles exhibit ferromagnetism at room temperature with clear hysteresis loops as shown in Figure 7-3. The saturated magnetizations of the ZnO:C nanoneedles increase with the increasing of the carbon concentration.

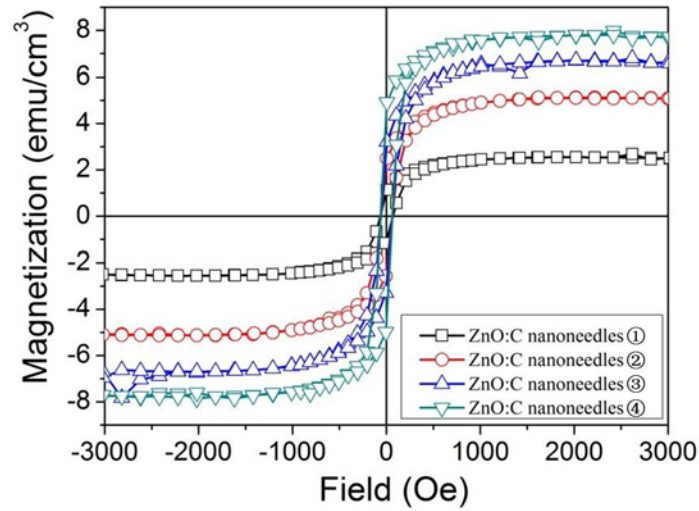


Figure 7-3 The magnetization hysteresis loops of the ZnO:C nanoneedles with different carbon concentration at room temperature.

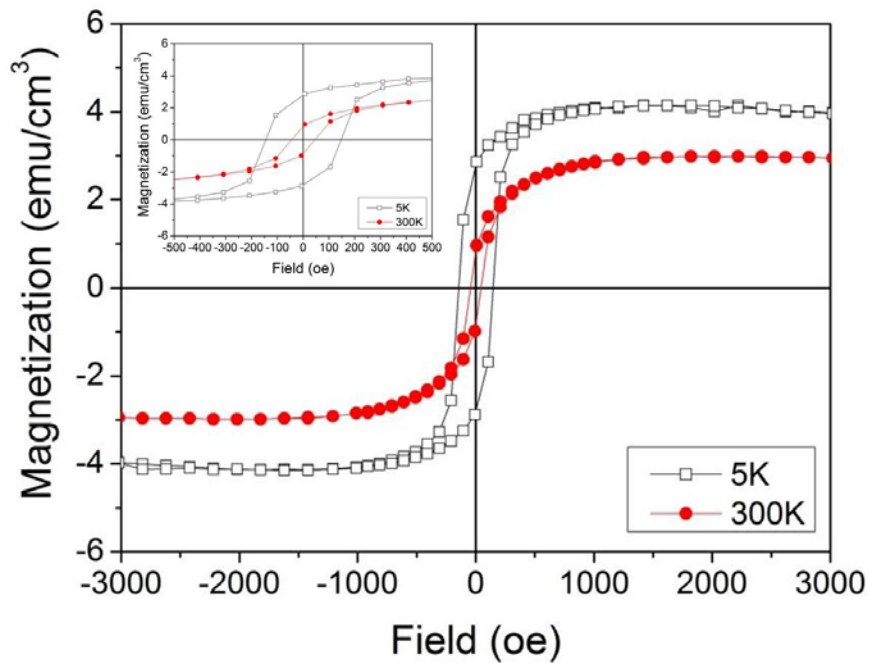


Figure 7-4 Magnetic hysteresis loops of the ZnO:C nanoneedles (needles ①) at 5 and 300 K. The inset shows enlarged view of the magnetic hysteresis loops.

Figure 7-4 depicts the magnetic hysteresis loops of the ZnO:C nanoneedles (needles ①) at 5 and 300 K. The sample shows the clear hysteresis loop at room

temperature with its M_s of 3.04 emu/cm^3 . At 5 K, a mild increment of M_s by 27% is observed. Nevertheless, a large enhancement in H_C is detected at low temperature. H_C is found in the order of 60 Oe at 300 K; then it is surged to 150 Oe at 5 K, as illustrated in the inset of Figure 7-4. This broadening effect is a classical behavior of magnetic materials at low temperature.

7.4.2 ZFC-FC magnetization curves

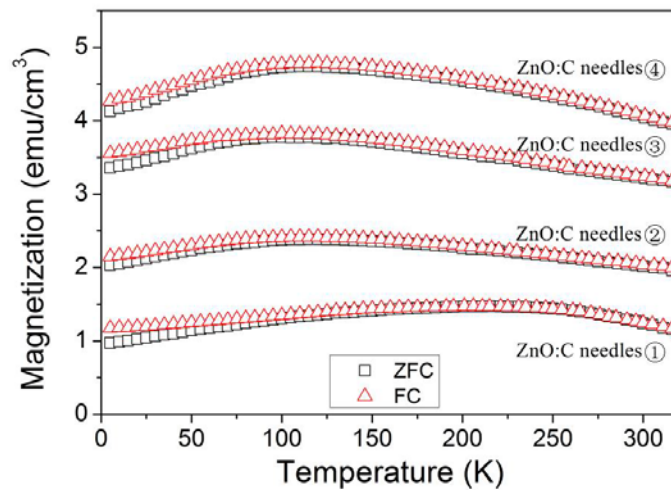


Figure 7-5 ZFC-FC magnetization curves for ZnO:C nanoneedles with different carbon concentrations measured at low magnetic field of 50 Oe.

Figure 7-5 shows the ZFC-FC magnetization curves of the ZnO:C nanoneedles measured at low magnetic field of 50 Oe. The Curie temperature of the sample is above 330 K. The ZnO:C nanoneedles show the ferromagnetic behavior at room temperature and spin-glass behavior at low temperature. ZFC and FC magnetization increases slowly to a plateau as the temperature increases from 5K. The slightly convex shape of the ZFC-FC magnetization curves reflects the antiferromagnetic and ferromagnetic transition at transition temperature (T_T)

about 120 K.[144] When $T > T_T$, the magnetization increases with decreasing the temperature which is a characteristic feature of the ferromagnetic DMS. For $T < T_T$, a pronounced antiferromagnetic interaction is observed. However, the ferromagnetic phase is still dominant over the whole temperature range.

7.4.3 Ferromagnetic anisotropy

In order to investigate the ferromagnetic anisotropy of the ZnO:C nanoneedles, the magnetizations of the ZnO:C nanoneedles (needles ①) were measured at different directions of the applied fields, as shown in Figure 7-6. M_s is 3.04 emu/cm^3 and 1.24 emu/cm^3 when the applied field was parallel and perpendicular to the surface of samples, respectively. The sample exhibits the ferromagnetic anisotropy at high field ($> 200 \text{ Oe}$). As proposed by Sati *et al.*, the easy plane ferromagnetism in ZnO:C may be considered as a signature of intrinsic ferromagnetism where carbon ions in ZnO possess a strong single anisotropy.[145] Chanier *et al.* reported the tetrahedral and trigonal crystal field of ZnO, together with spin-orbit coupling, lead to a magnetic anisotropy.[146]

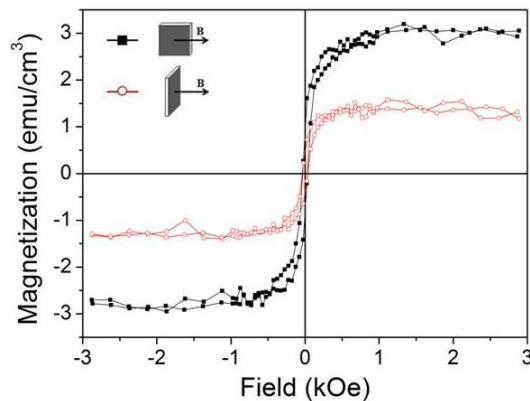


Figure 7-6 The magnetization hysteresis loops of the ZnO:C nanoneedles (needles ①) at room temperature in the perpendicular and parallel directions of the applied fields.

In order to determine the origin of the ferromagnetic anisotropy of the ZnO:C nanoneedles, the samples were tilted by 45° relative to the plane of the sample surface to align the angle (θ) between the shape axis of the nanoneedles and the applied field (B) equal to zero degree. Figure 7-7 shows the angular dependence of M_s and H_c of the ZnO:C nanoneedles from $\theta = 0^\circ$ to $\theta = 180^\circ$. When $\theta = 0^\circ$, M_s and H_c reach the minimum and maximum respectively. With the increasing of θ from 0 to 90° , M_s increases and H_c decreases. It confirms that the ferromagnetic anisotropy in the ZnO:C nanoneedles. The easy axis of the ZnO:C nanoneedles is perpendicular to the shape axis of the nanoneedles. There are two different effects related to the observed anisotropy. First, the easy axis of the single ZnO:C nanoneedle is perpendicular to the shape axis of the sample. It is easier to saturate the sample with a low field (about 1000 Oe, see Figure 7-6) applied in the perpendicular direction to the shape axis. Second, the effect related to the anisotropy of the sample as the magnetization along the direction of $\theta = 0^\circ$ is the smallest at all fields.

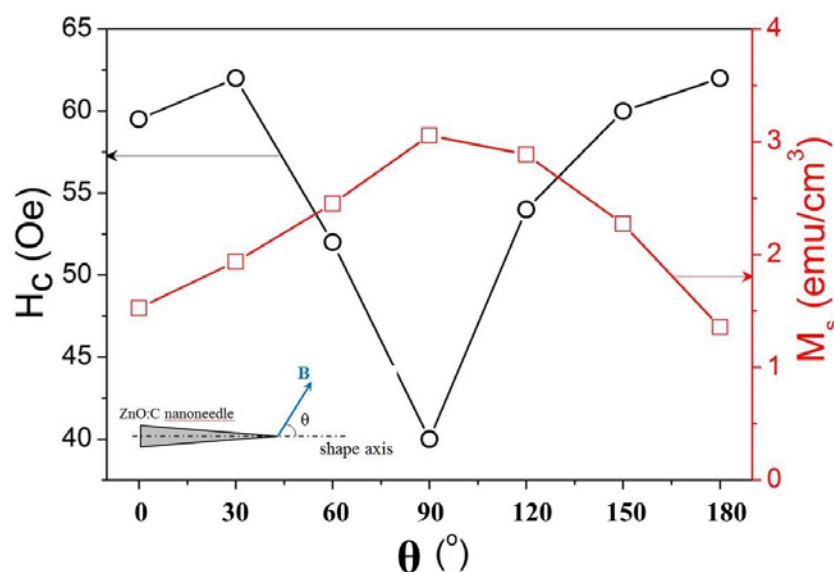


Figure 7-7 Angular dependence of M_s and H_c for the ZnO:C nanoneedles (needles ①).

The dipole–dipole interaction model has been employed to explain qualitatively the magnetization behaviors in magnetic wire arrays with the length from nanometers to microns [147-150]. The model can also be applied to our samples. The ZnO:C nanoneedles can be considered as a two dimensional array of magnetic dipoles. There are two key contributions in the determination of the field acting on the single nanoneedle. Firstly, the intrinsic self-demagnetization field ($H_{//}$) which leads to a magnetic easy axis parallel to the nanoneedle’s shape axis. Secondly, the extrinsic dipole field (H_{\perp}) prompts by the magnetostatic coupling among the nanoneedles which induced a magnetic easy axis perpendicular to the nanoneedle’s shape axis. The total effective anisotropic field (H_k) acting on one nanoneedle can be written as

$$H_k = H_{//} - H_{\perp} = 2\pi M_s - \frac{6.3\pi M_s r^2 L}{D^3}$$

in where r , L , and D represent the diameter, length, and separation of the nanoneedles respectively. When H_k equals to zero, the critical length L_c equals to $\frac{2D^3}{6.3r^2}$. If the length of the nanoneedle is larger than L_c , H_k is negative. Thus, the magnetic easy axis is perpendicular to the nanoneedle’s shape axis due to the dominant of the dipole field (H_{\perp}). For our nanoneedles, $D = 300$ nm and $r = 250$ nm, we have $L_c = 137$ nm. The average length of our ZnO:C nanoneedles (L) is about 700 nm which is larger than L_c . It reveals that H_k is dominated by H_{\perp} which is in good agreement with the experimental result. Therefore, the easy axis is perpendicular to the shape axis of the nanoneedles so that M_s reaches maximum when $\theta = 90^\circ$. H_c represents the sum of the intrinsic field ($H_{//}$) and extrinsic field (H_{\perp}) of the nanoneedles. It is evident that H_{\perp} increases with M_s as

M_s increases with θ and reaches maximum at $\theta = 90^\circ$. As shown in Figure 7-7, H_c decreases as θ increases from 0° to 90° . It suggests that $H_{//}$ should be decreased as θ increases from 0° to 90° in order to compensate the effect of H_{\perp} . It indicates that $H_{//}$ is more sensitive than H_{\perp} to the applied field although H_{\perp} is the dominated field in ZnO:C nanoneedles. As the result, the observed ferromagnetic anisotropy in the ZnO:C nanoneedles arrays reveals that every individual ZnO:C nanoneedle possesses ferromagnetism. As to the ZnO:C nanoneedles array assembled on the substrate, dipole–dipole interaction amongst nanoneedles which generate the H_{\perp} makes the easy axis of sample perpendicular to the shape axis of nanoneedles.

7.5 Transport properties

Anomalous Hall effect (AHE) is an important tool for identifying intrinsic ferromagnetic semiconductor. The Hall resistivity (ρ_{xy}) is given by sum of the ordinary Hall effect and AHE term, $\rho_{xy} = R_0B + R_s\mu_0M$, where R_0 , B , R_s , μ_0 and M is ordinary Hall coefficient, magnetic induction, anomalous Hall coefficient, magnetic permeability and magnetization, respectively. Figure 7-8 shows the magnetic field (H) dependence Hall resistivity (ρ_{xy}) of the ZnO:C nanoneedles (needles ①). The field was applied perpendicular to the sample's surface at room temperature. At low magnetic fields (< 1 kOe), ρ_{xy} has largely linear field dependence and the anomalous contribution dominates. Above 1 kOe, ρ_{xy} increases gradually and becomes much less field dependent, which is dominated by ordinary Hall resistance. The positive slope at high field regime

implies the charge carriers in the ZnO:C nanoneedles is *p*-type with its hole concentration of $1.9 \times 10^{18}/\text{cm}^3$. It should be noted that *n*-type conduction was observed in the undoped ZnO films. Thus, the observed *p*-type conduction in the ZnO:C nanoneedles must be associated with the carbon doping.

In addition, by subtracting the linear normal Hall effect term yields a clear signature that corresponding to the AHE as shown in the inset of Figure 7-8. Notably, the shape of the ρ_{xy} curve is well coincidence with the room temperature M-H curve as shown in Figure 7-8, confirming intrinsic ferromagnetism in the ZnO:C nanoneedles.

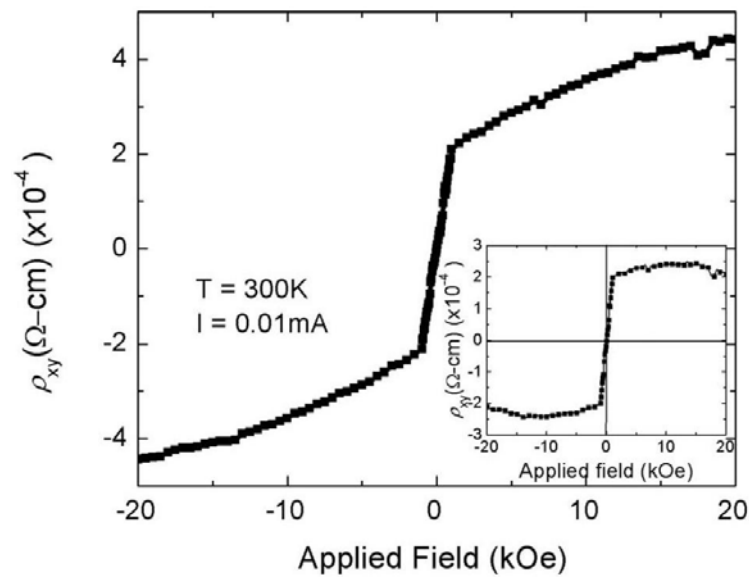


Figure 7-8 The magnetic field dependence of anomalous Hall resistivity (ρ_{xy}) of the ZnO:C nanoneedles (needles ①) measured at 300 K. The applied magnetic field is perpendicular to the sample's plane with constant current of 0.01 mA. The ρ_{xy} data after background subtraction is displayed in the inset.

7.6 Summary

The ZnO:C nanoneedles exhibit ferromagnetism at room temperature with the saturated magnetization up to $7.9 \text{ emu}/\text{cm}^3$, and *p*-type conduction with hole

concentration of $1.9 \times 10^{18}/\text{cm}^3$. The AHE curves are quantitatively consistent with the M-H loops, indicating the existence of spin-polarized carriers. The ferromagnetic anisotropy with an easy axis perpendicular to the shape axis of the ZnO:C nanoneedles is observed due to the dipole–dipole magnetic interaction amongst nanoneedles.

CHAPTER 8

Origin of ferromagnetism

8.1 Introduction

This chapter is devoted to study the origin of ferromagnetism in the ZnO:C system. The detailed microstructure and elemental analysis of the ZnO:C system were investigated using HRTEM, TEM, EELS, EDX and XANES in order to explore the mechanism of the ferromagnetism in the ZnO:C system.

8.2 High resolution transmission electron microscopy

High resolution transmission electron microscopy (HRTEM) images of the ZnO:C and ZnO thin films are shown in Figure 8-1(a)~(d). The selected area diffraction pattern (SADP) of the ZnO:C with the simulated SADP ring pattern of ZnO are shown in Figure 8-1(e). The SADP of the film is matched with the simulated ZnO pattern, implying the film exhibited ZnO wurtzite structure. No precipitates or nanocluster was observed in the film. HRTEM images show that the ZnO:C thin film has a large amount of complicated defects such as platelike defects and stacking faults. Figure 8-1(b) and (c) reveal the multiple stacking faults and platelike defects in ZnO:C sample respectively. These dislocations are probably caused by the lattice distortion induced by carbon doping and the non-epitaxy with the SiO₂/Si substrate.

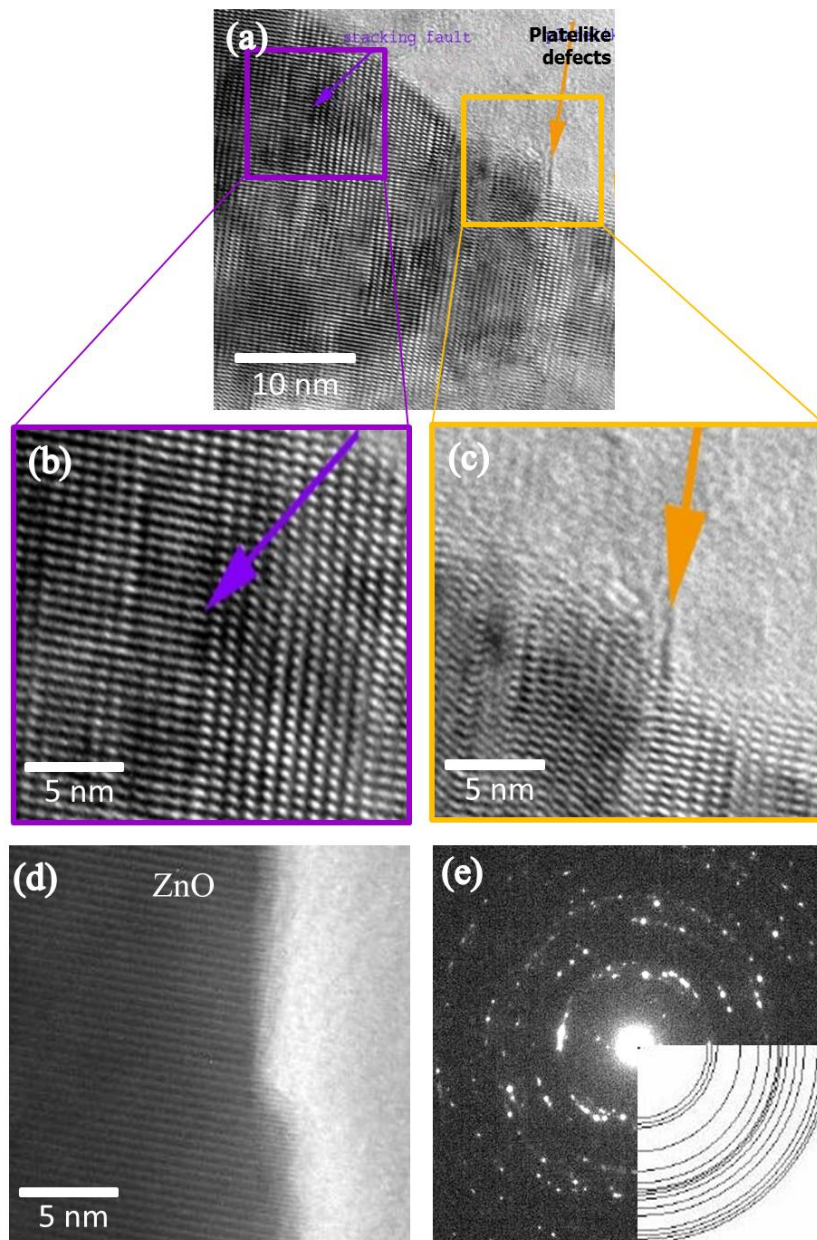


Figure 8-1 (a)~(c) HRTEM images of the ZnO:C thin film. The stacking fault (purple arrow) and platelike defects (yellow arrow) are marked in the images (b) and (c), respectively. (d) HRTEM image of the as-grown ZnO. (e) The comparison image of the SADP of ZnO:C with the simulated patterns of ZnO.

8.3 Transmission electron microscopy

Figure 8-2 shows the cross-sectional transmission electron microscopy (TEM) images of the ZnO:C thin films (film ①, ② and ④). TEM images show that the

nano-crystallined ZnO:C thin films have the columnar growth characters. The grain size of film ① is about 25 nm. As the C concentration increases, the grain size of film ② and ④ reduces to 20 nm and 10 nm, respectively.

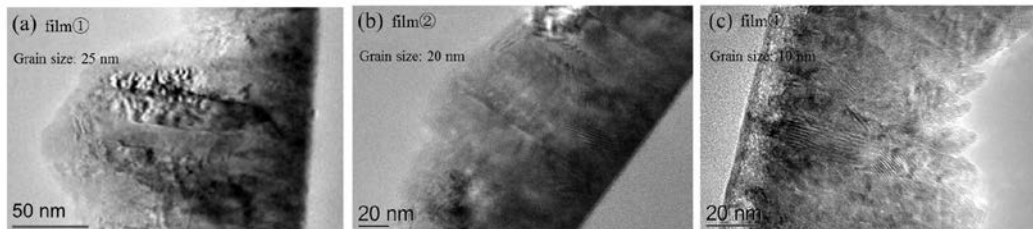


Figure 8-2 TEM images of ZnO:C thin films (a) film ①, (b) film ② and (c) film ④.

The decreasing of the grain size of the ZnO:C film can be ascribed to the increase of the defects which were introduced by the carbon doping. As discussed above, carbon doping introduces stacking faults and platelike defects in the ZnO:C sample. It seems that these defects are relevant to the ferromagnetism in the ZnO:C samples.[151-154] In order to investigate the effect of the defects on the ferromagnetism in ZnO samples, undoped ZnO samples were prepared by the ion beam irradiation under the same conditions as the fabrication of ZnO:C samples but no carbon source. No ferromagnetism was observed in the samples, as shown in Figure 8-3. Therefore, the possibility of ferromagnetism in the ZnO:C samples originated from the structural defects could be excluded.

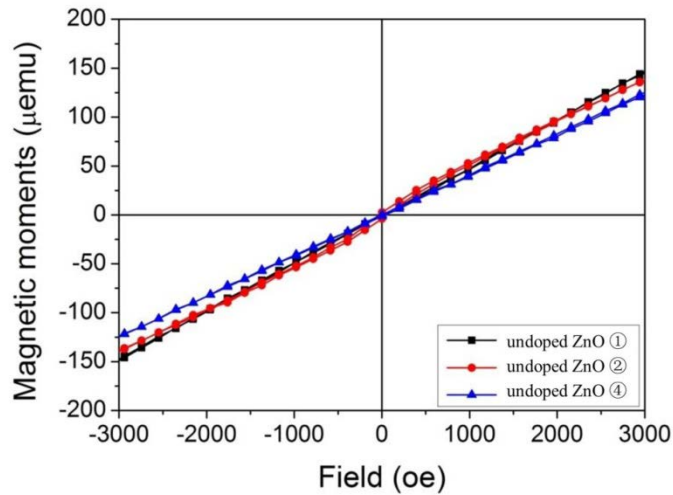


Figure 8-3 The magnetization hysteresis loops of the undoped ZnO samples irradiated by ion beam.

8.4 Electron energy loss spectroscopy

The typical EELS spectra of the ZnO:C thin films are shown in Figure 8-4. The spectra exhibit Si, Zn and O core loss spectra but no C K-edge are recorded. It suggests that either the C concentration is not high enough to be detected by EELS, or C elements are solute in the ZnO matrix. The C elements could be localized inhomogeneous distributed in the ZnO matrix. A high resolution scanning transmission electron microscope images with corresponding nanoprobe line scanning electron energy loss are needed to see if there is any correlation between C and local defects in the samples.

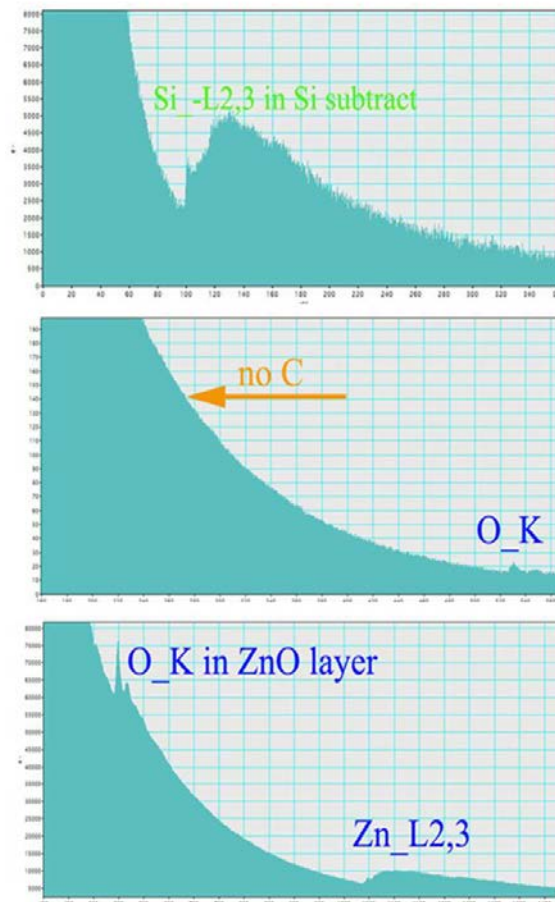


Figure 8-4 The typical EELS spectra of the ZnO:C thin films.

In addition, the elemental homogeneity of the ZnO:C film was further examined by EDX mapping, as shown in Figure 8-5. The image from the top left of Figure 8-5 is a regular TEM image. The others represent EDX mapping of Zn, C, and O elements, respectively. The arbitrary color scale is proportional to the element's concentration. On this particular sample, the recorded images indicate a homogeneous distribution of C element. No other elements are detected. Thus, the magnetic properties of the ZnO:C are not caused by other magnetic phases, but rather due to the C doping. The C K-edge energy dispersion is almost similar to O K-edge energy dispersion so that the C energy peak may be influenced by

the high intensity O energy peak. It may be the reason why there is no distinct C peak found in the EELS spectrum.

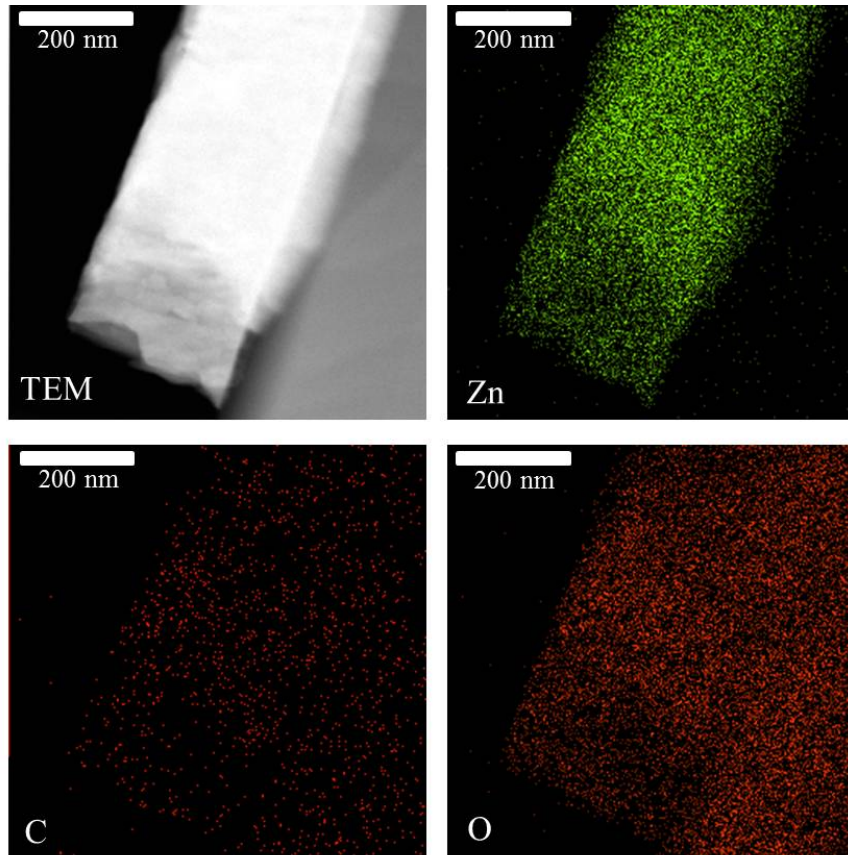


Figure 8-5 EDX mapping of the ZnO:C thin film. On the top left is a TEM image of the same area.

8.5 X-ray absorption near-edge fine structure spectroscopy

The detailed electronic structure of the ZnO:C thin films was investigated by X-ray absorption near-edge fine structure spectroscopy (XANES) at oxygen (O) and carbon (C) K-edges. Figure 8-6 shows the normalized XANES spectra at O K-edge of the ZnO:C thin films (film ①, ② and ④). Based on existing literatures and band structure calculations [155], the spectral features are assigned as follows: (a) the energy region between 527 and 532 eV is attributed mainly to O

$2p$ hybridization with highly dispersive Zn $3d4s$ / C $2s2p$ states which form the bottom of the conduction band with a peak at 529 eV due to transition to non-dispersive O $2p$ states and (b) the region between 533 and 550 eV is assigned to O $2p$ hybridized with Zn $4p$ states and above 550 eV, the spectra arise due to the O $2p$ states that extend to Zn higher orbitals. As evident from Figure 8-6, the preedge peak at 529 eV evolves with the carbon doping in ZnO was marked by an arrow in Figure 8-6 and its intensity increases with the carbon concentrations, suggesting a strong hybridization of O $2p$ orbitals with C $2p$ states. This preedge feature provides the significant information about nature of charge carriers and their relevance. Similar preedge features have been reported in the oxides mainly in manganites [155-157]. Since this feature originates with the carbon doping, it is ascribed to dipole transitions from O $1s$ to O $2p$ states that are hybridized with the unoccupied states of C $2p$. Thus, the intensity of this peak represents the C $2p$ density of states. A continuous increase of this peak with the carbon doping indicates more unoccupied states at the C $2p$ levels and hence reflects the presence of more charge carriers, electrons or holes. Considering the energy of the peak's position, Asokan *et al.* [156, 158-160] associated this as a characteristic feature of whole doped system. Present work gives an opportunity to see the evolution of spectral features at different concentrations. The spectral intensity of the peak at 537 eV decreases and a shoulder like feature at its low energy region increases with the carbon doping. The spectral features above 550 eV are quite similar and nearly independent of the carbon concentrations, and are dominated by the contribution from multiple scattering effects. This suggests that C ions are incorporated in the system and responsible for changing the electronic

structure.

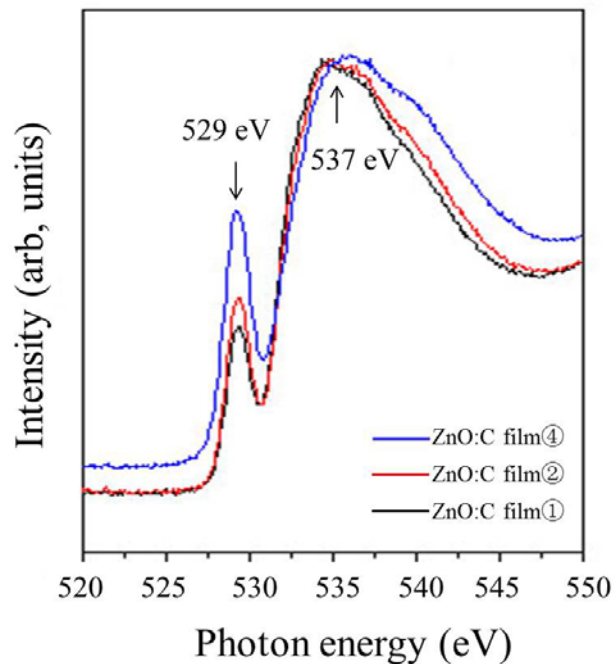


Figure 8-6 The normalized XANES spectra at O *K*-edge of the ZnO:C thin films (film ①, ② and ④).

The normalized XANES spectra at C *K*-edge are shown in Figure 8-7. The major spectral features are marked in the Figure 8-7. For X-ray energies in the XANES region, the excited photoelectron undergoes a transition from a core level to an unoccupied final state which is determined by the dipole-transition selection rule. The C *K*-edge XANES results indicate that the density of states (DOS) of both the unoccupied π^* and σ^* bands. The spectra of the ZnO:C thin films clearly display sharp features closely resembling those reported in earlier works.[161, 162] The two prominent peaks near 286.3 and 293.3 eV are known to be associated with the unoccupied π^* and σ^* bands respectively.[163, 164] Each C atom in the lattice possesses six electrons and has two *1s* electrons, three sp^2 electrons and one *2p* electron. The three sp^2 electrons form the three bonds in the

plane, leaving an unsaturated π orbital. It reveals that the intensity of the π^* band feature of the ZnO:C increases with the increase of the carbon concentration, which shows that the densities of unoccupied C π^* band states increase with the increase of the C concentration because the intensity is approximately proportional to the density of unoccupied states. The results of XANES spectra of the ZnO:C thin films at O K -edge and C K -edge indicate that the C substituted O induces the magnetic moments in the ZnO:C system. It is speculated that the substitution of C ions into O sites related to the origin of the ferromagnetism in ZnO:C system.

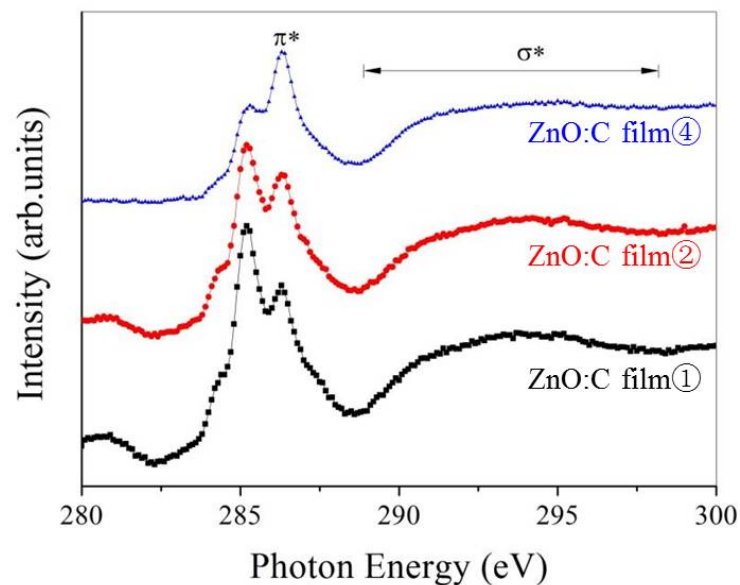


Figure 8-7 The normalized XANES spectra at C K -edge of ZnO:C thin films (film ①, ② and ④).

8.6 Origin of the ferromagnetism in ZnO:C

Since ZnO and carbon are non-ferromagnetic materials, the observed room-temperature ferromagnetism should be the intrinsic property of C-doped ZnO thin films. Carrier-mediated double exchange theory is often used to explain the

ferromagnetism in ZnO-based DMSs. Based on our experimental results and the band structures (see Figure 8-8) calculated by Pan *et al.*,[46] we propose the mechanism of ferromagnetic coupling in ZnO:C thin films is due to hole mediation.

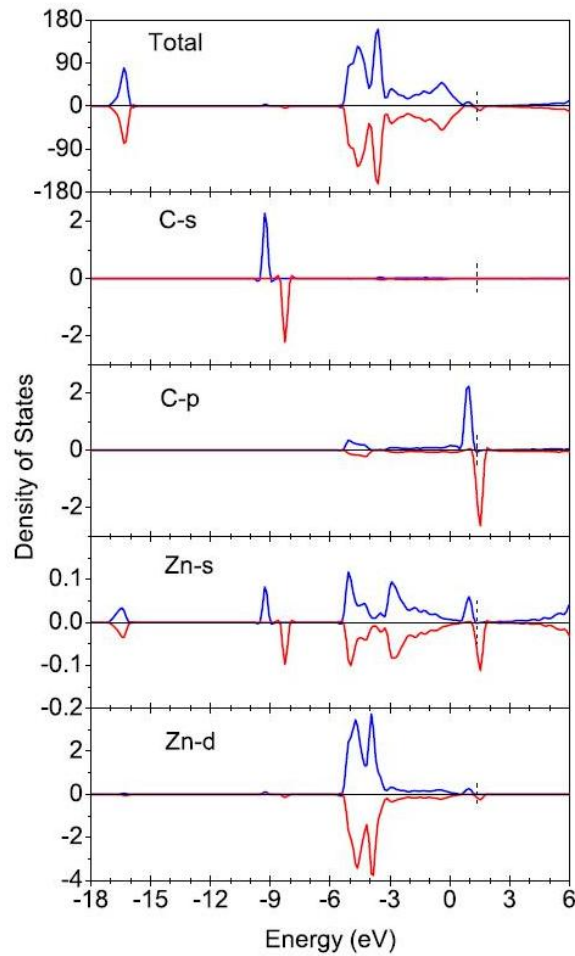


Figure 8-8 Calculated total (top panel) and local density of states for the carbon dopant and a neighboring Zn atom. The Fermi level is indicated by the dashed vertical line. [46]

The substitution of C atoms at O sites in the ZnO lattices introduces the holes in O $2p$ states, which hybridize with the unoccupied states of C $2p$ localized spins by a p - p interaction. This p - p interaction leads to the appearance of additional mixed band levels derived from the semiconductor valence band. The coupling

impels the minority p - p mixed state upward and the opposite spin state downward, resulting in the lowering total energy of the system. The wave function of the C $2p$ states is spatially extended to neighboring O $2p$ states, and couple to the O $2p$ states. By this p - p interaction, holes mediate the spin alignment of parent C atoms, leading to an indirect ferromagnetic coupling of C atoms. Our results of Hall effect and anomalous Hall effect indicate that the majority carrier in the ZnO:C thin films is hole, due possibly to the existence of free carbon and other types of defects such as oxygen vacancy, which can mediate the spin alignment at finite temperature. This hole doping enhances ferromagnetism remarkably. All of these confirm that C substitute O site could be the origin of the ferromagnetism and the hole-mediation is the mechanism of the ferromagnetism in ZnO:C thin films.

8.7 Summary

The microstructure and element analysis of the ZnO:C were investigated. The doping of carbon ions leads some defects in the samples such as platelike defects and stacking faults. These defects are not the origin of the ferromagnetism of ZnO:C samples. Carbon ions substituted oxygen sites in the lattice of ZnO can introduce holes in O $2p$ states hybridizing with C $2p$ states by a p - p interaction. By this p - p interaction, holes mediate the spin alignment of parent C atoms, leading to an indirect ferromagnetic coupling of C atoms. This may be the origin of the intrinsic ferromagnetism in ZnO:C system.

CHAPTER 9

Conclusions and recommendations

9.1 Conclusions

The room temperature ferromagnetism in the ZnO:C thin films as well as nanoneedles have been prepared by the filtered cathodic vacuum arc (FCVA) and ion beam irradiation (IBI) techniques. The ZnO:C system was optimized in terms of their magnetic properties.

The ZnO:C thin films exhibit the hexagonal wurtzite structure with high crystallinity and no impurity in the ZnO:C thin films. The magnetic domains randomly distributed in the ZnO:C thin film as the speckle structures. *P*-type conduction is observed in the ZnO:C thin films with their hole concentration about $2 \times 10^{18}/\text{cm}^3$ at room temperature. The ZnO:C thin films show the magnetoresistance effect with 4% MR ratio at 200 K. The anomalous Hall effect which is the ferromagnetic response of charge carriers in ferromagnetic semiconductor is observed in the ZnO:C thin films.

The one dimensional ferromagnetic ZnO:C nanoneedles showed high crystallinity. The ZnO:C nanoneedles exhibited the ferromagnetism at room temperature with the saturated magnetization up to $7.9 \text{ emu}/\text{cm}^3$, and AHE with hole concentration of $1.9 \times 10^{18}/\text{cm}^3$. The ferromagnetic anisotropy with an easy axis perpendicular to the shape axis of the ZnO:C nanoneedles was observed due

to the dipole–dipole magnetic interaction amongst nanoneedles.

The origin of the ferromagnetism in ZnO:C system was investigated. The experimental results indicate the carbon atoms are doped effectively into the ZnO to substitute the O sites. The origin of ferromagnetism in ZnO:C thin films could be due to the p - p interaction of the hybridization of O $2p$ orbitals with C $2p$ states inducing by the substitution of C ions into O sites in the ZnO lattices. This p - p interaction changes the electronic structure in the ZnO:C system and leads to the appearance of additional mixed band levels derived from the semiconductor valence band. Anomalous Hall effect indicates that the majority carriers in the ZnO:C thin films are holes. Direct hole doping at the anion site in the ZnO:C system is sustaining the magnetic moment. The magnetization and p -type conduction in the ZnO:C system were found to be stable in ambient air for more than one year.

9.2 Recommendations for future works

In this thesis, realization of room temperature ferromagnetic ZnO:C thin films and nanostructures is crucial and could open up a broad range of technological applications. However, the carbon concentration in the ZnO:C system was not determined accurately. The relationship between the carbon concentration and the properties of ZnO:C system is vital to the interpretation of the mechanism of the ferromagnetism in ZnO:C system. The analyzing methods with higher sensitivity and precision should be employed for the determination of carbon concentration. Atomic emission spectroscopy is a method of chemical analysis

that quantitative measurement of the optical emission from excited atoms to determine the concentration of an element in a sample. The wavelength of the atomic spectral line gives the identity of the element while the intensity of the emitted light is proportional to the number of atoms of the element. The major advantage of the atomic emission spectroscopy is all atoms in a sample can be detected simultaneously since they are excited simultaneously. One atomic emission spectroscope with a high-resolution spectrometer can reach the resolutions between 0.7~1.0 amu. Auger electron spectroscopy is another useful characterization technique for the chemical analysis of the nanostructured materials and thin films. It is based on the analysis of energetic electrons emitted from an excited atom after a series of internal relaxation events. It could be used to identify element concentration and to determine the lateral composition. Comparing the XPS, Auger electron spectroscopy has higher sensitivity for the light elements of C, O and N. The excellent sensitivity of these analyzing techniques provides a possibility for the determination of carbon concentration as well as the distribution of carbon in the ZnO:C system. The high spatial resolution for lateral composition is conducive to the depth profile characterization of the dopant. The employment of these high-resolution characterization techniques is bound to gain a deeper understanding of the mechanism of ferromagnetism in ZnO:C system.

As to the spintronics devices, electrical spin injection in semiconductors has been proven a difficult task over the last several years. It has been shown experimentally that the ferromagnetic semiconductors are good candidates for electrical spin injection. The *p*-type ZnO:C material is a dilute ferromagnetic

semiconductor that is compatible with spin light emitting diode (LED) technology, and has a Curie temperature (T_C) above room temperature. Therefore, the research on the ZnO:C based spin-LED is an interesting direction in the future. The key step to achieve an applicable spin-LED is the choice of the n -type semiconductors with the conductivity similar to the p -type ZnO:C in order to circumvent the conductivity mismatch.[165]

Another aspect need to be considered is to implement a tunnel barrier in semiconductors due to the extremely short spin-lifetimes of hole acting as the spin-polarized carriers in p -type ZnO:C DMS. We can consider inserting a thin semiconductor layer at the interface to achieve a good tunnel contact or introduce an artificial tunnel barrier between the p -type and n -type semiconductors. Finally, using interband tunneling is possible to convert the spin-polarized holes from a p -type ferromagnetic semiconductor into conduction-electrons in the non-magnetic semiconductor.[166-168] We believe that the present research could serve as a good foundation for the future research & development on the ZnO-based DMS spintronics devices.

REFERENCES

- [1] C. Chappert, A. Fert and F. N. Van Dau, *Nat. Mater.* **6**, 813 (2007).
- [2] S. A. Wolf, D. D. Awschalom, R. A. Buhrman, J. M. Daughton, S. von Molnar, M. L. Roukes, A. Y. Chtchelkanova and D. M. Treger, *Science* **294**, 1488 (2001).
- [3] J. M. George, L. G. Pereira, A. Barthelemy, F. Petroff, L. Steren, J. L. Duvail, A. Fert, R. Loloee, P. Holody and P. A. Schroeder, *Phys. Rev. Lett.* **72**, 408 (1994).
- [4] G. Binasch, P. Grunberg, F. Saurenbach and W. Zinn, *Phys. Rev. B* **39**, 4828 (1989).
- [5] M. N. Baibich, J. M. Broto, A. Fert, F. N. Vandau, F. Petroff, P. Eitenne, G. Creuzet, A. Friederich and J. Chazelas, *Phys. Rev. Lett.* **61**, 2472 (1988).
- [6] P. M. Tedrow and R. Meservey, *Phys. Rev. B* **8**, 5098 (1973).
- [7] S. Datta and B. Das, *Appl. Phys. Lett.* **56**, 665 (1990).
- [8] D. Z. Y. Ting and X. Cartoixa, *Appl. Phys. Lett.* **81**, 4198 (2002).
- [9] A. Voskoboynikov, S. S. Lin, C. P. Lee and O. Tretyak, *J. Appl. Phys.* **87**, 387 (2000).
- [10] T. Koga, J. Nitta and H. Takayanagi, *Phys. Rev. Lett.* **88**, 126601 (2002).
- [11] J. K. Furdyna, *J. Appl. Phys.* **64**, R29 (1988).
- [12] H. Ohno, *Science* **281**, 951 (1998).
- [13] E. L. Nagaev, *Physics of Magnetic Semiconductors* (MIR Moscow, 1983).
- [14] D. J. Craik, *Magnetic Oxides* (Wiley New York, 1975).
- [15] P. A. Wolff, R. N. Bhatt and A. C. Durst, *J. Appl. Phys.* **79**, 5196 (1996).
- [16] T. Story, *Acta Phys. Pol. A* **91**, 173 (1997).
- [17] R. M. Park, M. B. Troffer, C. M. Rouleau, J. M. Depuydt and M. A. Haase, *Appl. Phys. Lett.* **57**, 2127 (1990).



- [18] H. Ohno, *J. Magn. Magn. Mater.* **200**, 110 (1999).
- [19] G. Schmidt, *J. Phys. D. Appl. Phys.* **38**, R107 (2005).
- [20] J. Cibert, J. Bobo and U. Luders, *Comptes Rendus Physique* **6**, 977 (2005).
- [21] I. A. Buyanova, G. Y. Rudko, W. M. Chen, A. A. Toropov, S. V. Sorokin, S. V. Ivanov and P. S. Kop'ev, *Appl. Phys. Lett.* **82**, 1700 (2003).
- [22] T. Dietl, *Semicond. Sci. Tech.* **17**, 377 (2002).
- [23] T. Dietl, H. Ohno, F. Matsukura, J. Cibert and D. Ferrand, *Science* **287**, 1019 (2000).
- [24] K. Sato and H. K. Yoshida, *Jpn. J. Appl. Phys. Part 2* **39**, 334 (2001).
- [25] K. Sato and H. K. Yoshida, *Jpn. J. Appl. Phys.* **39**, L555 (2000).
- [26] T. Fukumura, Z. W. Jin, A. Ohtomo, H. Koinuma and M. Kawasaki, *Appl. Phys. Lett.* **75**, 3366 (1999).
- [27] T. Fukumura, Z. W. Jin, M. Kawasaki, T. Shono, T. Hasegawa, S. Koshihara and H. Koinuma, *Appl. Phys. Lett.* **78**, 958 (2001).
- [28] Z. W. Jin, T. Fukumura, M. Kawasaki, K. Ando, H. Saito, T. Sekiguchi, Y. Z. Yoo, M. Murakami, Y. Matsumoto, T. Hasegawa and H. Koinuma, *Appl. Phys. Lett.* **78**, 3824 (2001).
- [29] A. Tiwari, C. Jin, A. Kvit, D. Kumar, J. F. Muth and J. Narayan, *Solid State Commun.* **121**, 371 (2002).
- [30] S. W. Jung, S. J. An, G. C. Yi, C. U. Jung, S. I. Lee and S. Cho, *Appl. Phys. Lett.* **80**, 4561 (2002).
- [31] D. P. Norton, S. J. Pearton, A. F. Hebard, N. Theodoropoulou, L. A. Boatner and R. G. Wilson, *Appl. Phys. Lett.* **82**, 239 (2003).
- [32] J. H. Kim, H. Kim, D. Kim, Y. E. Ihm and W. K. Choo, *J. Appl. Phys.* **92**, 6066 (2002).
- [33] H. J. Lee, S. Y. Jeong, C. R. Cho and C. H. Park, *Appl. Phys. Lett.* **81**, 4020 (2002).
- [34] K. Ueda, H. Tabata and T. Kawai, *Appl. Phys. Lett.* **79**, 988 (2001).
- [35] Y. M. Cho, W. K. Choo, H. Kim, D. Kim and Y. Ihm, *Appl. Phys. Lett.* **80**, 3358 (2002).
- [36] S. J. Han, J. W. Song, C. H. Yang, S. H. Park, J. H. Park, Y. H. Jeong and K. W. Rhie, *Appl. Phys. Lett.* **81**, 4212 (2002).



- [37] H. Saeki, H. Tabata and T. Kawai, *Solid State Commun.* **120**, 439 (2001).
- [38] H. Akai, *Phys. Rev. Lett.* **81**, 3002 (1998).
- [39] Y. Kopelevich, R. R. da Silva, J. H. S. Torres, A. Penicaud and T. Kyotani, *Phys. Rev. B* **68**, 092408 (2003).
- [40] A. V. Rode, E. G. Gamaly, A. G. Christy, J. G. F. Gerald, S. T. Hyde, R. G. Elliman, B. Luther-Davies, A. I. Veinger, J. Androulakis and J. Giapintzakis, *Phys. Rev. B* **70**, 054407 (2004).
- [41] P. Esquinazi, D. Spemann, R. Hohne, A. Setzer, K. H. Han and T. Butz, *Phys. Rev. Lett.* **91**, 227201 (2003).
- [42] S. Talapatra, P. G. Ganesan, T. Kim, R. Vajtai, M. Huang, M. Shima, G. Ramanath, D. Srivastava, S. C. Deevi and P. M. Ajayan, *Phys. Rev. Lett.* **95**, 097201 (2005).
- [43] H. Ohldag, T. Tyliczszak, R. Hohne, D. Spemann, P. Esquinazi, M. Ungureanu and T. Butz, *Phys. Rev. Lett.* **98**, 187204 (2007).
- [44] P. O. Lehtinen, A. S. Foster, A. Ayuela, T. T. Vehvilainen and R. M. Nieminen, *Phys. Rev. B* **69**, 155422 (2004).
- [45] R. Q. Wu, L. Liu, G. W. Peng and Y. P. Feng, *Appl. Phys. Lett.* **86**, 122510 (2005).
- [46] H. Pan, J. Yi, L. Shen, R. Wu, J. Yang, J. Lin, Y. Feng, J. Ding, L. Van and J. Yin, *Phys. Rev. Lett.* **99**, 127201 (2007).
- [47] S. T. Tan, X. W. Sun, Z. G. Yu, P. Wu, G. Q. Lo and D. L. Kwong, *Appl. Phys. Lett.* **91**, 072101 (2007).
- [48] X. J. Ye, H. A. Song, W. Zhong, M. H. Xu, X. S. Qi, C. Q. Jin, Z. X. Yang, C. T. Au and Y. W. Du, *Journal of Physics D: Applied Physics* **41**, 155005 (2008).
- [49] H. W. Peng, H. J. Xiang, S. H. Wei, S. S. Li, J. B. Xia and J. B. Li, *Phys. Rev. Lett.* **102**, 017201 (2009).
- [50] H. Kwak and J. R. Chelikowsky, *Appl. Phys. Lett.* **95**, 263108 (2009).
- [51] S. C. B. J. Nagare, and D. G. Kanhere, *J. Phys. Chem. A* **114**, 2689 (2010).
- [52] H. S. Kang, B. Du Ahn, J. H. Kim, G. H. Kim, S. H. Lim, H. W. Chang and S. Y. Lee, *Appl. Phys. Lett.* **88**, 202108 (2006).
- [53] Z. Y. Xiao, Y. C. Liu, J. Y. Zhang, D. X. Zhao, Y. M. Lu, D. Z. Shen and X. W. Fan, *Semicond. Sci. Tech.* **20**, 796 (2005).



- [54] R. Triboulet and J. Perriere, *Prog. Cryst. Growth Ch* **47**, 65 (2003).
- [55] X. H. Zhang, S. J. Chua, A. M. Yong, H. D. Li, S. F. Yu and S. P. Lau, *Appl. Phys. Lett.* **88**, 191112 (2006).
- [56] J. M. Lin, H. Y. Lin, C. L. Cheng and Y. F. Chen, *Nanotechnology* **17**, 4391 (2006).
- [57] S. Heitsch, C. Bundesmann, G. Wagner, G. Zimmermann, A. Rahm, H. Hochmuth, G. Benndorf, H. Schmidt, M. Schubert, M. Lorenz and M. Grundmann, *Thin Solid Films* **496**, 234 (2006).
- [58] A. van Dijken, E. A. Meulenkaamp, D. Vanmaekelbergh and A. Meijerink, *J. Luminesc.* **87-89**, 454 (2000).
- [59] H. Morkoç and Ü. Özgür, *Zinc Oxide: Fundamentals, Materials and Device Technology* (Wiley-VCH, 2009).
- [60] N. H. Hong, J. Sakai and A. Hassini, *J. Phys-condens. Mat.* **17**, 199 (2005).
- [61] P. Wu, G. Saraf, Y. Lu, D. H. Hill, R. Gateau, L. Wielunski, R. A. Bartynski, D. A. Arena, J. Dvorak, A. Moodenbaugh, T. Siegrist, J. A. Raley and Y. K. Yeo, *Appl. Phys. Lett.* **89**, 012508 (2006).
- [62] A. Tuan, J. Bryan, A. Pakhomov, V. Shutthanandan, S. Thevuthasan, D. McCready, D. Gaspar, M. Engelhard, J. Rogers, K. Krishnan, D. Gamelin and S. Chambers, *Phys. Rev. B* **70**, 054424 (2004).
- [63] C. Li, G. J. Fang, F. H. Su, G. H. Li, X. G. Wu and X. Z. Zhao, *Nanotechnology* **17**, 3740 (2006).
- [64] Z. P. Sun, L. Liu, L. Zhang and D. Z. Jia, *Nanotechnology* **17**, 2266 (2006).
- [65] H. Y. Yang, S. P. Lau, S. F. Yu, A. P. Abiyasa, M. Tanemura, T. Okita and H. Hatano, *Appl. Phys. Lett.* **89**, 011103 (2006).
- [66] P. M. Gao, C. S. Lao, W. L. Hughes and Z. L. Wang, *Chem. Phys. Lett.* **408**, 174 (2005).
- [67] X. H. Han, G. Z. Wang, L. Zhou and J. G. Hou, *Chem. Commun.*, 212 (2006).
- [68] F. Demangeot, V. Paillard, P. M. Chassaing, C. Pages, M. L. Kahn, A. Maisonnat and B. Chaudret, *Appl. Phys. Lett.* **88**, 071921 (2006).
- [69] K. Rode, A. Anane, R. Mattana, J. P. Contour, O. Durand and R. LeBourgeois, *J. Appl. Phys.* **93**, 7676 (2003).



- [70] A. Fouchet, W. Prellier and L. Mechin, *Superlattice. Microst* **42**, 185 (2007).
- [71] J. M. D. Coey, M. Venkatesan and C. B. Fitzgerald, *Nature Materials* **4**, 173 (2005).
- [72] C. Song, X. J. Liu, K. W. Geng, F. Zeng, F. Pan, B. He and S. Q. Wei, *J. Appl. Phys.* **101**, 103903 (2007).
- [73] T. Kaspar, S. Heald, C. Wang, J. Bryan, T. Droubay, V. Shutthanandan, S. Thevuthasan, D. McCready, A. Kellock, D. Gamelin and S. Chambers, *Phys. Rev. Lett.* **95**, 217203 (2005).
- [74] P. A. Cox, *Transition Metal Oxides* (Clarendon, Oxford, 1992).
- [75] C. Song, F. Zeng, K. Geng, X. Liu, F. Pan, B. He and W. Yan, *Phys. Rev. B* **76**, 045215 (2007).
- [76] T. Dietl, T. Andrearczyk, A. Lipińska, M. Kiecana, M. Tay and Y. Wu, *Phys. Rev. B* **76**, 155312 (2007).
- [77] T. Dietl, A. Haury and Y. M. dAubigne, *Phys. Rev. B* **55**, R3347 (1997).
- [78] T. Dietl, *Nature Materials* **5**, 673 (2006).
- [79] G. L. Liu, Q. Cao, J. X. Deng, P. F. Xing, Y. F. Tian, Y. X. Chen, S. S. Yan and L. M. Mei, *Appl. Phys. Lett.* **90**, 052504 (2007).
- [80] M. Bouloudenine, N. Viart, S. Colis, J. Kortus and A. Dinia, *Appl. Phys. Lett.* **87**, 052501 (2005).
- [81] J. H. Shim, T. Hwang, S. Lee, J. H. Park, S. J. Han and Y. H. Jeong, *Appl. Phys. Lett.* **86**, 082503 (2005).
- [82] K. Potzger, S. Q. Zhou, H. Reuther, A. Mucklich, F. Eichhorn, N. Schell, W. Skorupa, M. Helm, J. Fassbender, T. Herrmannsdorfer and T. P. Papageorgiou, *Appl. Phys. Lett.* **88**, 052508 (2006).
- [83] J. P. Mahoney, C. C. Lin, W. H. Brumage and F. Dorman, *J. Chem. Phys.* **53**, 4286 (1970).
- [84] W. M. Walsh and L. W. Rupp, *Physical Review* **126**, 952 (1962).
- [85] A. Debernardi and M. Fanciulli, *Appl. Phys. Lett.* **90**, 212510 (2007).
- [86] P. Sharma, A. Gupta, K. V. Rao, F. J. Owens, R. Sharma, R. Ahuja, J. M. O. Guillen, B. Johansson and G. A. Gehring, *Nature Materials* **2**, 673 (2003).



- [87] Y. W. Heo, M. P. Ivill, K. Ip, D. P. Norton, S. J. Pearton, J. G. Kelly, R. Rairigh, A. F. Hebard and T. Steiner, *Appl. Phys. Lett.* **84**, 2292 (2004).
- [88] S. Ramachandran, J. Narayan and J. T. Prater, *Appl. Phys. Lett.* **88**, 242503 (2006).
- [89] N. Theodoropoulou, V. Misra, J. Philip, P. Leclair, G. Berera, J. Moodera, B. Satpati and T. Som, *J. Magn. Magn. Mater.* **300**, 407 (2006).
- [90] S. Lim, M. Jeong, M. Ham and J. Myoung, *Jpn. J. Appl. Phys.* **43**, 280 (2004).
- [91] K. Sato and H. K. Yoshida, *Semicond. Sci. Tech.* **17**, 367 (2002).
- [92] J. M. D. Coey, *J. Appl. Phys.* **97**, 10D313 (2005).
- [93] S. J. Pearton, Y. D. Park, C. R. Abernathy, M. E. Overberg, G. T. Thaler, J. Kim, R. Ren, J. M. Zavada and R. G. Wilson, *Thin Solid Films* **447**, 493 (2004).
- [94] C. N. R. Rao and F. L. Deepak, *J. Mater. Chem.* **15**, 573 (2005).
- [95] S. Kolesnik, B. Dabrowski and J. Mais, *J. Appl. Phys.* **95**, 2582 (2004).
- [96] G. Lawes, A. Risbud, A. Ramirez and R. Seshadri, *Phys. Rev. B* **71**, 045201 (2005).
- [97] B. K. Tay, G. F. You, S. P. Lau and X. Shi, *Surface and Coatings Technology* **133-134**, 593 (2000).
- [98] P. J. Martin, S. W. Filipczuk, R. P. Netterfield, J. S. Field, D. F. Whitnall and D. R. McKenzie, *J. Mater. Sci. Lett.* **7**, 410 (1988).
- [99] P. J. Fallon, V. S. Veerasamy, C. A. Davis, J. Robertson, G. A. J. Amaratunga, W. I. Milne and J. Koskinen, *Phys. Rev. B* **48**, 4777 (1993).
- [100] X. Shi, D. I. Flynn, B. K. Tay and H. S. Tan, Filtered Cathodic Arc Source, Patent number: PCT/GB96/00389, 20 February 1995.
- [101] Y. G. Wang, S. P. Lau, H. W. Lee, S. F. Yu, B. K. Tay, X. H. Zhang, K. Y. Tse and H. H. Hng, *J. Appl. Phys.* **94**, 1597 (2003).
- [102] X. L. Xu, S. P. Lau, J. S. Chen, G. Y. Chen and B. K. Tay, *J. Cryst. Growth* **223**, 201 (2001).
- [103] X. Shi, B. G. Tay and S. P. Lau, *Int. J. Mod. Phys. B* **14**, 136 (2000).
- [104] J. Robertson, *Tribol. Int.* **36**, 405 (2003).
- [105] J. Robertson, *Thin Solid Films* **383**, 81 (2001).



- [106] L. W. Yang, X. L. Wu, T. Qiu, G. G. Siu and P. K. Chu, *J. Appl. Phys.* **99**, 074303 (2006).
- [107] Y. Yang, J. X. Wang, X. W. Sun, B. K. Tay, Z. X. Shen and Y. Z. Zhou, *Nanotechnology* **18**, 055709 (2007).
- [108] C. Xu, J. Chun, K. Rho, H. J. Lee, Y. H. Jeong, D.-E. Kim, B. Chon, S. Hong and T. Joo, *Appl. Phys. Lett.* **89**, 093117 (2006).
- [109] H. L. Yan, X. L. Zhong, J. B. Wang, G. J. Huang, S. L. Ding, G. C. Zhou and Y. C. Zhou, *Appl. Phys. Lett.* **90**, 082503 (2007).
- [110] J. W. Chiou, H. M. Tsai, C. W. Pao, K. P. Krishna Kumar, J. H. Chen, D. C. Ling, F. Z. Chien, W. F. Pong, M. H. Tsai, J. J. Wu, M. H. Yang, S. C. Liu, I. H. Hong, C. H. Chen, H. J. Lin and J. F. Lee, *Appl. Phys. Lett.* **90**, 062103 (2007).
- [111] W. B. Jian, Z. Y. Wu, R. T. Huang, F. R. Chen, J. J. Kai, C. Y. Wu, S. J. Chiang, M. D. Lan and J. J. Lin, *Phys. Rev. B* **73**, 233308 (2006).
- [112] J. Luo, J. K. Liang, Q. L. Liu, F. S. Liu, Y. Zhang, B. J. Sun and G. H. Rao, *J. Appl. Phys.* **97**, 086106 (2005).
- [113] J. J. Chen, M. H. Yu, W. L. Zhou, K. Sun and L. M. Wang, *Appl. Phys. Lett.* **87**, 173119 (2005).
- [114] G. Savigny, J. R. Currie, D. Ila, R. L. Zimmerman, C. I. Muntele, R. Mu and A. Ueda, *Surf. Coat. Tech.* **196**, 113 (2005).
- [115] J. Ghatak, B. Satpati, M. Umananda, D. Kabiraj, T. Som, B. N. Dev, K. Akimoto, K. Ito, T. Emoto and P. V. Satyam, *Nucl. Instr. Meth. Phys. Res. B* **244**, 45 (2006).
- [116] M. Tanemura, H. Yamauchi, Y. Yamane, T. Okita and S. Tanemura, *Nuclear Instruments and Methods in Physics Research Section B: Beam Interactions with Materials and Atoms* **215**, 137 (2004).
- [117] M. Tanemura, T. Okita, H. Yamauchi, S. Tanemura and R. Morishima, *Appl. Phys. Lett.* **84**, 3831 (2004).
- [118] M. Tanemura, J. Tanaka, K. Itoh, Y. Fujimoto, Y. Agawa, L. Miao and S. Tanemura, *Appl. Phys. Lett.* **86**, 113107 (2005).
- [119] T. S. Heng, S. P. Lau, S. F. Yu, H. Y. Yang, L. Wang, M. Tanemura and J. S. Chen, *Appl. Phys. Lett.* **90**, 032509 (2007).
- [120] M. Tanemura, H. Hatano, M. Kudo, N. Ide, Y. Fujimoto, L. Miao, H. Yang, S. Lau, S. Yu and J. Kato, *Surf. Sci.* **601**, 4459 (2007).



- [121] T. S. Herng, S. P. Lau, C. S. Wei, L. Wang, B. C. Zhao, M. Tanemura and Y. Akaike, *Appl. Phys. Lett.* **95**, 133103 (2009).
- [122] N. A. Geisse, *Materials Today* **12**, 40 (2009).
- [123] K. Gramm, L. Lundgren and O. Beckman, *Phys. Scripta.* **13**, 93 (1976).
- [124] U. Ozgur, Y. I. Alivov, C. Liu, A. Teke, M. A. Reshchikov, S. Dogan, V. Avrutin, S. J. Cho and H. Morkoc, *J. Appl. Phys.* **98**, 041301 (2005).
- [125] Y. F. Chen, D. M. Bagnall, H. J. Koh, K. T. Park, K. Hiraga, Z. Q. Zhu and T. Yao, *J. Appl. Phys.* **84**, 3912 (1998).
- [126] N. Y. Garces, N. C. Giles, L. E. Halliburton, G. Cantwell, D. B. Eason, D. C. Reynolds and D. C. Look, *Appl. Phys. Lett.* **80**, 1334 (2002).
- [127] K. Vanheusden, W. L. Warren, C. H. Seager, D. R. Tallant, J. A. Voigt and B. E. Gnade, *J. Appl. Phys.* **79**, 7983 (1996).
- [128] K. Vanheusden, C. H. Seager, W. L. Warren, D. R. Tallant, J. Caruso, M. J. HampdenSmith and T. T. Kodas, *J. Lumin.* **75**, 11 (1997).
- [129] S. Lee, Y. Shon, S.-W. Lee, S. J. Hwang, H. S. Lee, T. W. Kang and D. Y. Kim, *Appl. Phys. Lett.* **88**, 212513 (2006).
- [130] M. Foygel, R. Morris and A. Petukhov, *Phys. Rev. B* **67**, 134205 (2003).
- [131] Maranzan.Fe, *Physical Review* **160**, 421 (1967).
- [132] X. Y. Peng and R. Ahuja, *Appl. Phys. Lett.* **94**, 102504 (2009).
- [133] C. Liu, F. Yun and H. Morkoc, *J. Mater. Sci-mater. El* **16**, 555 (2005).
- [134] P. M. Levy and S. F. Zhang, *Phys. Rev. Lett.* **79**, 5110 (1997).
- [135] A. Urushibara, Y. Moritomo, T. Arima, A. Asamitsu, G. Kido and Y. Tokura, *Phys. Rev. B* **51**, 14103 (1995).
- [136] N. H. Hong, J. Sakai, N. Poirot and V. Brize, *Phys. Rev. B* **73**, 132404 (2006).
- [137] Q. Wan, *Appl. Phys. Lett.* **89**, 082515 (2006).
- [138] T. S. Herng, S. P. Lau, S. F. Yu, H. Y. Yang, K. S. Teng and J. S. Chen, *Journal of Physics: Condensed Matter* **19**, 356214 (2007).
- [139] D. Y. Pan, J. G. Wan, G. L. Xu, L. Y. Lv, Y. J. Wu, H. Min, J. M. Liu and G. H. Wang, *J. Am. Chem. Soc.* **128**, 12608 (2006).



- [140] O. Auciello and R. Kelly, *Ion Bombardment Modification of Surfaces* (Elsevier Tokyo, 1984).
- [141] A. W. Czanderna, T. E. Madey and C. J. Powell, *Beam Effects, Surface Topography, and Depth Profiling in Surface Analysis* (Plenum New York, 1998).
- [142] F. Y. Ran, M. Tanemura, Y. Hayashi, N. Ide, M. Imaoka, T. S. Heng and S. P. Lau, *Z. Naturforsch. A* **64**, 765 (2009).
- [143] H. Y. Yang, S. F. Yu, S. P. Lau, T. S. Heng and M. Tanemura, *Nanoscale Research Letters* **5**, 247 (2010).
- [144] T. S. Heng, S. P. Lau, L. Wang, B. C. Zhao, S. F. Yu, M. Tanemura, A. Akaike and K. S. Teng, *Appl. Phys. Lett.* **95**, 012505 (2009).
- [145] P. Sati, C. Deparis, C. Morhain, S. Schäfer and A. Stepanov, *Phys. Rev. Lett.* **98**, 137204 (2007).
- [146] T. Chanier, M. Sargolzaei, I. Opahle, R. Hayn and K. Koepf, *Phys. Rev. B* **73**, 134418 (2006).
- [147] G. J. Strijkers, J. H. J. Dalderop, M. A. A. Broeksteeg, H. J. M. Swagten and W. J. M. de Jonge, *J. Appl. Phys.* **86**, 5141 (1999).
- [148] G. C. Han, B. Y. Zong, P. Luo and Y. H. Wu, *J. Appl. Phys.* **93**, 9202 (2003).
- [149] A. Encinas-Oropesa, M. Demand, L. Piraux, I. Huynen and U. Ebels, *Phys. Rev. B* **63**, 104415 (2001).
- [150] J. B. Cui and U. J. Gibson, *Appl. Phys. Lett.* **87**, 133108 (2005).
- [151] S. Y. Zhuo, X. C. Liu, Z. Xiong, J. H. Yang and E. W. Shi, *Solid State Commun.* **152**, 257 (2012).
- [152] K. Potzger, S. Q. Zhou, J. Grenzer, M. Helm and J. Fassbender, *Appl. Phys. Lett.* **92**, 182504 (2008).
- [153] H. S. Hsu, J. C. A. Huang, S. F. Chen and C. P. Liu, *Appl. Phys. Lett.* **90**, 102506 (2007).
- [154] X. J. Liu, X. Y. Zhu, C. Song, F. Zeng and F. Pan, *J. Phys. D: Appl. Phys.* **42**, 035004 (2009).
- [155] P. Thakur, K. H. Chaey, M. Subramanain, R. Jayavel and K. Asokan, *J. Korean Phys. Soc.* **53**, 2821 (2008).
- [156] P. Thakur, S. Gautam, K. H. Chae, M. Subramanain, R. Jayavel and K. Asokan, *J. Korean Phys. Soc.* **55**, 177 (2009).



- [157] W. Yan, Z. Sun, Q. Liu, Z. Li, Z. Pan, J. Wang, S. Wei, D. Wang, Y. Zhou and X. Zhang, *Appl. Phys. Lett.* **91**, 062113 (2007).
- [158] S. Gautam, P. Thakur, K. H. Chae, G. S. Chang, M. Subramanain, R. Jayavel and K. Asokan, *J. Korean Phys. Soc.* **55**, 167 (2009).
- [159] V. Vaithianathan, K. Asokan, J. Y. Park and S. S. Kim, *Appl. Phys. A-mater.* **94**, 995 (2009).
- [160] M. Subramanian, P. Thakur, S. Gautam, K. H. Chae, M. Tanemura, T. Hihara, S. Vijayalakshmi, T. Soga, S. S. Kim, K. Asokan and R. Jayavel, *J. Phys. D. Appl. Phys.* **42**, 105410 (2009).
- [161] J. F. Morar, F. J. Himpsel, G. Hollinger, G. Hughes and J. L. Jordan, *Phys. Rev. Lett.* **54**, 1960 (1985).
- [162] Y. Ma, N. Wassdahl, P. Skytt, J. Guo, J. Nordgren, P. D. Johnson, J. E. Rubensson, T. Boske, W. Eberhardt and S. D. Kevan, *Phys. Rev. Lett.* **69**, 2598 (1992).
- [163] D. A. Fischer, R. M. Wentzcovitch, R. G. Carr, A. Continenza and A. J. Freeman, *Phys. Rev. B* **44**, 1427 (1991).
- [164] P. E. Batson, *Phys. Rev. B* **48**, 2608 (1993).
- [165] V. F. Motsnyi, J. De Boeck, J. Das, W. Van Roy, G. Borghs, E. Goovaerts and V. I. Safarov, *Appl. Phys. Lett.* **81**, 265 (2002).
- [166] M. Kohda, Y. Ohno, K. Takamura, F. Matsukura and H. Ohno, *Jpn. J. Appl. Phys. Part 2* **40**, L1274 (2001).
- [167] E. Johnston-Halperin, D. Lofgreen, R. K. Kawakami, D. K. Young, L. Coldren, A. C. Gossard and D. D. Awschalom, *Phys. Rev. B* **65**, 041306 (2002).
- [168] P. Van Dorpe, Z. Liu, W. Van Roy, V. F. Motsnyi, M. Sawicki, G. Borghs and J. De Boeck, *Appl. Phys. Lett.* **84**, 3495 (2004).